Development of Wave Prediction and Virtual Buoy Systems

2010

Tracey Hiroto Alena Tom

Acknowledgements

The quest for academic excellence by earning a PhD is never traveled alone and support from many individuals is needed. There have been many people that have helped, encouraged, and inspired me along my quest and proper acknowledgement requires another thesis on the topic.

I am most grateful to Professor Hajime Mase whose guidance and support has truly kept me on course throughout this journey. His extensive research in wave modeling along with respect carried in the world wide scientific community has given me the knowledge and confidence to bring inspirational ideas to working reality. I would have never been able to accomplish as much without his expertise, encouragement, and unselfish help.

I wish to thank Professor Nobuhiro Mori for giving me invaluable advice on advanced usage of wave spectra and allowing me to see the paths that wave modeling can offer. Professor Tomohiro Yasuda has helped me find limits of my programs and given me the opportunity to contribute to his research and projects.

A heartfelt thank you goes out to Michio Kato, Kazuyuki Ogawa, Haruki Takeichi and everyone at Surflegend, Inc. for providing the valuable resources that was needed to undertake a project such as this. My research would have been physically impossible without their total trust and encouragement over the past five years. A special thanks to Mark Uranaka of Datahouse, Inc., his mentoring earlier in my career gave me the courage to set high goals.

I thank my family and friends for the encouragement and support they continue to provide me. Especially to my grandparents who have been the pillars of my life, to my Uncle Ba for inspiring me to pursue engineering, to my Uncle Roy and Aunty Tachan for pushing me towards academic achievement and my mom for having trust in me and allowing me to live my dreams. To Toshihisa and Mutsue Kawabata, thank you for accepting me into your family and helping me assimilate into Japan's society.

Most of all to my wife Mayumi and our children Kai and Koa, who form the foundation of my life, offering me total support and are the source of my motivation to search for excellence.

Table of contents

List of figures

List of tables

Chapter 1 Introduction

1.1 Motivations

WAVE HAZARD EXISTS– Waves generated and propagated on the ocean surface pose a potential hazard to seafarers and inhabitants along the sea as well as to coastal and offshore structures. According to Takayama (2006), Japan has been affected by disasters caused by high wave and storm surge from typhoons in the past, greatly due to being surrounded by water and geographically situated in the path of seasonal typhoons. Storm surge is characterized by a long gravity wave that rapidly raises water levels along coastlines causing flooding. High wind waves are characterized by waves that start as disorganized patterns of varying short gravity waves then grow to organized regularly spaced smooth waves of similar height moving in a uniform direction (Jelesnianski, 1993). Wind waves of long duration cause erosion to foundations and overtopping of protective structures.

NEED FOR INFORMATION INCREASING – The need for accurate marine information is increasing as marine activity increases. Oceans cover 70 percent of the world's surface and even with the large network of buoys available today, many areas are still unobserved. Reliable marine information is the key to support ocean situational awareness by providing user with the ability to estimate times and locations of potential dangerous ocean conditions. Commercial ocean navigation require forecasted information to safely select routes; coastal protection management require information for determination of potential disasters; scientist require information to analyze ocean events; engineers require information for structural design; and marine seafarers require information to select the proper equipment and determine safe locations.

Many organizations provide atmospheric and oceanographic information through various mediums, such as TV, radio, and Internet. Japan Metrological Agency (JMA) generates most of the raw metrological data for areas surrounding Japan. Free information is usually limited to synoptic pressure maps with 48 hour lead times displayed only as visual maps. Recreational marine users normally venture 10 km away from land at most, but freely available coarse resolution numerical weather prediction (NWP) data often fail to resolve the small-scale wind systems that play a crucial role in the generation of near shore waves.

RISK INCREASING – Destructive weather systems have been on the rise and a link to global climate change has been postulated. According to Knutson et al. (2004), idealized hurricanes simulated under warmer high-CO_2 conditions are more intense. Knutson et al. (2004) postulates that CO_2 gas-induced global warming may gradually increase the occurrences of highly destructive, "Super-Typhoon" class pressure systems. Researchers at the School of Earth and Atmospheric Sciences at Georgia Institute of Technology and the National Center for Atmospheric Research (NCAR), state the number of, "Super-Typhoon" class weather systems has doubled over the past 35 years, even though the total number has

dropped since the 1900's. Increases in population, infrastructure, and wealth on coastlines worldwide along with increased occurrence of destructive weather events greatly places special importance on the skill of wind and wave forecasting.

ACCIDENTS INCREASING – On the average, from 2001 through 2006, there were 312, seashore and marine accidents in Japan due to insufficient weather information (Japan Marine Recreation Association, 2006). Figure 1.1 shows the number of accidents due to insufficient information grouped by activity. In general, marine users engaged in commercial activities offshore have a low number of accidents due to accessibility to weather information. Marine activities close to shore such as: commercial boat fishing, swimming, and shore fishing are groups of concern where accidents of insufficient information are rising. Table 1.1 shows an increase in the number of accidents as the frequency of typhoons increase. Swimmers are directly impacted by increases of typhoons, showing a need for readily accessible information of ocean conditions now and in the future.

PROCESSING COST DECREASING – Proprietary wind-wave modeling systems and software have historically been only accessible for commercial and disaster prevention applications due to high operation and development cost. The high overall cost required to produce detailed forecast information is passed on to mariners, placing a price on overall safety. The cost of research, development, maintenance, and dissemination of weather systems are decreasing due to shared open source development, worldwide connectivity, and lowering cost of computing systems.

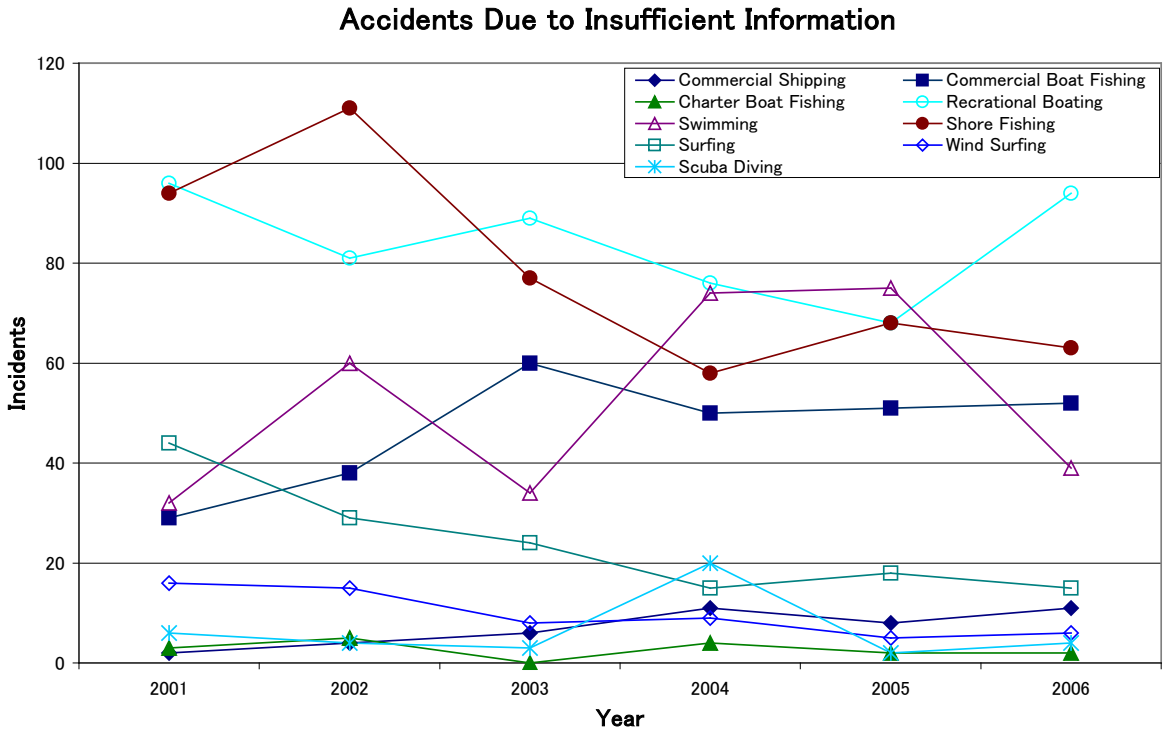

Fig. 1.1 Accidents due to insufficient information from 2001 through 2006

Table 1.1 Number of accidents due to insufficient information from 2001 through 2006

	YEAR						
	2001	2002	2003	2004	2005	2006	AVERAGE
Commercial Shipping	2	4	6	11	8	11	7
Commercial Boat Fishing	29	38	60	50	51	52	47
Charter Boat Fishing	3	5	0	4	2	2	3
Recreational Boating	96	81	89	76	68	94	84
Swimming	32	60	34	74	75	39	52
Shore Fishing	94	111	77	58	68	63	79
Surfing	44	29	24	15	18	15	24
Wind Surfing	16	15	8	9	5	6	10
Scuba Diving	6	4	3	20	2	4	7
TOTAL	322	347	301	317	297	286	312
Typhoon TOTAL	26	26	21	29	23	23	25

WAVE MODELING IMPROVING - Steady improvements in wave modeling theory have led very sophisticated ocean wave models that are able to accurately hindcast the ocean state during the past and forecast into the future. Modern ocean wave models can calculate wind-wave predictions on global, regional and site specific scales. Advances are greatly due to shared collaboration of worldwide scientist to address deficiencies of individual theories.

WIND DATA IMPROVING– The advances made in numerical meteorological weather have allowed more complete wind data grids to be used as input into wind-wave models. Wind-wave model performance is proportional to the quality of wind input. Both analysis and forecasted wind data with spatial resolutions of 1.0 degree (synoptic-scale) down to one km (meso-scale) can be readily accessed through the internet in real-time. If needed, synoptic meteorological data can be used as input into a local meso-scale weather model to produce wind grids with a very fine spatial resolution. Gridded analysis data is available hourly and forecast data can be obtained up to 4 times a day.

DATA DISTRIBUTION IMPROVING – Internet connectivity and data servers have allowed an easier and faster way of accessing information. Improvement in meteorological data access has reduced the cost, process, and time of acquiring real-time and archived data. Data distribution through the internet has allowed valuable information to reach a larger audience. Access to information by mobile devices through satellite and cellular communication networks in remote offshore locations, allows marine users to make better decisions on safety.

The goal of this study is to develop an accurate cost-effective wind-wave analysis system to aid in the prevention of future loss of life and property. Accurate wave prediction, available to more individuals, allows for better planning and preparation before a potential destructive event. The ability to better recreate ocean conditions of prior events that produced high wave and surge allows for better disaster analysis and prevention. Real-time wave analysis offers the current view of ocean conditions allowing for better marine safety management. Distribution of accurate prediction information to more people at lower cost will lead to a reduction of accidents caused due to lack of information. Successful development of an accurate wind-wave analysis system will have benefits throughout the world, especially in areas that are not privileged to a have full-scale advanced wave warning system.

In order to develop a cost-effective system the latest developments in: (1) wind-wave modeling, (2) parallel computing, (3) data processing, and (4) data communication is utilized. All of which are covered under, “GNU Open Source Licensing,” which has been the major contributing factor in keeping development cost low while facilitating a high level of intellectual development. Internet access allows access to high-quality real-time meteorological data and distribution of processed data. System infrastructure is based on, “Beowulf High Performance Computing,” systems using commodity equipment.

This study investigates the development and validation of a wind-wave analysis system where major topics are:

1) to investigate wind-wave ocean modeling on Beowulf High Performance Computing systems using commodity personal computing equipment,
2) to understand the forecasting ability of the wind-wave ocean model, for seas surrounding Japan, during both normal seasonal events as well as extreme wind events,
3) to understand the hindcasting ability of the wind-wave ocean model, for extreme wind events in the seas surrounding Japan and the Gulf of Mexico,
4) to understand the effectiveness of different meteorological synoptic and meso-scale analysis and forecast wind data when applied to the wind-wave ocean model,
5) to investigate the performance of action-balance formulations of Komen et al. (1984) and Janssen (1991) in the SWAN wind-wave model ,
6) to investigate the performance improvements to the Janssen (1991) action-balance formulation as specified by Lalbeharry et al. (2004),
7) to investigate real-time wave prediction using GPV analysis data available hourly,
8) to develop a real-time virtual buoy system using hourly available GPV data that provides wave statistical parameters of the seas surrounding Japan.

1.2 Thesis structure

The general layout of this thesis is as follows:

Chapter 2 presents the individual components of the developed wind-wave analysis system. System details include discussions on the computing architecture, meteorological data, wind-wave model, and data dissemination.

Chapter 3 presents verification of the developed system as employed for wind–wave forecasting. This chapter discusses the performance ability of the SWAN wind-wave model to forecast ocean waves. Specific validation included:

1) Evaluation of system performance and wave forecasts for the seas surrounding Japan,
2) Evaluation of GFS and WRF wind input and wave forecasts for the seas surrounding Japan during three seasons.

Chapter 4 presents analysis of the developed system as employed for wind-wave hindcasting. This chapter discusses ability of the SWAN wind-wave model, to recreate the ocean's state during previous events. Performance of the SWAN wind-wave model with different meteorological wind input, energy transfer models, and frequency ranges were evaluated. Specific validation included:

1) Evaluation of waves generated by Typhoon Tokage using GFS wind analysis input,
2) Evaluation of wind and waves generated by Hurricane Katrina, using three types of meteorological wind analysis data, three energy transfer settings in SWAN, and two frequency ranges were compared and evaluated.

Chapter 5 presents the developed system as employed for real-time wind-wave hindcasting and forecasting. Specific development and testing included:

1) Evaluation of hindcast and forecast, calculated hourly, of the seas surrounding Japan using hourly available GPV atmospheric analysis data,
2) Development of a virtual-buoy system using wave analysis calculated hourly. This system simulates wave gauges by displaying real-time wave information of any grid point within the computational domain.

Chapter 6 presents conclusions of this study and future projects.

Chapter 2 Wave prediction and analysis system

2.1 Introduction

Wind-wave modeling has grown from the pioneering work of approximating wind-wave growth by Sverdrup and Munk (1947) to third-generation (3G) spectral wave modeling proposed by the WAM Group (1988). 3G model development was started by the need to improve limitations of parametrical based spectrum second generation (2G) models. 3G spectral wave modeling are characterized by the following:

- Source/sink mechanisms are defined discretely in the frequency/direction domain, and are not parametric or empirically formulated,
- Spectral shape is not bound by a priori limit and the spectrum is defined from the balance of the source/sink term,
- Nonlinear wave-wave interaction is solved explicitly.

The move from 2G parameterization to 3G discrete formulation has increased spectral wave modeling capabilities, but more processing power is needed to perform the required calculations. Significant advances in computing technology have allowed sophisticated numerical wind-wave modeling to take advantage of the calculation power offered by today's high performance computing (HPC) systems. HPC systems allow modern numerical wind-wave models to perform complex calculations, accurately, timely and cost-efficiently.

Dramatic improvement and availability of commodity personal computers have made clusters of commodity computers, now commonly known as Beowulf Clusters, a viable alternative to commercial super computer systems. Beowulf Clusters allow scalable HPC at relatively low cost. Traditionally supercomputers solutions from commercial vendors were the only available option. These solutions were very expensive and out of the reach of many small to medium-sized research groups, universities and companies.

A large factor contributing to the rapid development of both advanced numerical wind-wave models and Beowulf Clusters is the adoption of open source licensing. Open source licensing protects software by ensuring the, "source code," of all development is readily available. Open source licensing helps lower overall cost and promotes co-operative development through open collaboration of theories and findings.

Advances in meteorological data analysis and forecasting have allowed wind-wave models to utilize a higher quality of wind input. Availability of meteorological data has dramatically increased in recent years due to a combination of increased storage capability, file compression, and internet transfer rates. Data availability along with file standardization, have simplified data manipulation and extraction to where analysis of devastating high sea events can be performed immediately.

Calculated output from wind wave and prediction systems can be delivered to more locations at very low cost. Internet and file server technologies have allowed dissemination of data to more people than ever before by many methods, such as through Hypertext Transfer Protocol (HTTP), File Transfer Protocol (FTP) and Simple Mail Transfer Protocol (SMTP). Additionally, wireless communications technology has also allowed the ability to deliver information to mobile devices through SMTP and modified HTTP.

The developed wind-wave system consists of four core components: (1) system architecture, (2) meteorological wind input, (3) wind-wave model, and (4) system processes.

The first core component is the system architecture. The system architecture includes computing hardware that provides the system with a platform for data acquisition, processing, storage, and dissemination. Section 2.2, describes: (1) what comprises the system, (2) how the system communicates, (3) what facilitates developmental collaboration, and (4) what allows the system to be cost effective.

The second core component is the meteorological wind input. Numerical weather prediction (NWP) models describe the current and future atmospheric conditions. Wind forcing for modern wind-wave models are provided by 10 meter wind grids generated by NWP models. Each NWP model wind grid exhibits different characteristics that affect wave prediction accuracy. Accuracy of wave prediction is heavily dependent on the accuracy of the wind input data. Section 2.3, describes the NWP models used by the developed wind wave analysis system.

The third component is the wind-wave model. The developed wind-wave analysis system uses the SWAN (Simulating Waves Nearshore) wind-wave model, Booij et al. (1999). SWAN is based on the action balance equation. Section 2.4, details the key concepts of wind-wave analysis using the spectral energy balance as well as the source/sink terms as implemented by SWAN.

The fourth component is systems operation and data dissemination. The developed system is designed to operate automatically, with manual intervention only during times of trouble. Data is automatically downloaded, prepared, processed, and distributed. Section 2.5, describes the processes performed automatically by the system and currently employed method of data dissemination.

2.2 System architecture

System architecture consists of (1) computing hardware, (2) operating system, and (3) systems software. This section describes the hardware design basis as well as the software that controls communication and operational tasks. The completed system is described as a high performance computing (HPC) system made possible by the open source development of Beowulf Cluster computers.

2.2.1 High-performance computing

HPC refers to the use of computing systems comprised of multiple processors linked together into a single system with networking interconnects to provide greater computation power. Each processor is controlled by a communications library enabling more computational cycles available to solve a single problem. Large computations required by modern wind-wave models are accomplished through the distributed parallel computing capabilities of HPC systems. Modeled on the basis of a Class I Beowulf Cluster Computer, this section describes the system architecture of the developed wind-wave system.

2.2.1.1 Open source

Open source licensing is a copyright license for computer software that makes the source code available for modification and redistribution without having to pay the original author. The GNU General Public License (GPL) originally written by Richard Stallman is intended to guarantee freedom to share and change all versions of a program and to make sure the software remains free for all users. GNU is a recursive acronym meaning, “GNU is Not Unix.”

Great advancements in HPC systems are attributed to GPL by allowing open collaboration of Linux, GNU software, and the "standardization" of message passing via Message Passing Interface (MPI) libraries. GPL has allowed researchers and scientist to openly collaborate and develop new theories in wind and wave modeling.

2.2.1.2 Beowulf Cluster

Beowulf Clusters are based on a cluster of commodity off the-shelf (COTS) personal computer hardware interconnected on a private local area network with an open source software infrastructure. Performance can be improved by adding machines and using faster network interconnections. The Beowulf Cluster idea enables researchers to build their own small supercomputer, capable of running computational intensive models with substantial savings in cost. As COTS technology evolves, a Beowulf Cluster can be easily upgraded to take advantage of it. A Beowulf Cluster can be as simple as two networked computers each running Linux and sharing a file system or as complex as 1000 nodes with a high-speed, low-latency network.

There are generally two classifications of Beowulf Clusters:

- Class I clusters are built entirely using commodity hardware and software using standard technology such as SCSI, Ethernet, and IDE.
- Class II clusters are built using specialized hardware and software to achieve higher performance.

The performance of a class II cluster is better than that of a class I cluster with the drawback of increased cost. The developed wind-wave system was designed under the Beowulf class I cluster classification to keep costs at a minimum. A detailed description of a Beowulf Cluster can be found in Brown (2004)

2.2.2 Hardware

The Beowulf Cluster infrastructure mainly consists of a cluster of computers known as, “compute nodes, " interconnected by standard Ethernet networking. Each node has access to a shared file working/storage area. Also attached to the network is a “master node” that controls and schedules processing. Following the Beowulf class I specification, all hardware used in the developed system are COTS products.

2.2.2.1 Computing node

The computational node represents the basic building block of a Beowulf Cluster. A typical Beowulf Cluster consists of a head node and one or many compute nodes. The head node is the command center of the Beowulf Cluster and runs the communicative daemons necessary to transform the individual nodes into a cohesive cluster. Typically, the head node handles the mounting of shared file-systems, job monitoring, resource allocation and access to the outside world. The compute nodes are solely dedicated to computational processing.

Each node must have a central processing unit (CPU), random access memory (RAM), and hard disk storage space. The CPU is the computational heart of the cluster with its main function to perform calculus. Each node can contain one or more CPU’s. RAM is used for quick access to intermediate data used in processing. Hard disk storage space is needed to store the operating system and processing software on each node. The hard disk space on the head node is generally larger to serve shared data to each node.

2.2.2.2 Network interconnect

The head and compute nodes are networked together and communicate over a private LAN through standard network protocols, isolated from ordinary network traffic. The most demanding communication occurs between compute nodes and performance is greatly affected by the efficiency of network communication where high bandwidth, high speed, and low latency are recommended. The most common network protocols available are Fast Ethernet, Gigabit Ethernet, Myrinet, and Infiniband.

The developed wind-wave system utilizes Gigabit Ethernet technology for communication between each computer on the cluster. Each computer is connected by a switch that controls communication between each node. The advantage of a switch is that it accepts packets on twisted-pair wires from each computer and does not broadcast to all the connected nodes to determine who the receiver is as does a hub.

2.2.3 Software

The driving concept of a Beowulf Cluster can be described as, "Strength in Numbers," or "Divide and Conquer." The Beowulf Cluster achieves its processing power through, "Parallel Processing." The term, "parallel processing," generally refers to the concept of speeding-up program execution by dividing program tasks into multiple fragments that can execute simultaneously on each processor. A program being executed across *n* processors might execute *n* times faster than it would a single processor. Software is vital for each node on the cluster to operate singularly as well as cohesively. This section describes the software used by the developed system and required by Beowulf Clusters. Software is categorized into the following groups: (1) an operating system which includes tools necessary to build and control the computer, (2) a file system that allows each node direct access to shared data, and (3) a message passing interface library for inter-process communication.

2.2.3.1 Operating system

An operating system (OS) performs many tasks, such as performing memory allocation, prioritizing system request, controlling input and output devices, facilitating networking and managing file systems. Linux is a free Unix-type OS originally created by Linus Torvalds with the assistance of developers around the world. Developed under GPL, the source code for Linux is freely available to everyone. The developed wind-wave system uses Red Hat Linux 8.0 as the OS on the head and compute nodes.

2.2.3.2 File system

A shared file area accessible by all nodes is required to share data as well as control parallel processing on the Beowulf Cluster. Network File System (NFS) commonly used by Beowulf Clusters to provide a distributed file system. The head node or dedicated file server exports files to compute nodes that access them as if they are local. NFS does not save information about the client that made the request, so every client request is considered independently. Therefore, they must contain all the information necessary for execution each time they make a call to the server. This causes large messages and consumes a lot of network bandwidth. The advantage, however, of this system is that if the client crashes, the server does not halt, but continues working and satisfying all the other requests.

Higher I/O performance and processor performance has led to I/O bottlenecks in many applications, especially those using large data sets. A popular approach for alleviating this kind of bottleneck is the use of parallel file systems where multiple disks on different nodes are striped together into a single file system. By spreading out file data in this manner, larger files can be created, potential bandwidth is increased, and network bottlenecks are minimized. The developed system utilizes NFS for its ease of access and maintenance.

2.2.3.3 Message passing interface

Parallel processing is accomplished by splitting an application into several tasks, each task having its own private data, memory space, and computational cycles. Communication of each task is accomplished on the software level by an explicit message passing interface (MPI) library. The MPI standard was first released in 1994 from MPI Forum (MPIF). It specifies a portable interface for writing message passing parallel programs. Network technology with high bandwidth and low latency is important for maximizing cluster efficiency and speed. Details about MPI and MPIF can be found at: http://www.mpi-forum.org.

MPICH2 from Argonne National Laboratory is an implementation of the MPI with a goal to provide a portable implementation of MPI-2. It also provides a vehicle for MPI implementation research and for developing new and better parallel programming environments. OpenMP is a message passing library designed to work within a symmetric multi processor (SMP) machine. In the SMP model, the processors have a shared memory address space, which can be used to transport messages. MPICH2 supports the use of the hybrid programming model, where both MPI and OpenMP are utilized. Communication between nodes use MPI and communication within SMP machines use OpenMP. MPICH2 is a freely available and can be found at: http://www-unix.mcs.anl.gov/mpi/mpich2. The developed wind-wave system uses MPICH2 to accomplish parallel processing through inter process communication. MPICH2 runs a daemon on each node which relives the dependency on specific nodes to be up and running, increasing the fault tolerance of the developed system.

2.3 Numerical weather models

Wind-wave models depend on accurate meteorological 10m wind grid for wind forcing. Historically wind estimates were manually interpolated from direct measurements or synoptic weather charts. The availability of numerical weather prediction data grids eliminates the need for manual determination of wind characteristics.

Models can either be global (covering the entire Earth) or regional (covering only a part of the Earth). Global models often use spectral methods for the horizontal dimensions and finite difference methods for the vertical dimension. Regional models can use finer grids to resolve smaller-scale meteorological phenomena and usually use finite-difference methods in all three dimensions.

The developed wind-wave system uses 10m wind data from various meteorological datasets. This chapter presents the meteorological aspects involved in wind generation, the different scales of atmospheric motions, and the meteorological datasets available for use in the wind-wave models.

2.3.1 Meteorological aspects of wind generation

Wind generation is the most important factor that meteorology has on wave generation. Understanding the basic processes involved in wind generation over marine and coastal areas are necessary for wave prediction.

Solar heating and earth rotation are the primary driving mechanisms for atmospheric motions. Vertical motions are typically driven by instabilities created by: (1) direct surface heating, (2) advection of air into a region of different ambient air density, (3) topographic effects, or (4) compensatory motions related to mass conservation. Horizontal motions tend to be driven by gradients in near-surface air densities created by differential heating, and compensatory motions related to conservation of mass.

2.3.1.1 Atmospheric winds

The Earth's atmosphere extends from the surface to over 100 km in height. Vertical layering of the atmosphere increases in height, primarily due to the absorption of specific bands of radiation in localized vertical regions. Absorption of radiation in each layer causes substantial warming, producing layers of local mixing. The troposphere extends from the earth's surface to an average altitude of 11 km and contains useful meteorological information for estimating surface winds in marine areas.

The lowest portion of the troposphere is commonly referred to as, "the atmospheric or planetary boundary layer (PBL)." Typically the PBL is considered to be from the surface layer up to a height of 1-2 km. This height varies with latitude, season, and time of day. The

PBL is the region of the atmosphere directly influenced by the presence of the earth's surface. Surface friction causes the wind within the PBL to be turbulent and gusty. Frictional drag decreases with height causing winds to be more uniform at stronger at higher altitudes.

The lowest level of the PBL, where the fluxes are approximately equal to surface values, is sometimes termed the constant flux layer. In this bottom layer, the time scale of momentum transfer is so short that there is little or no Coriolis effect; hence the wind direction remains approximately constant. Above this layer is the outer layer, where fluxes are not constant as in the surface layer but decrease monotonically from their surface values to small values at the top of the PBL.

2.3.1.2 Scales of atmospheric motions

Scales of Motion are categories used to describe weather features but nature is not easily classified. The sizes of features vary and may fit in more than one category. Orlanski (1975) proposed the horizontal scale of motion as a quantity for classifying atmospheric process. His proposal is as follows (1) Micro-scale, (2) Meso-scale, (3) Synoptic-scale, and (4) Large or Climatological-Scale.

Micro-scale is measured in meters with a time scale of minutes. It includes organized convective motions responsible for individual thunderstorm cells. The diameter of eddies are a few meters or less and may last only few minutes. Included in this group are turbulent eddies which is the primary transfer mechanism for momentum passing from the atmosphere into the sea.

Meso-scale is the next larger scale, which is measured in kilometers to hundreds of kilometers, with timescales of tens of minutes to hours. Meso-scale motions include land-sea breeze circulations, coastal fronts, thunderstorms, small tropical storms, flows over complex terrain and katabatic winds (winds cause by cold air flowing down slopes due to gravitational acceleration). The first signs of Coriolis effects are found in meso-scale motions.

Synoptic-scale is the next larger scale of atmospheric motion, which is measured in hundreds to thousands of kilometers, with timescales of days to a week. Synoptic scale motions include cyclones and tropical cyclones. This scale can be thought of as the, "weather map scale." Only circulations on the scale of pressure centers are distinguishable. This term has become somewhat specialized in referring to the use of meteorological data obtained simultaneously over a wide area for the purpose of providing a picture of the current state of the atmosphere.

Global or climactic scale is the next larger scale of atmospheric motion, which range includes the entire planet, with timescales of weeks. This scale of motion is strongly influenced by thermodynamic factors than by dynamic factors. Persistent surface temperature differentials

over large regions of the globe produce motions that can persist for very long time periods. Examples of events in this group include the El Nino Southern Oscillation (ENSO) episodes, variations in year-to year weather, changes in storm patterns and/or storm intensity, and long-term (secular) climatic variations.

2.3.1.3 Numerical weather prediction

Numerical weather prediction (NWP) uses mathematical equations for the physics and dynamics of the atmosphere to predict weather. Forecast models, use the power of supercomputers or clustered computers to provide predictions on many atmospheric variables such as temperature, pressure, wind, and rainfall.

Observed data from various weather instruments are collected and a numerical grid of observed data is calculated. This analysis dataset is then used as a starting point for the model to produce a forecast. Primitive equations are then applied to this atmospheric state to find new rates of change, and these new rates of change predict the atmosphere at a yet further time into the future. This procedure is continually repeated until the solution reaches the desired forecast time. The length of the time step is related to the distance between the points on the computational grid. Calculation time steps for global climate models may be on the order of tens of minutes, while time steps for regional models may be a few seconds to a few minutes.

NWP has become an indispensable tool but it is important to understand prediction limitations. The equations used to simulate the atmosphere are nonlinear and impossible to solve exactly. Numerical methods used to obtain solutions are generally approximated, which leads to prediction error. All atmospheric numerical models are based upon the same set of governing equations and differ by the following:

- How the equations are solved,
- What approximations and assumptions are made, and
- How one represents the physical processes in the physical parameterizations.

It is important to keep the sources of error in mind to make intelligent use of NWP data. Errors can be grouped into three categories: (1) initial condition errors, which arise from problems in data collection and interpretation, (2) model limitation errors, which are problems due to the ability of the model to take all factors of weather into account, and (3) model predictability errors, arise from the fact that forecast errors increase with time.

2.3.2 Synoptic-scale forecasts

Global models on the synoptic scale play a key role in wind-wave modeling. These models show weather systems on a large scale. Notably for disaster prevention, these models show development of pressure systems that generate hazardous high seas. Forecasting such events can prevent maritime accidents and pre-warn of approaching high surge along coastal areas. Models that use synoptic data show the general state of current ocean basin wave system. Synoptic scale models normally provide forecasts of three to five days and some even longer, out to sixteen days. Current models typically show skill at predicting out to around five days into the future. Since predictability of the atmosphere is not constant, forecast skill vary with location, weather situation, and season. This section describes available global synoptic NWP that contain 10m wind data that can be used as input into wind-wave models.

2.3.2.1 GFS & FNL

The Global Forecast System (GFS) is a NWP model primarily run and distributed by the National Centers for Environmental Prediction (NCEP). GFS is run four times a day (00, 06, 12C, and 18 UTC) and considered as a, "real-time dataset." The dataset consists of a global analysis grid along with 16 day forecasts in decreasing horizontal and temporal resolution over time. Forecast have a temporal resolution of three hours up to the 180 hour forecast then continue with a resolution of 12 hours up to the 384 hour forecast. The analysis grid of each run is produced by using observational data collected up to 2 hours and 45 minutes past the synoptic time.

The Final Global Data Assimilation System (FNL) is similar to the GFS and primarily run and distributed by NCEP. FNL is run four times a day and consists of a global analysis grid along with 3, 6, and 9 hour forecasts. The analysis grid of each run is produced by using, "first guess," data (3, 6, and 9 hour forecast from the previous synoptic time run) and observational data collected up to 6 hours past the synoptic time. FNL is the final run in the series of NCEP operational runs and this dataset is also known as, "Final Analysis or Final Run."

2.3.2.2 NARR

The North American Regional Reanalysis (NARR) from the NCEP is a long-term atmospheric and land surface hydrology dataset for the North American continent and considerable parts of adjacent oceans. This dataset has a horizontal resolution of 32 km and a vertical resolution of 45 layers. Spatial resolution is three hours and the dataset includes data from 1979 to present. NARR assimilates all available observational data into each corresponding analysis dataset. This data analysis uses all available observational data but is not considered as a, "real-time dataset," because there is a considerable delay in its availability.

2.3.2.3 GPV-GSM

The Grid Point Value - Global Spectral Model (GPV-GSM) is a synoptic scale NWP that is produced by the Japan Meteorological Agency (JMA). The GSM run four times a day (00, 06, 12, and 18 UTC) and considered a, "real-time dataset." The all runs have a temporal resolution of six hours for forecast data out to 84 hours. The 12 UTC dataset contains additional forecast from 96 hours out to 196 hours with a temporal resolution of twelve hours. The GSM has a spatial resolution of 0.50 degrees from the surface to the 100 hPa level, and continues to 10 hPa with a 1.0 degree spatial resolution. The GSM covers the entire globe and is provided in a GRIB2 World Meteorological Organization (WMO) standard format. Archived data is freely available for download from the internet but access to real-time data requires a fee.

2.3.3 Meso-scale forecast

Early operational weather models were only able to resolve synoptic-scale features. Advances in parallel processing and computational speed now allow NWP models to calculate meso-scale features. Calculation domains are generally limited to regional areas, since predicting meso-scale weather features requires much finer model resolution. Boundary condition information from synoptic-scale forecast is used to ensure continuity of the regional grid without using excessive amounts of valuable computer resources. Meso-scale forecast is important to local wind-wave domains because it detects smaller weather phenomena such as sea and land breeze motions and local wind eddies that produce local wind-waves.

2.3.3.1 WRF

The Weather Research and Forecasting (WRF) model is a meso-scale NWP designed to serve both operational forecasting and atmospheric research needs. It is an evolutionary successor to the MM5 model. The effort to develop WRF has been a collaborative effort among the National Center for Atmospheric Research (NCAR), the National Oceanic and Atmospheric Administration (NOAA), the National Centers for Environmental Prediction (NCEP) the Forecast Systems Laboratory (FSL), the Air force Weather Agency (AFWA), the Naval Research Laboratory, and many other research and academic organizations world-wide. Open collaboration and research is possible by WRF being covered under GPL. Many options for different parameterizations are available to tune WRF for different areas and seasons. The developed wind-wave system produces meso-scale forecast, with a spatial resolution of 10 km, for the Honshu area of Japan (between 33 to 36.2 latitude and 136.4 to 142.3 longitude). The model is run four times daily, with a temporal resolution of one hour, forecasting out to 72 hours. The GFS 1.0 degree dataset is used as input for the initial boundary conditions into the model.

2.3.3.2 GPV-RSM

The Grid Point Value - Regional Spectral Model (GPV-RSM), produced by the Japan Meteorological Agency (JMA), is a hydrostatic spectral model with a sigma-pressure hybrid vertical coordinate system. The model includes 40 vertical levels and has a horizontal resolution of 20 km covering an area between 20 to 50 latitude and 120 to 150 longitude. GPV-RSM is run twice a day (00 UTC and 12 UTC) with forecast out to 51 hours in three hour increments. This model uses the GPV-GSM to set up its lateral boundary conditions. JMA states the major objectives of RSM are: (1) to predict meso-scale phenomena over and around Japan, (2) to supply quantitative forecast of surface temperature, wind and precipitation, (3) to provide information for local aviation uses, and (4) to provide the lateral boundary condition for the GPV-MSM. Archived data is freely available for download from the internet but access to real-time data requires a fee.

2.3.3.3 GPV-MSM

The Grid Point Value - Meso-Scale Model (GPV-MSM) is a non-hydrostatic NWP grid model produced by JMA to provide additional information for disaster prevention and aviation safety. The GPV-MSM provides a 15 hour forecast every three hours: 00, 03, 06, 09, 12, 15, 18, and 21 UTC. The 03, 09, 15, and 21 UTC datasets contain forecast out to 33 hours. The forecast domain covers a rectangular area of about 3600 km x 2880 km, between 22.4 to 47.6 degrees latitude and 120 to 150 longitude, with a horizontal resolution of 5 km, 0.05 degrees by 0.0625 degrees (481 x 505 grid points). The MSM utilizes a Lambert conformal conic map projection with a vertical terrain following coordinate system. The upper boundary of the model is 21,800 meters and lower boundary at 40 m with 50 layers. GPV-MSM is provided in a GRIB2 WMO standard format.

Initial conditions are provided by the Meso-4D-Var and the lateral boundary conditions are provided by GPV-RSM. GTOPO30 is the data source of the model terrain. The data is smoothed so that the valid resolution of the model terrain is approximately 7.5 km. Archived data is freely available for download from the internet but access to real-time data requires a fee.

2.3.3.4 HAGPV

The Hourly Atmospheric Analysis Grid Point Value (HAGPV) is a NWP analysis of the horizontal wind and temperature fields produced hourly by JMA. The dataset contains wind and temperature fields for 17 atmospheric levels, including 10 m wind and 1.5 m temperature data at the surface. The configuration of HAGPV is listed in Table 2.1. The HAGPV grid covers the area between 22.4 to 47.6 degrees latitude and 120 to 150 longitude with a horizontal resolution of 0.05 degrees by 0.0625 degrees (481 x 505 grid points). The dataset is provided in a GRIB2 WMO standard format. The analysis uses the latest forecast from the meso-scale model (GPV-MSM) as the first guess, and the multivariate optimum interpolation

(OI) scheme is utilized to assimilate wind and temperature observational data. Wind observations assimilated are from WINDAS (Wind Profiler Network and Data Acquisition System), ACARS (Aircraft Communications Addressing and Reporting System), Satellite AMV (Atmospheric Motion Vector), and AMeDAS (Automated Meteorological Data Acquisition System). Temperature observations are obtained from ACARS and AMeDAS. WINDAS, established by JMA in April 2001, is a network of wind profiler sites. There are currently 31 wind profiler sites throughout Japan. Each site uses 300m vertical profiles of 10 minute averages of Doppler velocities on five beams that are measured every hour. Wind components (u, v, and w) are calculated and the dataset is available within 20 minutes after the hour. AMEDAS, established in November 1974 by JMA, is a high-resolution surface observation network. The network consists of about 1,300 stations with automatic observation equipment. These stations are located at an average interval of 17 km throughout Japan.

Data cut-off time is set to be at 20 minutes past the hour in order to distribute the products approximately 30 minutes past the hour.

Table 2.1 Configuration of the hourly analysis system

	surface analysis	upper air analysis
analysis scheme	2D optimum interpolation	3-dimensional optimum interpolation
assimilated observation	AMeDAS (wind, temperature)	wind profiler, Doppler radar (VVP wind), ACARS, hourly satellite wind, AMeDAS (temperature)
first guess	latest forecast from MSM (forecast time = 2-4 hours)	
analysis variable	horizontal wind (u and v components), temperature	
domain	MSM domain, grid spacing 5km, vertical levels up to about 150 hPa	
analysis time	on the hour, every hour (calculation starts at 20 minutes past the hour)	
product distribution	around 30 minutes past the hour	
Data format	GRIB2	

2.4 Wind-wave model

Numerical wave models allow computation of ocean parameters on global and regional scales with relative accuracy. Wind-wave prediction has greatly evolved over the last sixty years. The developed wind-wave system uses the third-generation wind-wave modal Simulating Waves Nearshore (SWAN) to calculate ocean forecast/hindcast parameters. Although SWAN specifically designed for coastal application, the developed wind-wave system employs it for both ocean and coastal applications. The basic calculation philosophy of SWAN is identical to WAM (WAMDI group 1988) for oceanic scales.

SWAN allows the use of two different energy transfer models for calculations. The first from WAM cycle 3 based on formulations of Komen et al. (1984) and the second from WAM cycle 4 (Komen et al. 1994) based on formulations of Janssen (1991). Lalbeharry et al. (2004) states the implementation of Janssen (1991) as implemented in SWAN is different from WAM cycle 4 and proposes a modification. Modifications as proposed by Lalbeharry et al. (2004) has been implemented and tested in the developed wind-wave system. Details of modifications are provided in Section 2.4.3.2.1.2, Modified wind growth formulation in SWAN, and tests are provided in Chapters 3, 4, and 5.

This section describes the evolution of wind-wave models to where they are today, the concepts of the ocean wave spectra, and the governing equations bounding the spectral description of waves as implemented in SWAN.

2.4.1 Model classifications

The foundation for early wave models were laid by Sverdrup and Munk (1947), where the relationships of various wave-generation parameters to resulting wave conditions were documented through the use of empirical wind sea and swell laws. They determined that significant wave height and significant period could be directly related to wind speed, fetch, and duration. Their method of prediction was called a parameter method, because the method was describe using wave height, wind speed, fetch length and duration as input parameters. Bretschneider (1952) completely reformulated this empirical formula using the most accurate observational data available at that time.

Pierson et al. (1955) refined wind-wave prediction by showing that wave generation was best described through the concept of a wave spectrum. They examined how a turbulent wind field interacts with a random sea surface, and showed that a frequency spectrum could be constructed from various wind speeds, fetch lengths and durations. Their method was based on study by Neumann (1953) where the wave spectrum was derived from an empirical formula for wave slope.

Phillips (1957) and Miles (1957) were the first to describe wave generation processes through mathematical theories. Following Phillips (1960) study of nonlinear energy transfer S_{nl}, Hasselmann (1962) identified and mathematically described the weak nonlinear interactions between waves due to a resonant mechanism. Hasselmann (1962) proposed an energy transport equation for wind wave spectra, where the physical processes of wave growth, and decay were considered separately. The processes were described as a source function, consisting of three terms representing the input from the wind, nonlinear transfer, and dissipation by white-capping (or bottom friction). The general energy transport equation proposed by Hasselmann provided the basic framework for early wind-wave models and in a form is still used today.

2.4.1.1 First and second generation models

The terms, "first generation model," and, "second generation model," were first mentioned by SWAMP (1985). According to the distinction made by SWAMP, first generation models neglect nonlinear wave-wave interactions, and second generation models describe them, but in a simplified parameterized form. First generation models are also known as decoupled discrete models because they neglect the coupling of wave-wave interactions across spectral components. Conversely second generation models are alternatively called coupled discrete models.

First generation wave models were based on empirical relationships between wave-height, wave-length, wind speed, fetch length, and duration. The development of the wave spectrum allowed evolution of individual wave components with frequency σ traveling in direction θ of the directional wave spectrum $E(\sigma, \theta)$, using the energy balance equation for deep-water applications:

$$\frac{\partial E}{\partial t} + \vec{c}_g \cdot \vec{\nabla} E = \sum S_i \tag{2.1}$$

where $E = E(\sigma, \theta, x, t)$ varies in space (x) and time (t). Group velocity is represented by $\vec{c}_g$. On the left hand side of Eq. (2.1), the first and second terms describe the local change of the two-dimensional wave spectrum, and the divergence of the wave energy flux, respectively. Parameter S_i on the right hand side of Eq. (2.1) defines the source/sink terms. Theoretically, the total sum all source/sink terms is balanced where the energy source term transfers energy in and the sink term removes energy out from the equation.

Early models focused on wind input mechanisms and nonlinear wave-wave interactions were not considered explicitly. According to Miles and Phillips, momentum was transferred from winds to the ocean surface through two input terms:

1) a turbulent atmospheric pressure forcing process, and
2) a linear feedback process.

Based on the wind input equation, growth would never stop and additional work on the universal equilibrium range by Phillips (1958) proposed a method to control wind-wave growth. Phillips, postulated that wave breaking leads to a balance of wave growth and dissipation. Pierson and Moskowitz (1962) formulated a limit of the frequency spectrum, PM spectrum, where the equilibrium range of the wind-wave spectrum is expressed by a simulated f^5 high-frequency tail. Models that enhance the wind input and impose a high-frequency tail to simulate the effects of quadruplet wave-wave interactions and white-capping to prevent regions of the wind-wave spectrum from exceeding a determined saturation level are referred to as first-generation models.

The foundation of second generation models can be attributed to Hasselmann (1962), where the concept of nonlinear wave-wave interaction was introduced. Nonlinear wave-wave interactions seemed to explain the transfer of energy between frequency bands and migration of the spectral peak toward lower frequencies in the spectrum. The concept of S_{nl} and its effect on the ocean wave spectrum gained general acceptance after ground breaking work on the Joint North Sea Waves Project (JONSWAP) in the North Sea. Hasselmann et al. (1973) showed, with JONSWAP, the importance of nonlinear wave-wave interactions to the growth of low frequency spectral components. Key findings in their study formed the framework for more efficient source term parameterizations in modern 2G models. Notable accomplished findings by Hasselmann et al. (1973) were:

1) Developed the JONSWAP spectrum from analysis of observations,
2) Demonstrated short wave energy generated by the Miles mechanism is transferred to wave with frequencies slightly lower than the frequency of waves at the peak of the spectrum. In addition, wave speed eventually is greater than the wind as noted by Pierson and Moskowitz,
3) Confirmed earlier findings of Mitsuyasu (1968), and showed a clear relationship between Phillips equilibrium constant ($\alpha = 0.0081$) and non-dimensional fetch,
4) Discovered that the ocean wind-wave spectrum is never fully developed.

The SWAMP study (1985) compared nine different first and second generation models using hypothetical conditions including a test that considered the response of the models to a hurricane wind field. SWAMP (1985) demonstrated that, although second generation models showed a significant improvement over first generation models, deficiencies still existed. It was found that wave spectra showed much more variability than was originally assumed in parametric models, and two-dimensional aspects were more important than expected. Development of various spectral distributions in different input conditions could only be controlled by restraining the spectrum to a predetermined level. According to SWAMP (1985), a full spectral model with explicit representation for the physical processes relevant for wave evolution was needed. This spectral model needed to include a two-dimensional description of the sea state.

2.4.1.2 Third generation models

Third generation models generally share the following characteristics:

1) Ocean wave spectrum is free to develop without an a priori limit on the spectral shape. The resulting spectrum is defined purely from the balance in the source/sink terms.
2) Nonlinear wave-wave interaction source term is solved explicitly, and is consistent with the same number of degrees of freedom as the discrete representation of the spectrum.
3) Source/sink mechanisms are defined discretely in the frequency/direction domain, and not formulated by parameterization.

Differences in third generation models are normally in differences of the source/sink term expressions, especially in the nonlinear wave-wave interaction term, S_{nl}.

Hasselmann and Hasselmann (1981) proposed a third generation model, EXACT-NL, describing an explicit method for calculating the mean exchange of energy between wave components within a spectrum. This model is based on the six-dimensional integral expression proposed by Hasselmann (1962) and includes a representation of the dissipation source term, incorporating assumptions of energy dissipation through whitecap breaking by Hasselmann (1974). EXACT-NL showed success in predicting the overall characteristics of the wave spectrum but its approach demanded large computational processing. Hasselmann et al. (1985) introduced Discrete Interaction Approximation (DIA) method to compute the nonlinear transfer in a surface wave spectrum in an attempt to reduce the overall computational time needed to solve for spectral energy balance. DIA relaxes most of the constraints on spectral shape in simulating wave growth in the parameterization of the nonlinear wave-wave interaction source terms. The success of DIA is documented in Komen et al. (1994).

The Wave Modeling group (WAMDI 1988) was formed with the goal of developing a third generation model that could be implemented operationally on global as well as regional scales, to replace existing second generation models implemented operationally. The group utilized the success of EXACT-NL (Komen et al., 1994) and developed the Wave Modeling (WAM) model. The success of WAM greatly can be attributed to the DIA algorithm for its ability to approximate S_{nl} with very low computational cost.

The DIA algorithm has allowed independent development of other third generation models. Tolman and Chalikov (1996) present new formulations for source terms. S_{in} source term is based on Chalikov and Belevich (1993) and S_{nl} is based on DIA of Hasselmann et al. (1985). S_{ds} is divided into two constituents, a low and a high-frequency source term.

Ris (1997) and Booij et al. (1999) implemented the third generation model, SWAN, for shallow waters and enclosed basins. SWAN computes the evolution of wind waves in coastal regions using the wave action balance equation. This model shares the basic scientific philosophy as WAM of incorporating the formulations for deep water process of wave

generation, dissipation and the quadruplet wave-wave interactions. Although designed for coastal regions, SWAN can also be used on global and regional scales since it is an extension of WAM.

2.4.2 Wave spectrum

Waves are created by the induced surface pressure as winds blow over the ocean surface. The effect is momentum transferred from the atmosphere to the ocean, and the creation of arced ripples. As the wind continues to blow, the ripples increase in height and decrease in frequency. Transferred momentum is in the form of energy and there is little mass motion of the water in the direction of travel as the energy moves through the water. The travel of energy forms sine waves on the ocean surface.

Waves created by the local wind are known as wind waves and are generally still under the influence of the local wind in the generating area. These waves are composed of an infinite number of sine waves superimposed on each other and have a large spectrum or range of frequencies. Wind waves are very irregular in size, direction, and speed. Wave speed gradually increases until they travel at nearly the speed of the wind. At this point, resistance causes energy loss and the cease of wave growth in height and frequency. As waves leave the generating area, they are no longer under the developing influence of the generating wind. These waves interact with each other and increase in size through wave-wave interactions and decrease through white-capping. Swell waves have frequencies smaller than that of wind waves.

The wave spectrum is a term that describes the spectral technique used to describe ocean waves mathematically in the form of a distribution of wave energy with frequency and direction. Total energy present in ocean waves is the sum of all harmonic sine waves present.

2.4.2.1 Random-phase/amplitude model

Holthuijsen (2007) uses the random-phase/amplitude model as a model for describing ocean waves. The moving surface elevation $\mu(t)$ is considered to be the sum of a large number of harmonic waves as shown in the Fourier series Eq. (2.2),

$$\mu(t) = \sum_{i=1}^{N} a_i \cos(2\pi\sigma_i t + \alpha_i) \tag{2.2}$$

Where N is a large number of frequencies, and amplitude a and phase α are random variables. In this model, wave frequencies are normally between 0.05 – 1.0 Hz. At every frequency σ_i there is a uniform distribution for the random phase (between 0 and 2π) and a Rayleigh distribution for the random amplitude. Phase is ignored, since it is a uniform distribution, and the result is shown as an amplitude spectrum. The amplitude spectrum describes sea-surface as a stationary, Gaussian process, at time t (at one location).

2.4.2.2 Variance density spectrum

The variance of each wave component $E\left\{\frac{1}{2}a_i^2\right\}$ is used because (1) statistically variance is a more meaningful quantity than amplitude, and (2) linear theory shows for surface gravity waves, the energy of waves is proportional to the variance. The variance spectrum is a summation of individual wave components at discrete frequencies σ_i, but continuous frequencies are present at sea. Therefore the variance $E\left\{\frac{1}{2}a_i^2\right\}$ is distributed over the frequency interval $\Delta\sigma_i$ at frequency σ_i.

$$E^*(\sigma_i) = \frac{1}{\Delta\sigma_i} E\left\{\frac{1}{2}a_i^2\right\} \qquad \text{for all } \sigma_i \tag{2.3}$$

The above equation represents the spectrum where all frequencies are defined but still discontinuous from one frequency band to the next. Continuity of the variance density spectrum is achieved by allowing the width of the frequency bands $\Delta\sigma_i$ approach zero

$$E(\sigma) = \lim_{\Delta\sigma\to 0} \frac{1}{\Delta\sigma} E\left\{\frac{1}{2}a_i^2\right\} \tag{2.4}$$

To describe moving waves a horizontal dimension is added, where θ represent the direction of wave propagation. A continuous two-dimensional variance density spectrum can be described by the following formula:

$$E(\sigma,\theta) = \lim_{\Delta\sigma\to 0}\lim_{\Delta\theta\to 0} \frac{1}{\Delta\sigma\Delta\theta} E\left\{\frac{1}{2}a_i^2\right\} \tag{2.5}$$

The above two-dimensional variance density spectrum represents the stationary Gaussian surface elevation at a given time t at one geographic point. To predict the spectrum at a given location in the ocean we need to follow each wave component across the ocean from its point of inception to the prediction point and account for all effects of generation, wave-wave interaction and dissipation encountered.

$$E(\sigma,\theta) = E(\sigma,\theta;x,y,t) \tag{2.6}$$

2.4.3 Governing equations and functions

The sea surface is commonly described as a wave variance spectrum or energy density $E(\sigma, \theta)$. Third-generation models use the Eulerian formulation to calculate $E(\sigma, \theta)$. Where, the spectrum is simultaneously computed for a large number of locations in the forecast area. The forecast area is treated as grid (geographic or Cartesian) and energy balance is maintained in each cell. The spectral energy balance can be expressed by the following formula:

$$\frac{\partial E(\sigma,\theta;x,y,t)}{\partial t}+\frac{\partial c_{g,x}E(\sigma,\theta;x,y,t)}{\partial x}+\frac{\partial c_{g,y}E(\sigma,\theta;x,y,t)}{\partial y}=S(\sigma,\theta;x,y,t) \tag{2.7}$$

Where the first term on the left-hand side represent the change of energy in the cell. The second and third terms represent the net import of energy in the x and y direction respectively. The term on the right-hand side represent the locally generated energy.

2.4.3.1 Wave action balance equation

Action density is defined as $N = E/\sigma$ and is conserved during propagation in the presence of ambient current, whereas energy density E is not (Whitham, 1974). Evolution of the action density $N(\lambda, \varphi, t, \sigma, \theta)$ on a spherical coordinate grid is determined in terms of space (longitude λ, latitude φ), and time t. The energy density is defined by Eq. (2.8).

$$\frac{\partial N}{\partial t}+\frac{\partial c_{\lambda}N}{\partial \lambda}+\cos^{-1}\varphi\frac{\partial c_{\varphi}\cos\varphi N}{\partial \varphi}+\frac{\partial c_{\sigma}N}{\partial \sigma}+\frac{\partial c_{\theta}N}{\partial \theta}=\frac{S_{tot}}{\sigma} \tag{2.8}$$

2.4.3.2 Source term functions

The source/sink term described in terms of energy density, on the right-hand side of Eq. (2.8), represents physical processes which generate, dissipate, or redistribute wave energy. In SWAN, S_{tot} includes six processes as shown in Eq. (2.9).

$$S_{tot}=S_{in}+\left[S_{nl3}+S_{nl4}\right]+\left[S_{ds,wc}+S_{ds,bf}+S_{ds,br}\right] \tag{2.9}$$

The source term S_{tot} can be described as follows:

- S_{in} represents the wind induced generation of waves,
- S_{nl3} and S_{nl4} represent the redistribution of wave energy through non-linear wave to wave interactions, and
- $S_{ds,wc}$, $S_{ds,bf}$ and $S_{ds,br}$ represent the dissipation of energy from white-capping, bottom friction, and depth-induced wave breaking respectively.

2.4.3.2.1 Generation by wind, S_{in}

Third generation models express the generation of waves in many ways but the basis of all formulation in the source term is described by the sum of a linear wave growth mechanism by Phillips (1957) and an exponential mechanism by Miles (1957). Numerically wind growth is described by Eq. (2.10) where coefficients A (linear growth) and B (exponential growth) are dependent on wave frequency and direction, along with, wind speed and direction:

$$S_{in}(\sigma,\theta) = A + BE(\sigma,\theta) \tag{2.10}$$

Early stages of wave growth are expressed as a linear function of time. As waves become steep the boundary between the ocean surface and atmosphere becomes distorted and wave growth becomes exponential with time. Most operational wave models ignore the initial linear resonance mechanism because small waves are always present to trigger wave growth.

2.4.3.2.1.1 Wind growth formulation in SWAN

SWAN offers two options for wind growth that can be optionally set. The first option was taken from the WAM Cycle-3 model (WAMDI group 1988) and is based on formulations of Komen et al. (1984). The second option was taken from the WAM Cycle-4 model (Komen et al. 1994) and is based on formulations of Janssen (1991), where wind and waves are coupled by having a feedback of growing waves on the wind profile. Feedback enhances the growth of younger wind waves over older wind waves for the same source wind.

Selecting the first option activates source term formulations by Komen et al. (1984) and the wind speed at 10m U_{10} is used as input, but friction velocity U_* as transformed by WAM Cycle 3, is used for calculation:

$$U_* = C_D U_{10}^2, \tag{2.11}$$

$$C_D(U_{10}) = \begin{cases} 1.2875\times10^{-3} & \text{for } U_{10} < 7.5\text{m/s} \\ \left(0.8 + 0.065\times10^{-3}\right) & \text{for } U_{10} \geq 7.5\text{m/s} \end{cases}, \tag{2.12}$$

where C_D is the drag coefficient as described by Wu (1982).

Selecting the second option activates the formulations by Janssen (1991). Janssen (1991) shows, the wind friction speed can be estimated using the logarithmic wind profile if the sea roughness is known or assumed and expressed by:

$$U_{(z)} = \frac{U_*}{k}\ln\left[\frac{z + z_e - z_0}{z_e}\right] \quad , \quad k = 0.41 \tag{2.13}$$

$$z_e = \frac{z_0}{\sqrt{1-\left|\vec{\tau}_w\right|/\left|\vec{\tau}\right|}} \quad , \quad z_0 = z_{ch}\frac{U_*}{g} \quad , \quad z_{ch} = 0.01 \tag{2.14}$$

where $U_{(z)}$ is the wind speed at height z (above the mean water level), k is the Von Karman constant, and z_e is the effective surface roughness length, z_0 is the roughness length, and is the Charnock (1955) parameter.

Janssen (1991) parameterized the sea roughness in terms of wave induced stress τ, which depends on the wave spectrum. Total surface stress is expressed as:

$$\vec{\tau} = \rho_a \left|\vec{U}_*\right| \vec{U}_* \tag{2.15}$$

where ρ_a is the atmospheric density. Wave stress $\vec{\tau}$ is given by:

$$\vec{\tau}_w = \rho_a \int_0^{2\pi}\int_0^{\infty} \sigma BE(\sigma,\theta)\frac{\vec{k}}{k} d\sigma d\theta \tag{2.16}$$

U_* can be determined for a given wind speed U_{10} and a given wave spectrum $E(\sigma,\theta)$.

2.4.3.2.1.2 Modified wind growth formulation in SWAN

Lalbeharry et al. (2004) showed that the Janssen et al. (1991) implementation in SWAN is not as implemented in WAM 4.5. Lalbeharry et al. (2004) documents improvement in both significant wave height and wave period when modifying the SWAN implementation. Lalbeharry et al. (2004) notes two specific differences in the implementation of SWAN and WAM 4.5. First, the shift growth parameter $z_\alpha = 0.011$ in the wave growth source term is omitted. Second, the wave growth limiter in the exponential wind growth source term differs between SWAN and WAM 4.5. Janssen formulation in SWAN is implemented using a limiter as described by Ris (1997) in terms of action density and σ:

$$\left|\Delta N(\sigma,\theta)\right|_{\max} = (0.1\alpha_{PM})/(2\sigma k^3 c_g) \tag{2.17}$$

where:

$$\alpha_{PM} = 0.0081 \tag{2.18}$$

and the limiter in WAM 4.5 is based on the formulation of Hersbach and Janssen (1999) where:

$$\left|\Delta N(\sigma,\theta)\right|_{\max} = (2\pi)^2 \times 3.0\times 10^{-7}\, g u_* \sigma_c \Delta t/(\sigma^3 k) \tag{2.19}$$

where:

$$u_* = \max\left(u_*, gf^*_{PM} / f\right)$$
$$f^*_{PM} = 5.6\times10^{-3} \tag{2.20}$$

is the dimensionless Pierson-Moskowitz frequency.

2.4.3.2.1.3 Linear growth term

The expression for *A*, as implemented in SWAN, for shallow water is derived from Calvaleri and Malanotte-Rizzoli (1981), with a filter that limits growth lower than the Pierson-Moskowitz frequency as described by Tolman (1992):

$$A = \begin{cases} \dfrac{1.5\times10^{-3}}{2\pi g^2}\left(U_* \max\left[0, \cos\left(\theta-\theta_w\right)\right]\right)^4 H & \text{for } \left|\theta-\theta_{wind}\right| \le 90^\circ \\ 0 & \text{for } \left|\theta-\theta_{wind}\right| > 90 \end{cases}, \tag{2.21}$$

$$H = \exp\left\{-\left(\frac{\sigma}{\sigma^*_{PM}}\right)^{-4}\right\}, \qquad \sigma^*_{PM} = \frac{0.13g}{28U_*}2\pi \tag{2.22}$$

where θ_w is the wind direction, *H* is the growth filter, and σ^*_{PM} is the peak frequency of the fully developed sea state as described by Pierson and Moskowitz (1964).

2.4.3.2.1.4 Exponential growth term

SWAN offers two options for wind growth as mentioned previously in this section, formulations by Komen et al. (1984), and formulations by Janssen (1991). These two transfer models mainly differ in the S_{in} and S_{ds} source terms. The S_{in} source term differ as described previously and the S_{ds} source term use different formulation constants in wave energy dissipation.

Selecting the first option uses formulations of Komen et al. (1984) and is expressed as a function of U_*/c_{ph} :

$$B = \max\left[0, 0.25\frac{\rho_a}{\rho_w}\left(28\frac{U_*}{c_{ph}}\right)\cos\left(\theta-\theta_w\right)-1\right]\sigma \tag{2.23}$$

where c_{ph} is the phase speed, ρ_a is the air density, and ρ_w is the water density.

Selecting the second option uses formulations of Janssen (1989, 1991), commonly referred to as the quasi-linear wind-wave theory, and is implemented in SWAN where β is the, "Miles constant":

$$B = \beta \frac{\rho_a}{\rho_w} \left(\frac{U_*}{c_{ph}} \right) \max\left[0, \cos\left(\theta - \theta_w \right) \right]^2 \sigma \,, \tag{2.24}$$

$$\begin{cases} \beta = \dfrac{1.2}{k^2} \lambda \ln \lambda^4 & , \quad \lambda \le 1 \\ \lambda = \dfrac{g z_e}{C_{ph}^2} e^{\tau} & , \quad \tau = \dfrac{kc}{U_* \cos\left(\theta - \theta_w \right)} \quad , \quad k = 0.41 \end{cases} \tag{2.25}$$

2.4.3.2.2 Nonlinear wave-wave interactions

Nonlinear wave-wave interaction is the mechanism that affects wave growth, where energy is transferred between waves from one component to another through resonance. Energy is neither gained nor loss in this mechanism and only redistributed over the spectrum. The basic principles of wave-wave interactions were discovered by Phillips (1960) and Hasselmann (1962). In deep and intermediate oceanic areas, quadruplet (four-wave) interactions allow energy transfers from the spectral peak to lower frequencies. Quadruplet wave-wave interaction occurs when the diamond pattern created by two pairs of wave components has matching wave numbers and frequencies, are superimposed:

$$\begin{aligned} f_1 + f_2 &= f_3 + f_4 \\ k_1 + k_2 &= k_3 + k_4 \end{aligned} \,, \tag{2.26}$$

with frequency f and wave number k.

In areas with shallow water depth, triad (three-wave) interactions are important where energy is transferred from lower frequencies to higher frequencies. Triad interactions occur when two wave components interact with a third wave component and proper resonance conditions exist.

2.4.3.2.2.1 Quadruplets, S_{nl4}

The computation of quadruplet wave-wave interactions require considerable computer resources due to the large number of quadruplets interactions involved in the ocean. For this reason SWAN calculates quadruplet wave-wave interactions in deep water using the Discrete Interaction Approximation (DIA) method as proposed by Hasselmann et al. (1985), slightly adapted by Tolman, which considers the interactions of each wave component in the spectrum in only two quadruplets.

$$\begin{aligned}\sigma_1 &= \sigma_2 = \sigma,\\ \sigma_3 &= \sigma(1+\lambda) = \sigma^+,\\ \sigma_4 &= \sigma(1-\lambda) = \sigma^-\end{aligned} \tag{2.27}$$

where, $\lambda = 0.25$ is a constant coefficient. The wave-number vectors with frequencies σ_3 and σ_4 lie at angles of θ_1 = -11.5º and θ_2 = -11.5º to the other two wave-number vectors that are identical to each other in frequency, wave number, and direction. The second quadruplet is a mirror of the first quadruplet where θ_1 and θ_2 are inverted. The corresponding source term in deep water for the quadruplet wave-wave interactions is:

$$S_{nl4}(\sigma,\theta) = S^{*}_{nl4}(\sigma,\theta) + S^{**}_{nl4}(\sigma,\theta) \tag{2.28}$$

where $S^{*}_{nl4}(\sigma,\theta)$ represents the first quadruplet configuration and $S^{**}_{nl4}(\sigma,\theta)$ refers to the second.

The source term for quadruplet interactions in finite water depth is taken from Hasselmann and Hasselmann (1981),

$$S_{nl4,\,finitedepth} = R\left(k_{peak,JONSWAP}d\right) S_{nl4,\,finitedepth} \tag{2.29}$$

where $k_{peak,JONSWAP}$ is the peak wave number of the JONSWAP spectrum of the original computation. In swan, $k_{peak,JONSWAP}$ is replaced with 0.75 times the mean wave number: $k_{peak,JONSWAP} \rightarrow k_p = 0.75\overline{k}$ (Komen et al., 1994). The coefficient values are C_1 = 5.5, C_2 = 6/7 and C_3 = -1.25. A maximum value of R = 4.43 is imposed to avoid unrealistically high values.

2.4.3.2.2.2 Triads, S_{nl3}

Triad wave-wave for shallow coastal regions is implemented in SWAN based on the Lumped Triad Approximation (LTA) by Eldeberky (1996). LTA is adapted from the Discrete Triad Approximation DTA of Eldeberky and Battjes (1995) where

$$S_{nl3}(\sigma,\theta) = S^{-}_{nl3}(\sigma,\theta) + S^{+}_{nl3}(\sigma,\theta)\ , \tag{2.30}$$

$$S^{-}_{nl3}(\sigma,\theta) = \max\left\{0, \alpha_{EB}\,2\pi c c_g J^2 \left|\sin(\beta)\right| \left\{E^2(\sigma/2,\theta) - 2E(\sigma/2,\theta)E(\sigma,\theta)\right\}\right\}\ , \tag{2.31}$$

$$S^{-}_{nl3}(\sigma,\theta) = 2S^{+}_{nl3}(2\sigma,\theta) \tag{2.32}$$

where the tunable proportionality coefficient is α_{EB} = 0.1 in SWAN (default setting). The bi-phase β is approximated with:

$$\beta = -\frac{\pi}{2} + \frac{\pi}{2}\tanh\left(\frac{0.2}{U_r}\right), \tag{2.33}$$

$$U_r = -\frac{gH_{m_0}\overline{T}^2}{\left(8\sqrt{2}\pi^2 d^2\right)}, \tag{2.34}$$

$$T = \frac{m_0}{m_1} \tag{2.35}$$

where Ursell number U_r, zeroth moment m_0 and first moment m_1 of the variance density spectrum $E(f)$ and δ = 0.2. The triad wave-wave interaction is only calculated for Ursell number $U_r > 0.1$. The interaction coefficient J is taken from Madsen and Sorensen (1993):

$$J = \frac{k_{\sigma/2}^2\left(gd + 2c_{\sigma/2}^2\right)}{k_\sigma d\left(gd + \frac{2}{15}gd^3k_\sigma^2 - \frac{2}{5}\sigma^2 d^2\right)} \tag{2.36}$$

2.4.3.2.3 Dissipation of wave energy

The evolution of deep-water wind-waves is very dependent on wave breaking. Spectral dissipation of wave energy is mostly assumed to be from wave breaking. Spectral dissipation is the lease understood mechanism in the modeling of wind-wave evolution. Holthuijsen (2007) states there is no generally accepted precise definition of breaking and quantitative observations are difficult to perform. Dissipation of wave energy of wave breaking is classified into three groups: white-capping, bottom friction, and depth-induce wave breaking

2.4.3.2.3.1 White-capping S_{ds}

White-capping occurs in the open ocean when the wave height becomes too large as compared to its wavelength. Hasselmann (1974) proposed a spectral dissipation model where each white-cap acts as a pressure pulse on the forward face of breaking waves. Each pressure pulse exerts negative work on the water surface, in effect acting against the rising sea surface and decreasing wave energy.

2.4.3.2.3.2 Formulation Review

Quasi-linear (WAM3) Komen et al. (1984) described quasi-linear dissipation source term as:

$$S_{ds} = -C_{ds}\left(\frac{s}{s_{PM}}\right)^{2m}\left(\frac{k}{k_m}\right)\omega_m F(\omega,\theta) \tag{2.37}$$

where C_{ds} is tuning coefficient, k_m and ω_m are the mean wave number and mean angular frequency, θ is the wave direction, $s_{PM} = \sqrt{4.57 \times 10^{-3}}$ is the integrated steepness of a fully developed Pierson-Moskowitz spectrum, respectively. The default WAM Cycle 3 (WAM3) uses $C_{ds} = 2.36 \times 10^{-5}$ and $m = 2$. The definition of ω_m and E_{tot} are

$$E_{tot} = \int\int E(\omega,\theta) d\omega d\theta \tag{2.37}$$

$$\omega_m = \left[\frac{1}{E_{tot}} \int\int \frac{1}{\omega} E(\omega,\theta) d\omega d\theta \right]^{-1} \tag{2.38}$$

Eq. (2.37) was evaluated more general form to adjust wave number dependence for WAM Cycle 4 (WAM4).

$$S_{ds} = -C_{ds} \left[(1-\delta) \left(\frac{k}{k_m} \right) \delta \left(\frac{k}{k_m} \right)^2 \right]^{n/2} \left(\frac{s}{s_{PM}} \right)^{2m} \omega_m F(\omega,\theta) \tag{2.39}$$

The WAMC3 setup has $\delta = 0$ and $n = 2$ and WAMC4 setup has $\delta = 1/2$ and $n = 1$. These formulations were based on Hasselmann, (1974). The quasi-linear model of S_{ds} is too strongly weighted by the mean angular frequency. Unphysical behavior in the presence of swells has been reported (Holthuijsen and Booij, 2000). SWAN allows white-capping dissipation formulation of WAMC3 and WAMC4.

Saturation based S_{ds} Alves and Banner (2003) experimentally found that dissipation is related to the nonlinear hydrodynamics within waves groups and a proposed saturation based S_{ds} term based on frequency-local spectrum saturation parameter.

$$S_{ds} = -C_{ds} \left[\frac{B(k)}{B_r} \right]^{p/2} s^{2m} \left(\frac{k}{k_m} \right)^n \omega_m E(\omega,\theta) \tag{2.40}$$

Where $B(k)$ is azimuth-integrated spectral saturation parameter

$$B(k) = \int k^4 E(k,\theta) d\theta \tag{2.41}$$

and B_r is a tunable parameter ranging from 3×10^{-3} to 4.25×10^{-3}, p is the exponent constant which has two different asymptotic behaviors.

$$p = \frac{p_0}{2}\left\{1 + \tanh\left\{10\left[\left(\frac{B(k)}{B_r}\right)^{1/2} - 1\right]\right\}\right\} \tag{2.42}$$

Where p_0 is the constant that need to be determined numerically. Alves and Banner (2003) defined p_0 equal to 4 and 8 for young and old sea conditions that leads to p = 2 and 4 respectively. The alternative form of Eq. (2.40) in frequency domain can be defined:

$$S_{ds} = -C_{ds}\left[\frac{B(k)}{B_r}\right]^{p/2} s^{2m}\left(\frac{k}{k_m}\right)^{n} \omega_m F(\omega,\theta) \tag{2.43}$$

$$B(k) = \int \frac{d\omega}{dk} k^3 F(\omega,\theta) d\theta = c_g k^3 F(\omega) \tag{2.44}$$

2.4.3.2.3.3 Formulation comparison and discussion

This section compares and discusses the white-capping formulations of (1) Komen et al. (1984) to be referred to as Komen, (2) WAM Cycle 3 as implemented in SWAN referred to as SWAN3, (3) WAM Cycle 4 as implemented in SWAN referred to as SWAN4, (4) WAM Cycle 4 referred to as WAMC4, (5) Alves and Banner (2003) referred to as AB.03.

Fig. 2.1 shows a comparison of white-capping dissipation formulation during wind-swell condition with values (wavelength, wave height, and wave period respectively): $\gamma = 2.0$, $H_s = 3m$, $T_s = 7s$; and swell with values: $\gamma = 3.3$, $H_s = 1m$, $T_s = 15s$. Fig. 2.2 shows a comparison of white-capping dissipation formulation during wind-swell condition with values $T_s = 15s$ (wavelength, wave height, and wave period respectively): $\gamma = 2.0$, $H_s = 3m$, $T_s = 7s$; and swell with values: $\gamma = 3.3$, $H_s = 3m$,.

For wind-sea condition where swell wave height is low, the quasi-linear based dissipation of Komen, WAMC4, SWAN3, and SWAN4 show under prediction of energy density at lower frequencies, accuracy is shown in wind swell areas of the spectrum but over predicted at higher frequencies in the tail. Komen shows larger over prediction in the higher frequencies when compared to SWAN formulations. Saturation based dissipation of AB03 show good overall accuracy of prediction with higher under prediction in the lower frequencies than quasi-linear based dissipation and slight over prediction in the higher frequencies.

For wind-sea conditions where swell wave height is high, quasi-linear based dissipation still under predicts energy density at lower frequencies but over predicts at higher frequencies. All quasi-linear base formulation show similar tendencies of over prediction at the tail end of the spectrum. Komen show highest over prediction at the peak of wind-sea part of the spectrum. Saturation based dissipation of AB03 under predicts at lower frequencies, with better prediction at higher frequencies over quasi-linear based dissipation.

Comparing both wind-sea conditions for swell shows the following:

1. SWAN predicts lower dissipation in the wind-sea part of the spectrum with the presence of swell.
2. Komen show dependence of wind-sea dissipation on swell.
3. SWAN formulation shows an independence of wind-sea dissipation on swell. Holthuijsen and Booiji (2000) suggested removal of the dependence of wind-sea dissipation on swell by making dissipation at a particular frequency a function of the mean wave number and steepness of only the frequencies higher than itself.
4. AB03 show similar prediction with and without the presence of swell.

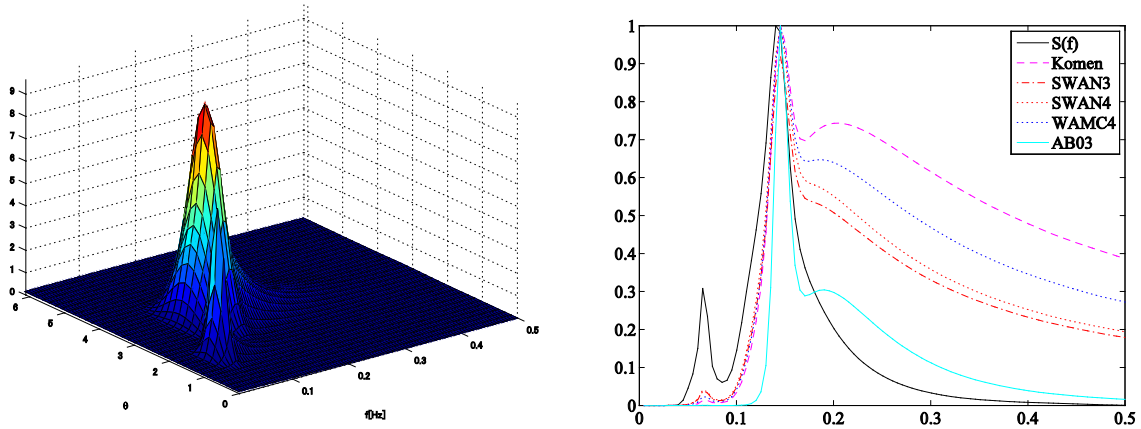

(a) Directional Spectra (b) normalized S_{ds}

Fig. 2.1 Wind-swell condition (Wind sea: $\gamma = 2.0$, $H_s = 3m$, $T_s = 7s$; Swell: $\gamma = 3.3$, $H_s = 1m$, $T_s = 15s$)

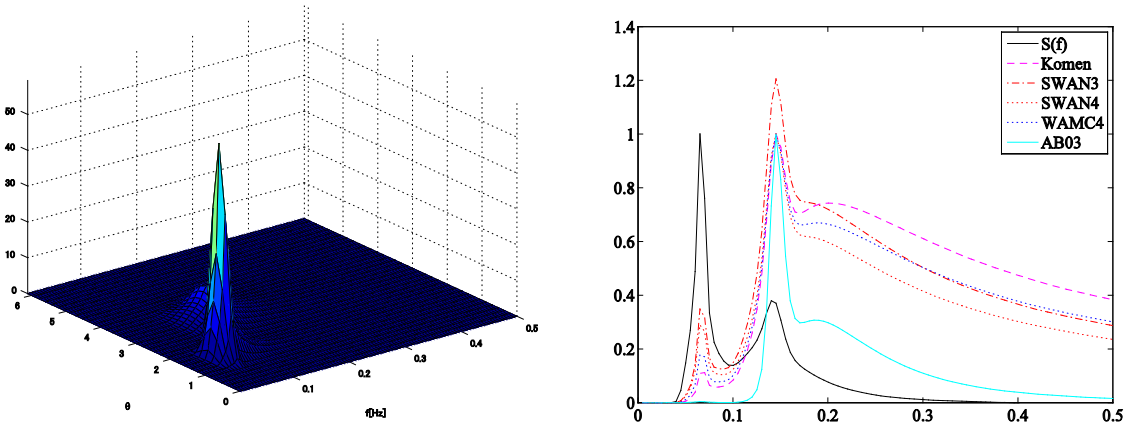

(a) Directional Spectra (b) normalized S_{ds}

Fig. 2.2 Wind-swell condition (Wind sea: $\gamma = 2.0$, $H_s = 3m$, $T_s = 7s$; Swell: $\gamma = 3.3$, $H_s = 3m$, $T_s = 15s$)

2.4.3.2.3.4 Bottom friction, $S_{d,bf}$

Energy dissipation by bottom friction is based on linear theory that is generalized into the following formula:

$$S_{ds,br}(\sigma,\theta) = -\frac{C_f}{g}\left[\frac{\sigma}{\sinh(kd)}\right]^2 E(\sigma,\theta)U_{rms} \tag{2.45}$$

where C_f is a bottom friction coefficient which depends on the hydrodynamic and sediment conditions. The root mean square of the orbital bottom velocity is represented by U_{rms} :

$$U_{rms}^2 = \int_0^{2\pi}\int_0^{\infty} \frac{\sigma^2}{g^2 \sinh^2(kd)} E(\sigma,\theta) d\sigma d\theta \tag{2.46}$$

Although, SWAN allows three types of bottom friction formulations, only the empirical model of JONSWAP (Hasselmann et al., 1973) will be discussed in this document. Each model uses the general formula as written above and the main differences are based on the derivation of the bottom friction coefficient C_f. The JONSWAP model sets $C_f = C_{JON} = 0.038 m^2 s^{-3}$ for swell conditions (Hasselmann et al., 1973), and sets $C_f = C_{JON} = 0.067 m^2 s^{-3}$ for wind-sea conditions (Bouws and Komen, 1983). This setting for bottom friction is default and used exclusively in all experimentation in this study, except for experimentation in open-sea locations where bottom friction is deactivated.

2.4.3.2.3.5 Depth-induced wave breaking, $S_{d,br}$

Depth-induced wave-breaking of individual waves is initiated when the wave height becomes greater than a certain fraction of the water depth. SWAN implements depth-induce wave breaking based on the random-bore model of Battjes and Janssen (1978), and Eldeberky and Battjes (1995) for random waves. Battjes and Janssen (1978) formulated the average energy dissipated in the breaking process; per unit area is represented by the following:

$$-D_{tot} = \frac{\alpha_{BJ}}{4} Q_b \left(\frac{\overline{\sigma}}{2\pi}\right) H_{\max}^2 , \tag{2.47}$$

$$\overline{\sigma} = \mathrm{E}_{tot}^{-1} \int_0^{2\pi}\int_0^{\infty} \sigma E(\sigma,\theta) d\sigma d\theta , \tag{2.48}$$

where $\alpha_{BJ} = 1$, $\overline{\sigma}$ is the mean frequency, and $H_{\max}$ is the maximum wave height that can exist at the given depth.

Q_b is the fraction of breaking waves induced by depth is determined by:

$$\frac{1-Q_b}{\ln Q_b} = -\left(\frac{H_{rms}}{H_{\max}}\right)^2, \tag{2.49}$$

$$Q_b = \begin{cases} 0 & \text{for } \beta \le 0.2 \\ Q_0 - \beta^2 \dfrac{Q_0 \exp\left(Q_0 - 1\right)/\beta^2}{\beta^2 \exp\left(Q_0 - 1\right)/\beta^2} & \text{for } 0.2<\beta<1 \\ 1 & \text{for } \beta \ge 0.2 \end{cases}, \tag{2.50}$$

$$\beta = \frac{H_{rms}}{H_{\max}} \tag{2.51}$$

In SWAN, dissipation from depth-induce breaking for a spectral component per unit time is calculated using formulation of Eldeberky and Battjes (1995), extended to include the spectral directions:

$$S_{ds,br}\left(\sigma,\theta\right) = D_{tot}\frac{E\left(\sigma,\theta\right)}{E_{tot}} \tag{2.52}$$

where D_{tot} represents power dissipated in the breaking process, $E(\sigma,\theta)$ represents the wave energy density at frequency σ in direction θ, and E_{tot} is the total wave energy of the spectrum.

2.5 Operations and output

This section describes methods developed to perform the individual procedures required to control and manage the wind-wave system. Every data processing computing system performs at least three functions: (1) data input, (2) data processing, (3) and data output. The main functions of the developed system are:

1) to download and prepare external meteorological data,
2) to process meteorological data to produce meso-scale wind data, and to process wind-wave model with 10m input data as well as bathymetric data,
3) to prepare calculated wind and wave output into both graphical charts and textual detailed tables.
4) to distribute graphical information over the world wide web network for display on both mobile appliances and personal computers.
5) to archive available data for future applications.

2.5.1 Processing control

The developed wind-wave system utilizes, “shell scripts,” to perform the processing routines required for every processing cycle. The shell on Linux operating systems is a command interpreter. It is a powerful programming language that is an easy-to-use tool for building applications. A shell program is called, “a script,” and allows all Linux commands, utilities and tools to be invoked. Shell scripts can perform administrative system task at scheduled times and relieves manual execution of tasks that need to be performed routinely. Although the shell language is not a full-blown tightly structured programming language, it allows enough programming control for most tasks that can be manually performed. The syntax of the shell language is similar to that of invoking and chaining together utilities at the command line. Shell scripting originates from the UNIX philosophy of breaking complex projects into simpler subtasks, of chaining together components and utilities.

All of the task needed to complete an entire cycle of data processing (input, process, output) can be done manually from the command line. Each task is broken down into manageable processes and a script was written to perform each task when required.

Both the hindcasting and forecasting functions of the system are controlled by scripts. The forecasting function requires the downloading of new data before processing can commence. The two major concerns in the real-time system, are: (1) timely acquisition of meteorological data, and (2) system recovery after system failure. Real-time processing of wind-wave forecast is performed four times daily, coinciding with the data availability of the GFS meteorological data from NCEP. The hindcasting function uses the same processing programs as the forecasting function but requires different wind input data and bathymetric data to be downloaded and formatted for each location.

2.5.2 Data acquisition

Almost all available data needed for the developed wind-wave system can now be accessed through the internet. The wind-wave model SWAN requires at least two types of data input, (1) meteorological data containing 10m wind, and (2) bathymetric data of the computational grid. Most meteorological datasets are provided real-time without cost for access. Most agencies throughout the world offer their data free of charge but at delayed access times. Availability of meteorological datasets is discussed in Section 2.3.2.

Most meteorological data files are considerably large and a fast high speed internet connection is required to receive meteorological data sets in a timely manner. There are three methods of obtaining data through the internet. The first method is through a Local Data Manager (LDM) or "push" technology. LDM developed by Unidata, is a collection of cooperating programs that select, capture, manage, and distribute arbitrary data products. The system is used in the Internet Data Distribution (IDD) project where a community of over 150 universities shares near real-time earth observations. Unidata IDD is designed so a university can request that certain data sets be delivered to computers at their site as soon as they are available from the observing system. The second method is scheduled download or "get" technology from ftp file servers of the data providing system. IDD is only available to educational organizations so most corporate organizations must download the required data through ftp. The third method is through satellite reception of NOAA data. A NOAAport receiver is required to capture the data from the NOAA satellites and reception of NOAAport satellite data is available only to North America and US territories.

2.5.3 Data dissemination

Atmospheric and oceanographic data are stored in many types of file formats throughout the world. The World Meteorological Organization was established to facilitate in worldwide exchange of meteorological and related information and the standards adopted have gained worldwide commitment. The problems facing established organizations are (1) existing data needs to be converted to WMO standards, (2) existing systems need to be modified to read/write new standards, and (3) different compression algorithms offer various tradeoffs.

The Grid Analysis and Display System (GrADS) from the Center for Ocean-Land-Atmosphere Studies (COLA), is used by the developed wind-wave analysis system to process all datasets into graphical or textual format. GrADS is an interactive desktop tool that is used for easy access, manipulation, and visualization of earth science data. The format of the data may be either binary, GRIB, NetCDF, or HDF-SDS (Scientific Data Sets).

The developed wind-wave system processes three types of data:

1) External meteorological data from weather agencies such as GFS, FNL, NARR, JMA-GSM, etc.
2) Internal meteorological data processed by the system using WRF.
3) Wind-wave data processed by the system using SWAN.

GFS data can be directly read by GrADS so no other conversion is necessary other than creating a control and index file using tools provided by GrADS.

WRF produces data files in a NetCDF format and need to be converted to GrADS format. The developed wind-wave system uses a conversion program provided by the WRF group to convert the WRF NetCDF formatted file to a GrADS formatted file . WRF uses an Arakawa-C grid where x and y data for wind is stored on a staggered grid. Due to interpolation, the grid points are doubled in the output file during conversion from NetCDF to GrADS.

SWAN output is in a textual data form where every data record represents a point on the computational grid. A C++ program was developed to convert the SWAN output into a GrADS or NetCDF binary formatted file.

GrADS allow easy access and manipulation of the data used and produced by the developed wind-wave analysis system. The following subsections briefly describe applications developed for data distribution.

2.5.3.1 WWW applications

The main goal of WWW applications is to deliver the most current available data to marine users, in a cost effective manner, so they can plan their activities accordingly. In the case of hindcasted data, the goal is to allow more time to be spent evaluating data instead of preparing data.

Two types of applications have been developed for access through personal computers connected to the internet:

1) Real-time marine weather information in the form of graphical animations and numerical data in tabular form.
2) Hindcasted numerical data for examination in two forms, “graphical animations” and “on demand” numerical data for selected points.

The real-time marine weather application allows users to view the most current meteorological and marine weather data available. The developed wind-wave system processes the following data and uploads to the WWW server:

1) GFS data is processed into a graphical animation that includes surface pressure and 10m wind direction and speed, in 3 hour increments. Forecasted animation goes out to 180 hours. The each graph displays data for the area between 120 to 180 degree longitude and 0 to 60 latitude.
2) WRF data processed into a graphical animation that includes surface pressure and 10m wind direction and speed, in 1 hour increments. Forecasted animation goes out to 72 hours. The each graph displays data for the area between 131 to 142 degree longitude and 33 to 38.5 latitude. In addition numerical data is extracted for AMEDAS locations within the calculation domain and displayed in graphical and tabular form. Wind forecasted by WRF is compared with AMEDAS reports to give a visual reference on forecasting success by the current WRF forecast.

3) SWAN data processed into a graphical animation that includes significant wave height, peak wave period, and 10m wind direction and speed, in 1 hour increments. Forecasted animation goes out to 72 hours. There are two domains processed. The first domain is a 27.5 km grid, for the area between 120 to 175 degree longitude and 5 to 55 latitude. The second domain is a 1.8 km grid, for the area between 136.4 to 142.3 degree longitude and 33 to 36.2 latitude.

The customizable hindcast application allows users to view any point of the calculation grid as a graphical map and numerical table. Detailed information includes wind speed, wind direction, significant wave height, and peak wave period. Each graph is produced individually by the WWW server so only upload of available data is required.

The data described above, distributed through WWW applications, do not represent the entire set of data distributed but only the data produced by the developed wind-wave analysis system.

2.5.3.2 Mobile applications

The Mobile application, delivers processed data through the mobile phone's internet feature. The developed wind-wave system processes the following data and uploads to the mobile server provider:

1) GFS data is processed into a graphical animation that includes surface pressure and 10m wind direction and speed, in 3 hour increments. Forecasted animation goes out to 180 hours.
2) WRF data processed into a graphical animation that includes surface pressure and 10m wind direction and speed, in 1 hour increments. Forecasted animation goes out to 72 hours.
3) SWAN data processed into a graphical animation that includes significant wave height, peak wave period, and 10m wind direction and speed, in 1 hour increments. Forecasted animation goes out to 72 hours.

2.5.3.3 Other entities

Data produced by the developed wind-wave analysis system is distributed to external organizations for their dissemination. Using Linux scripts, customized data processing routines have been developed meeting special request of various organizations. This type of distribution is mainly of the real-time forecasting functions of the developed wind-wave system.

Meteorological data sets such as the GFS, FNL, and WRF are very large and require an enormous amount of disk storage. Most of data processed and produced is archived for future use.

Chapter 3 Wave forecasting and verification

3.1 Introduction

Recent advances in wave modeling, computational power, meteorological data prediction, and data dissemination have allowed wave forecasting to be calculated and distributed in a cost effective manner. As the need for accurate and timely forecast increase, building a cost-effective wind-wave analysis system will allow more users to utilize the available information, leading to a reduction of maritime accidents.

This section takes the concepts detailed in Section 2 and discusses the wind-wave analysis system as employed for wave forecasting. Testing was performed to (1) verify the accuracy of forecast, (2) verify the timeliness of data processing and delivery, and (3) validate the reliability of the computer system.

3.2 Model description

As described in Section 2, the wind-wave analysis system consists of four core components: (1) system architecture, (2) meteorological wind input, (3) wind-wave model, (4) post processing. Employing the wind-wave system for forecasting requires the following:

1) Powerful enough to deliver accurate forecasted information in a timely manner;
2) Economical enough to offer data to users at a reasonable charge or even no charge; and
3) Deliverable to a large audience.

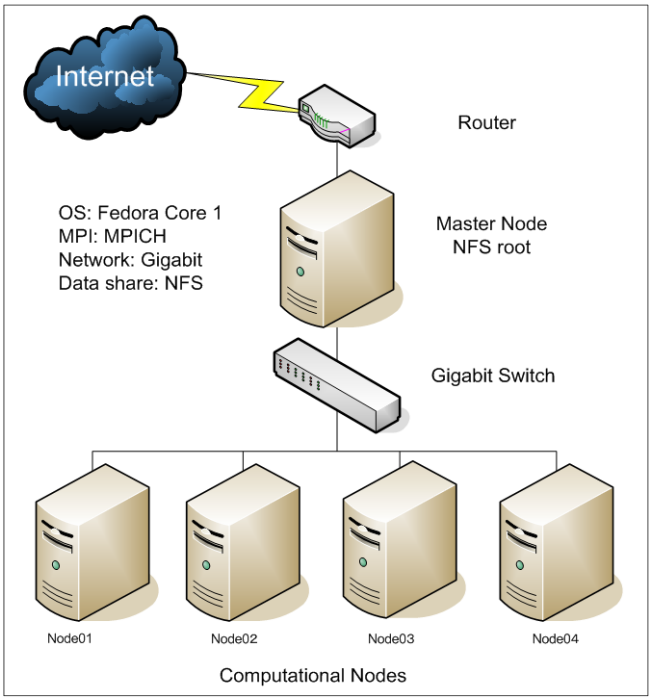

Fig. 3.1 System architecture

3.2.1 System architecture

The wind-wave analysis system as employed for forecasting uses a Class I Linux Beowulf style cluster computer system as described in section 2.2. Linux serves as the system's operating system with MPICH as the controller for parallel processing. Network communication is provided by Gigabit Ethernet interconnects and file sharing is provided by NFS. Figure 3.1 shows the system architecture as setup to perform wind-wave forecasting.

3.2.2 Wind forecast input

Ideally the JMA Grid Point Value Meso-scale Model (GPV-MSM) was preferred but obtaining the data cost effectively was a deterrent. National Centers for Environmental Prediction (NCEP) offers a real-time global NWP synoptic model called Global Forecasting System (GFS) through its NOAA Operational Model Archive Distributed System (NOMADS) servers on the internet.

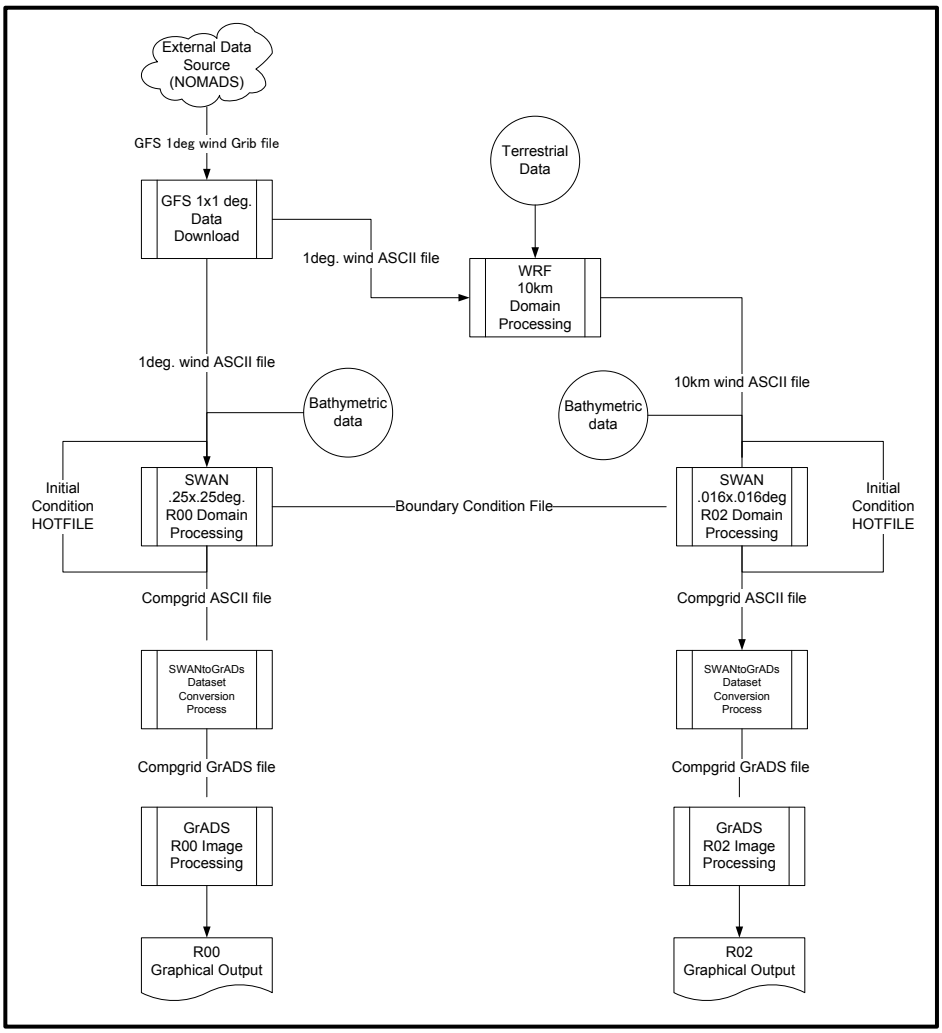

Fig. 3.2 Data flow diagram

GFS model data is updated four times a day and has a 1.0 degree grid resolution. The wind data at 10 m above the surface is extracted from GFS and used as input into the ocean wave model SWAN. For a discussion on GFS refer to Section 2.2.2.1. GFS model data is used as input into WRF to obtain a higher resolution wind field, and the resulting wind data is employed as input data for SWAN. For a discussion on WRF refer to Section 2.3.3.1. Figure 3.2 shows the flow of data during of the wind-wave analysis system employed for forecasting.

3.2.3 Wind-wave model

The wind-wave analysis system uses the wave model, SWAN, to calculate significant wave heights and mean wave periods generated by the winds in the computational area. To reduce the large CPU-demanding calculation time, SWAN coding allows parallel processing, which utilizes multiple independent processors to communicate through a Message Passing Interface (MPI) standard. Parallel processing in SWAN is performed by decomposing the calculation domain into load balanced partitions equal to the number of available processors. SWAN performs load balanced grid partitioning automatically, where the size of each partition equals the total number of wet points divided by the total number of partitions.

3.2.4 Post-processing

SWAN offers the ability to output data in text, or MATLAB formatted binary. Text can be in spectra format of swan or table form listing data for each data point for each time step on each line. The wind-wave analysis system converts SWAN text data point type output into a binary file readable by Grid Analysis and Display System (GrADS).

GrADS is an interactive desktop tool that can be used for easy access, manipulation, and visualization of earth science data. GrADS has been implemented worldwide on a variety of commonly used operating systems and is freely distributed over the Internet.

GrADS is used by the wind-wave analysis system to perform most data extract and graphical manipulation tasks. The system is coupled together by Linux scripts that are executed as “cron jobs.” GrADS output processing can be programmed and controlled by the system through batch processing allowing for automatic coordinated processing after each SWAN computation completes. Processed output data is then sent to a web server for data dissemination to a worldwide audience. In addition, data is compressed then sent to archive server for storage.

3.3 Verification

3.3.1 Wave forecasting system for the seas surrounding Japan

3.3.1.1 Introduction

Recreational marine users normally venture 10 km away from land at most but high cost of detailed weather prediction often fails to resolve the small-scale wind systems that play a crucial role in wind-wave generated near shore.

Ocean wave modeling has been extensively researched and used for maritime disaster prevention in the seas surrounding Japan. Available ocean wave models, mainly produced for commercial shipping and military activities, were not targeted for recreational marine users. Ocean wave models available for the general public were focused on deep-ocean events such as typhoons and tropical disturbances, and not presented for usual marine users to comprehend nor utilize in their ocean recreation activity.

This section presents the validation of the employed wind-wave analysis system as employed for wave forecasting for the seas surrounding Japan.

3.3.1.2 Model setup

The testing period of two months spanned a partial winter season, November and December 2004. Although the system is capable of calculating forecast four times a day, there was only one processing cycle a day for this test. Processing started at 9:00 JST every day and took approximately 5 hours to complete one processing cycle. One processing cycle as described in Figure 2 included the following: (1) GFS data download, (2) SWAN outer domain calculation, (3) WRF calculation for inner domain, (4) SWAN inner domain calculation, and (5) output processing. Each forecast calculation (SWAN outer, SWAN inner, & WRF 10m wind) produced a 72 hour forecast with a 1 hour temporal resolution

3.3.1.2.1 Computational domain

The wind-wave analysis system is configured to produce ocean forecast information for two domains:

1) Outer domain has a spatial resolution of 0.25 degrees covering the seas surrounding Japan (a longitudinal area from 120° E to 175° E and a latitudinal area from 5° N to 55° N), shown in Figure 3.3 (upper left);
2) Inner nested domain with a spatial resolution of 0.0165 degree resolution covering the Sagami-Bay Area (a longitudinal area from 136.4° E to 142.3° E and a latitudinal area from 33° N to 36.2° N), shown in Figure 3.3 (lower right). WRF calculated domain has a spatial resolution of 10 km with a 4.97 degree by 2.91 degree computational area.

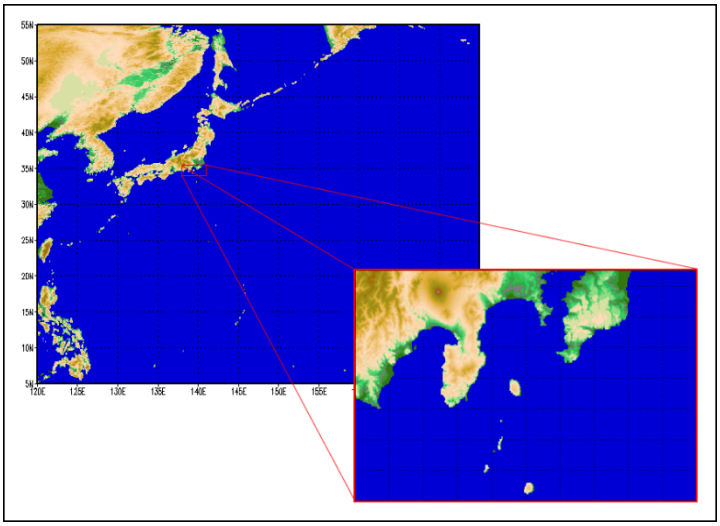

Fig. 3.3 Areas of computation: outer and nested domains

3.3.1.2.2 Numerical prediction models

The wave model for the system is SWAN which is configured to use the default wave growth formulation of Komen (1984) with triads, quadruplet, and white-capping turned on. The wind-wave analysis system as employed for forecasting produces two domains but only the outer domain is evaluated in this validation. WRF, as described in Section 2, is a numerical weather model capable of producing meso-scale forecasts. WRF and the inner mesh domain are tested in the next section for three seasons.

3.3.1.2.3 Input data

SWAN requires at a minimum two types of input data: (1) 10m wind data, and (2) bathymetric data of the calculation area.

The outer domain used GFS 10 m wind data with a 1.0 degree spatial resolution from NCEP (The National Center for Environmental Prediction). GFS 1.0 degree has a temporal resolution of 3 hours. GFS is discussed in Section 2.3.2.1, GFS & FNL. The model was setup to use 10 minute horizontal resolution, DBDB-V bathymetric data from Naval Oceanographic Office.

The inner domain used GFS 10 m wind data with a 10 km spatial resolution. WRF 10 km was set to produce forecast with a 1 hour temporal resolution. WRF is a meso-scale weather model that uses terrestrial and GFS synoptic forecast data and produces highly detailed meso-scale wind forecast down to a 1 km spatial resolution. WRF is discussed in Section 2.3.3.1, WRF. The model was setup to use J-EGG500 bathymetric data from the Japan Oceanographic Data Center. J-EGG500 bathymetric data has a 500 m horizontal resolution.

Figure 3.4 displays the wind forecast of 10 km grid resolution (left hand side) and forecasted wave height and direction (right hand side). Figure 3.5 shows an example of the forecasting of wave heights and directions for the outer and nested domains.

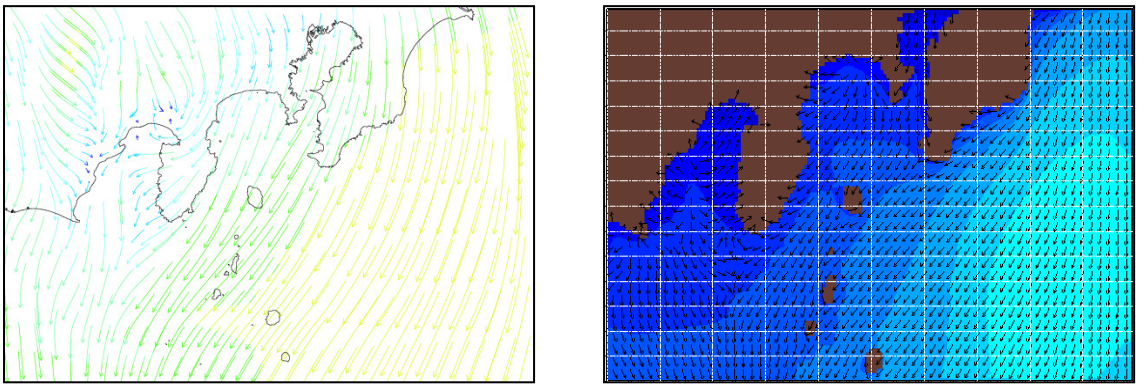

Fig. 3.4 WRF 10 km wind forecast (left) and resulting wave height and direction (right) for nested domain at 10/23/2004 00:00 GMT

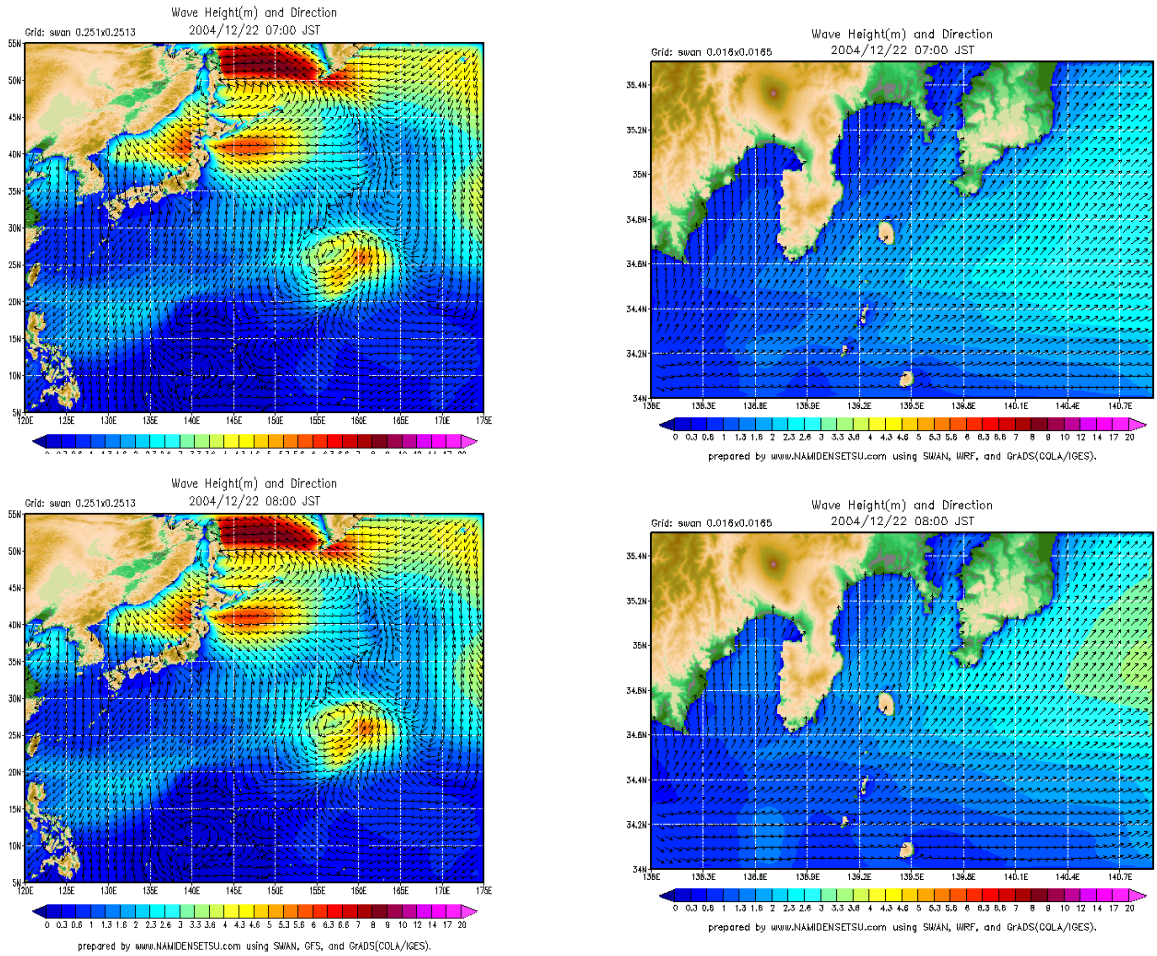

Fig. 3.5 Forecasted wave heights and directions for outer and nested domains

3.3.1.3 Observational data

System verification and validation were performed to ensure the system performed reliably and forecasted accurately. In addition, testing using real-time data was performed to find suitable correlation factors. Seven points were selected, from NOWPHAS (Nationwide Ocean Wave Information network for Ports and HArbourS, Sugahara et al., 1999), to compare the forecasted wave heights and periods with the observed ones. The selected points are shown in Figure 3.6. These points are situated in locations open to the sea (not in Bays or Inlets).

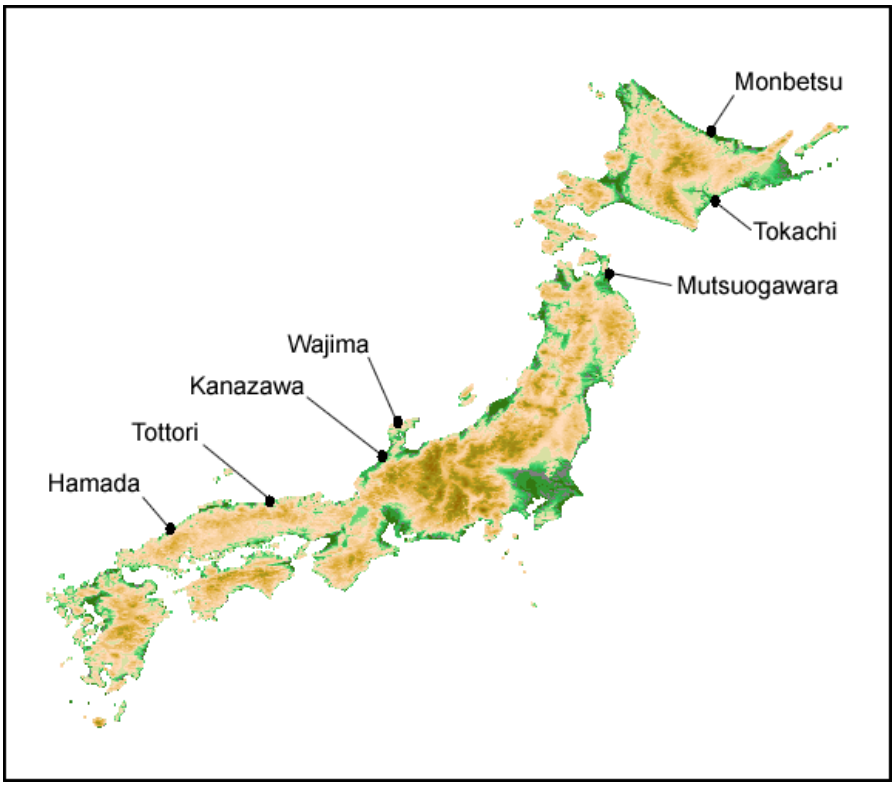

Fig. 3.6 Test locations of NOWPHAS wave gauges

Testing was performed over a two months period from November 1st to December 31st 2004 (partial winter season in Japan). The testing focused on a large domain which encompasses the deep-sea regions around Japan. The computational grid of domain was set to 0.25 degrees under GFS's 10 m wind input with a resolution of 1.0 degree. Processing was executed (started) at 09:00 JST daily. The system was monitored daily and output was saved for analysis. The saved data included forecasted wave heights and wave periods at 5 hr, 11 hr, 23 hr, 35 hr, 47 hr and 59 hr ahead of the processing start time (09:00 JST). System modification was frozen and limited to, “emergency only maintenance.”

3.3.1.4 System errors during testing

During the course of two months no major problems occurred but the following areas of concern in system design were uncovered:

1) Due to data unavailability, the system failed to process on two occasions. GFS data was unavailable for download from the NOMADS server, due to heavy server load. Systems contingency accounts for data unavailability by trying to download data at 30 minute intervals until successful. If after six tries this process fails, the entire system will terminate processing and wait until the next processing period. On the two occasions of system failure, the system tried to download data for three hours then halted, as programmed. The system is dependent on real-time GFS wind data and cannot function without this vital input. Therefore, a chain of data sources that will allow GFS data download 100% of the time is a critical requirement.
2) During system failure, manual intervention was required to continue processing. Restoration of initial condition files (hotfiles) was required to restart the system job and reprocess the ocean models for the missing time period. An automated recovery method of restoring hotfiles after system failure is needed.

To prevent data unavailability, another source of data was found and employed to push GFS data to the system four times a day. This data provider obtains GFS data through a NOAAPort satellite feed then sends the data through ftp to the system. The system first tries to download the data from the NOMADS server. If this fails, it checks if the “PUSHED” data has been received, if none are available the system waits for 30 minutes then repeats the data acquisition cycle.

To prevent system halting on system failure a “fail-safe” system needs to be implemented. The “fail-safe” system needs the following:

1) A head node on “ready-wait” on head node failure.
2) A backup compute node on compute node failure.
3) A data storage server on “ready-wait” on data storage server failure.
4) Daily backup of head node, compute node, and data storage server main hard disk. Incremental storage of working disk attached to data storage server.

3.3.1.5 Comparison and evaluation

Data validation consisted of comparing model output with real-time wave gauge reports at seven points surrounding Japan.

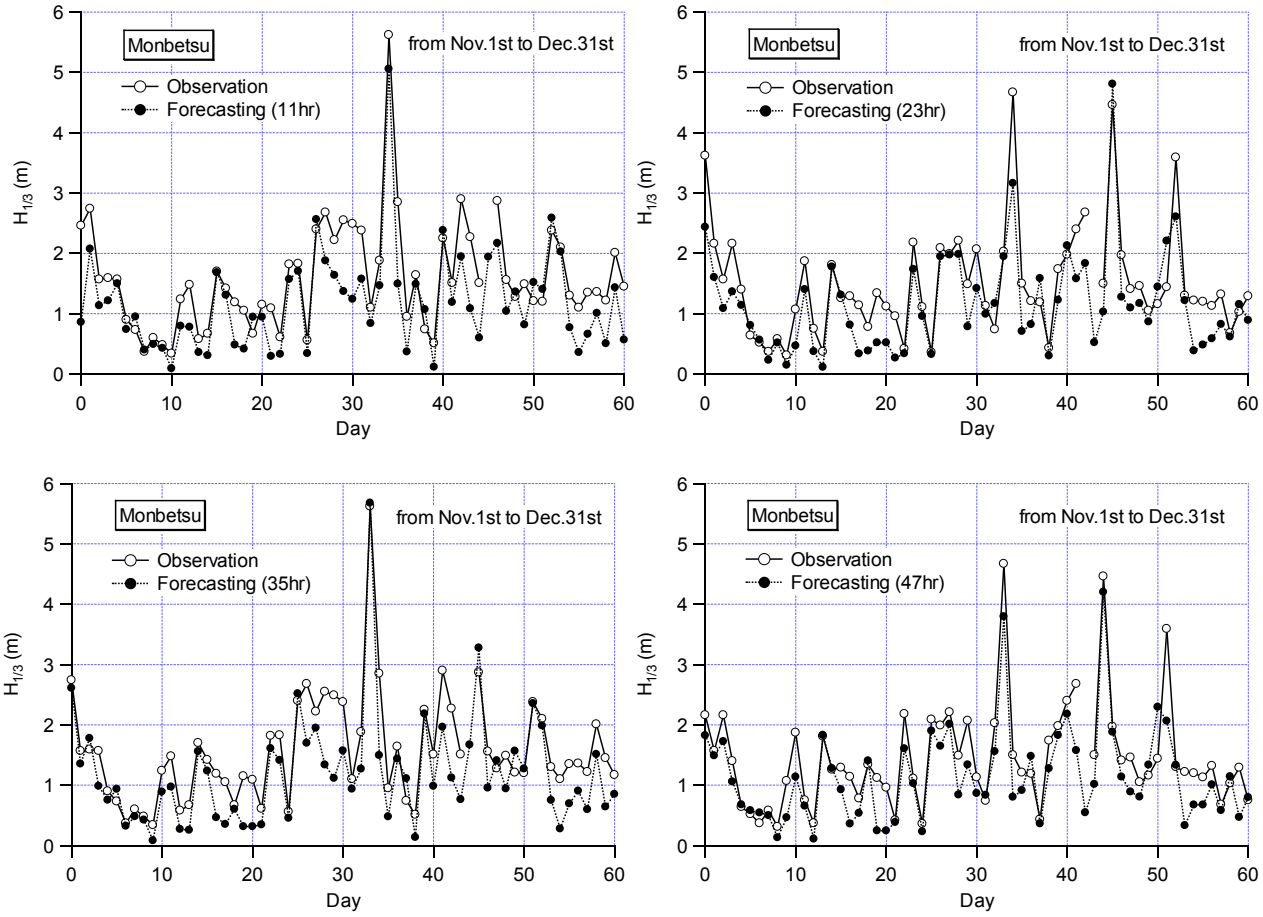

Fig. 3.7 Observed and forecasted wave heights at Monbetsu of NOWPHAS system

Figure 3.7 shows an example of the time series of observed wave heights compared with the forecasted significant wave heights at 11 hr, 23 hr, 35 hr and 47 hr after the start of forecasting calculation. This figure shows good correspondence of changes in wave heights, but forecasted wave heights tended to be under-reported.

Figure 3.8 shows comparisons of wave heights in a different form. Figure 3.9 denotes a summary of correlation coefficients between observed and forecasted wave heights. It can be seen that correlation is good even at the 59th hour forecast. If suitable correlation factors were used, the forecasted wave heights become good estimates.

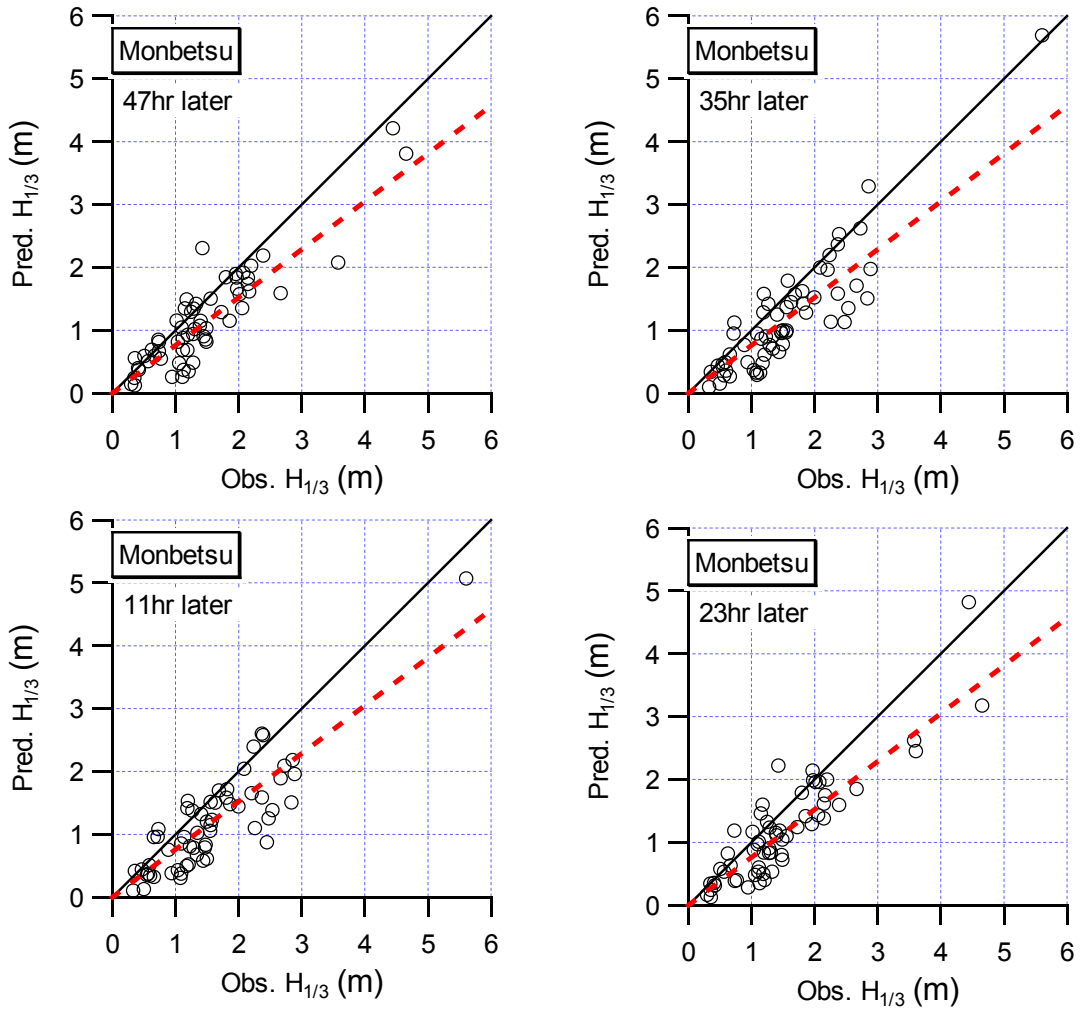

Fig. 3.8 Comparison of wave heights with observations

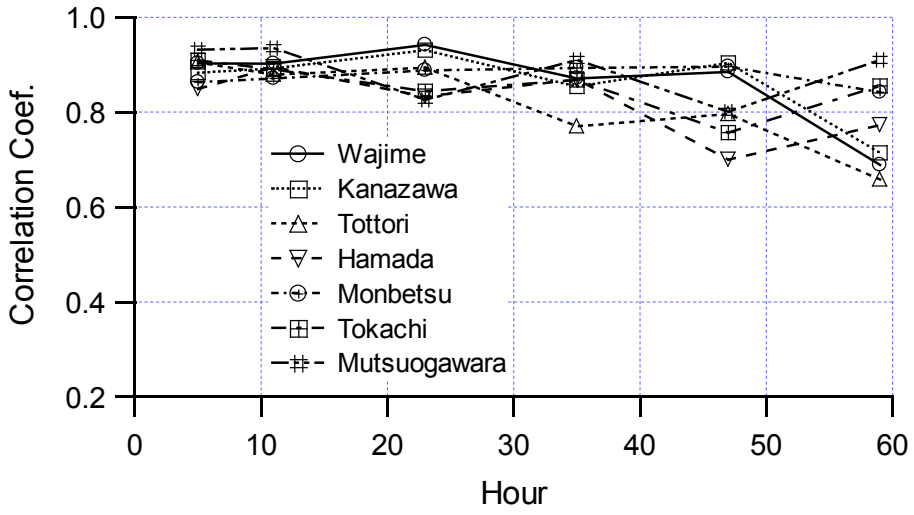

Fig. 3.9 Correlation coefficients between observed and forecasted wave heights

The present analysis indicates that the GFS forecast possesses characteristics of under-predicting 10 m wind strength, causing wave heights to be under-predicted and that different parameter settings for day and night processing exists. The rough resolution of 1.0 degree GFS wind data cannot represent the wind field near coasts, which is a cause of the differences between observed and forecasted data.

3.3.1.6 Summary

In summary, causes of wave height forecast error are believed to be from the following:

1) Wave gauge and forecasted point location were not exact;
2) Synoptic GFS model resolution and computational grid size of the SWAN domain was too large for accurate prediction of close to shore locations;
3) Course resolution of GFS synoptic data fail to resolve the small-scale wind systems that play a crucial role in the generation of near shore wave systems;
4) 10 min bathymetric data resolution too large. Higher resolution data is needed to increase forecast accuracy;
5) GFS and SWAN models both contain computational errors.

A wave prediction system suitable for casual marine recreational users has been developed by combining the near shore wave prediction model of SWAN with the synoptic model of GFS, and the high resolution meso-scale model of WRF. Tests have shown that the system is reliable in predicting changes of wave height but wave heights are slightly under-predicted and that an error ratio can be applied to forecasted output to better approximate wave heights.

3.3.2 Three season study of GFS-WRF-SWAN forecast system

3.3.2.1 Introduction

Section 3.3.1 detailed the performance of SWAN utilizing GFS input during a winter season by comparing forecasted values with observational values from selected NOWPHAS buoy points. This study continues by examining the performance of the forecasting system during three seasons: spring, fall (typhoon), and winter.

First, the accuracy of predicting a typhoon's course was evaluated by comparing JMA and GFS forecasted tracks with official "best track" data as reported by JMA. Second, the accuracy of GFS-WRF wind data was evaluated against AMEDAS wind observations at four locations in the Mutsu Bay area. Third, accuracy of both the GFS-SWAN and GFS-WRF-SWAN wave predication were evaluated for three seasons. The boundary input was provided by an outer SWAN computational grid using GFS with a 1.0 degree spatial resolution. Finally, the influence of wave growth parameters were examined, by repeating a test with the same wind input and changing the wave growth formulation and frequency ranges.

3.3.2.2 GFS and WRF evaluation

3.3.2.2.1 Typhoon track forecast evaluation

The forecasted routes by GFS were compared with the actual routes reported by the Japan Meteorological Agency (JMA) for Typhoons 11, 14, 17 that occurred in 2005. Figure 3.10 is a comparison example showing the actual route of Typhoon 0511 and forecasted routes of both GFS and JMA. The actual route is indicated by ○, and two forecasted routes as reported by JMA are indicated by ◇, and □. GFS forecasted routes for two different times are indicated by △, and ▽.

The agreement is good at an initial stage, because the forecast of JMA starts from an actual typhoon position. Conversely, the GFS typhoon route starting at 0300 on the 24th is not in good agreement with the initial starting point of the actual typhoon position. Figure 3.10, shows that a correlation exists between the GFS forecast and actual route. Adjusting the starting point of the GFS forecast brings the forecasted and actual routes in agreement, showing the route predictability of GFS.

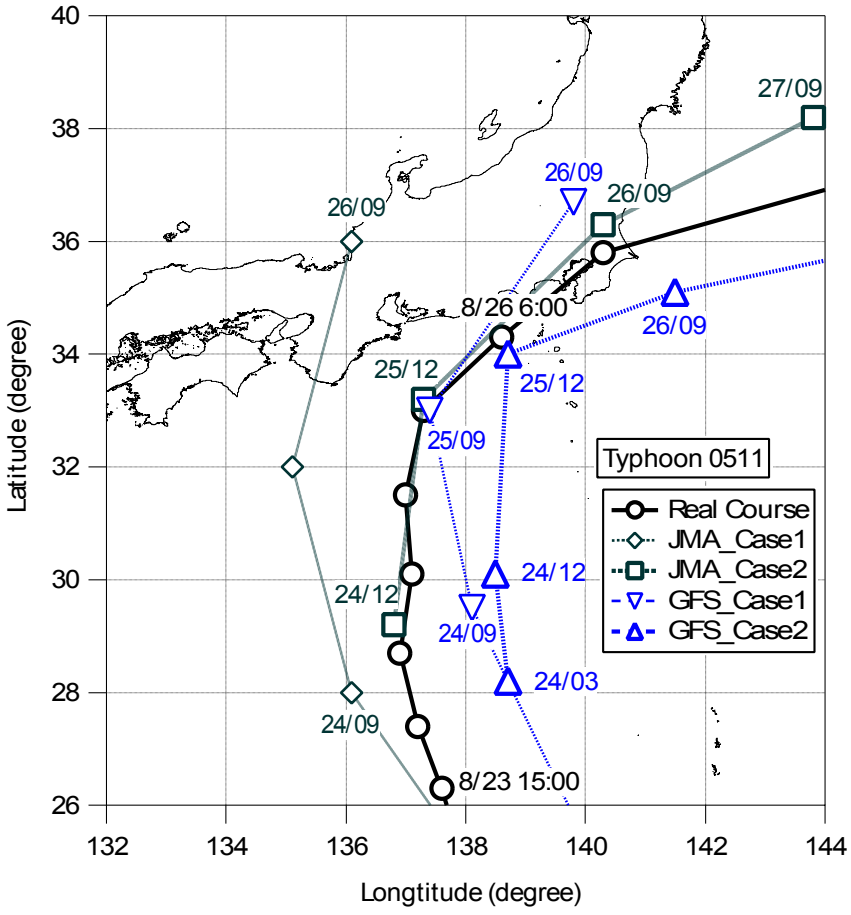

Fig. 3.10 Typhoon 0511 actual and forecasted courses of both GFS and JMA

3.3.2.2.2 Wind speed examination

Wind prediction of a 10 km spatial resolution was compared with wind data of the Automated Meteorological Data Acquisition system (AMEDAS) for Mutsu bay. The calculation area covers a longitudinal area from 140° E to 175° E and a latitudinal area from 40.7° N to 41.8° N.

The results of two points: Aomori (140.77°E, 40.82°N), Mutsu (141.21°E, 41.28°N) are shown in Figures 3.11 to 3.14 for the periods: (1) Spring from May 16th through 23rd, 2005; (2) Summer from July 23rd through 30th, 2005; (3) Autumn from November 23rd through 30th, 2004; and (4) Winter from January 13th through 20th, 2005

A 10 km mesh was calculated once daily with WRF using GFS meteorological data as input. GFS data was downloaded daily from the NCEP server. In figures 2 through 5, WRF calculated wind speed at Mutsu and Aomori is represented by ● and JMA AMEDAS reported wind speed is represented by ○.

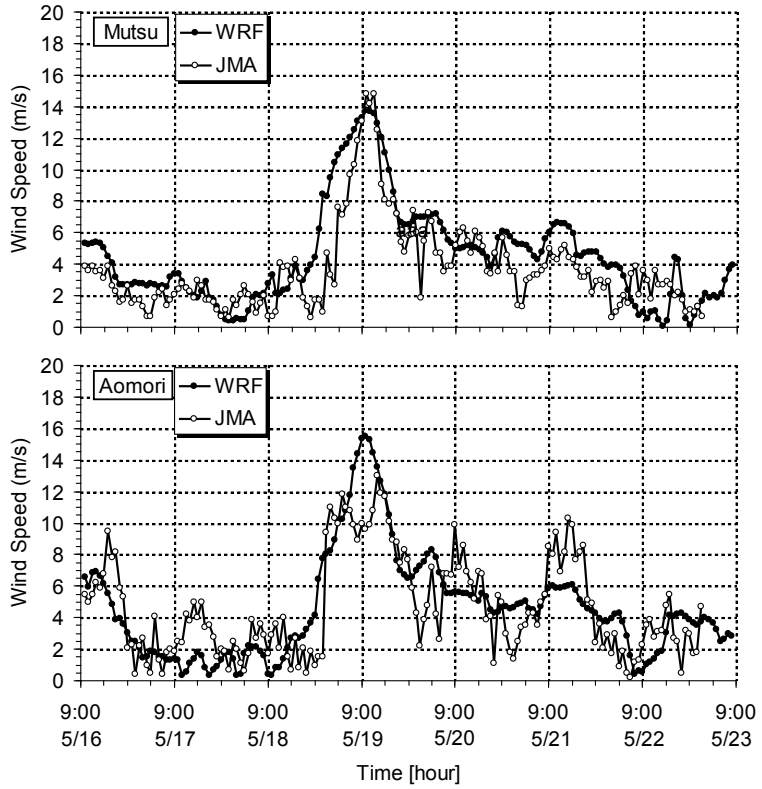

Fig. 3.11 GFS-WRF comparison for Mutsu and Aomori during Spring

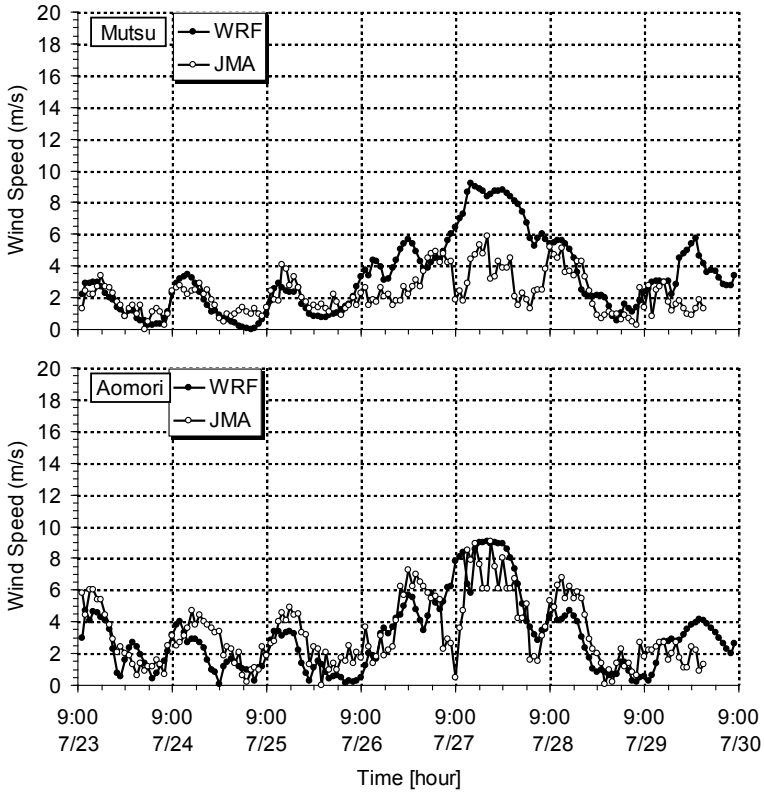

Fig. 3.12 GFS-WRF comparison for Mutsu and Aomori during summer

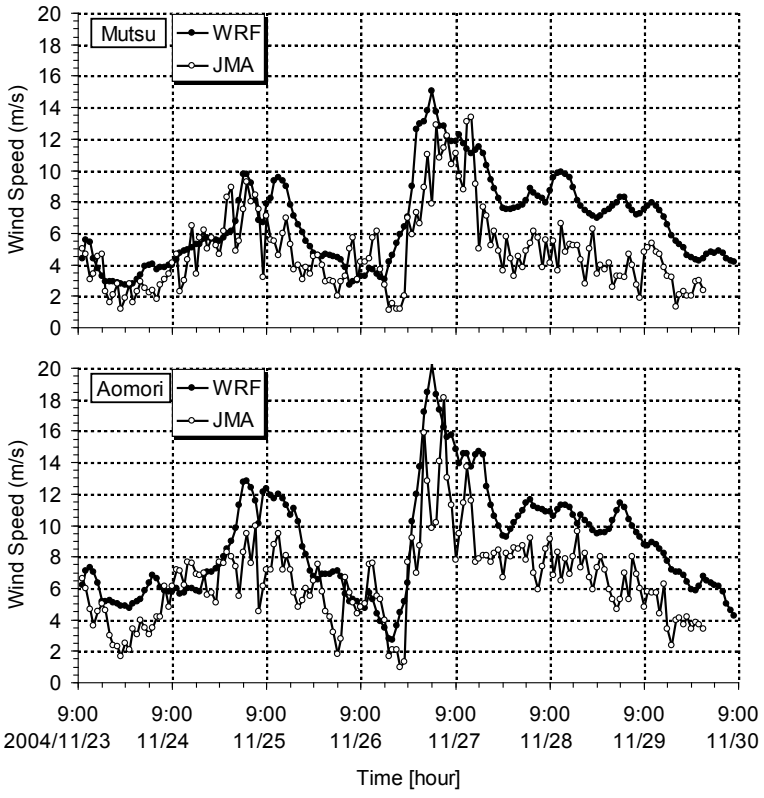

Fig. 3.13 GFS-WRF comparison for Mutsu and Aomori during fall

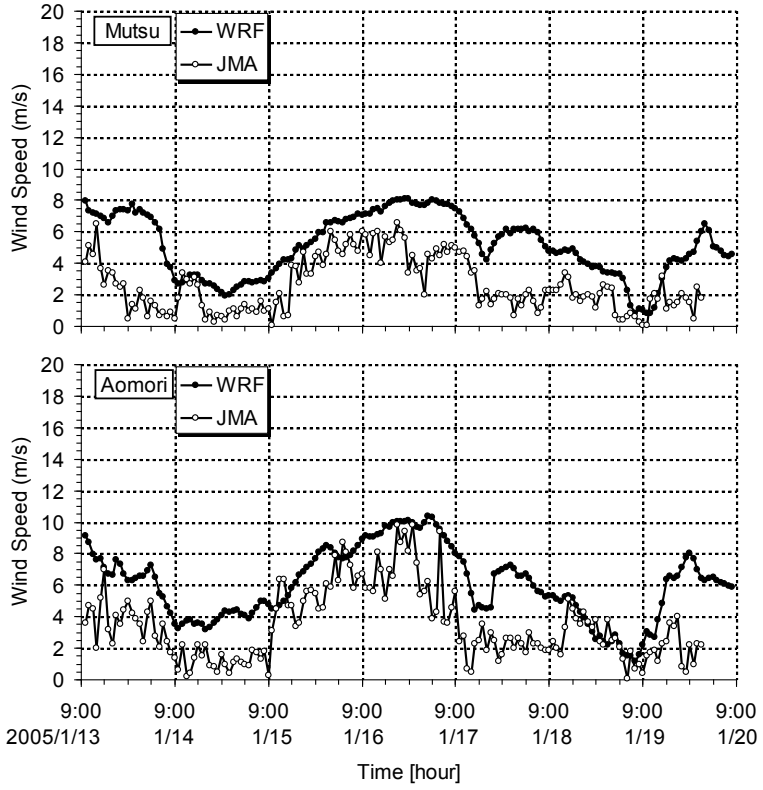

Fig. 3.14 GFS-WRF comparison for Mutsu and Aomori during winter

The AMEDAS stations at Aomori and Mutsu are located in graphical locations that are generally similar with the most noticeable difference being that the ocean is located to the North of the Aomori station and South of the Mutsu station. The prediction values at Aomori had a tendency to be greater than observations values. Three key factors influence the accuracy of observations: (1) surrounding geographical land features, (2) surrounding buildings, and (3) height of the wind observation unit. For Aomori and Mutsu, the prediction and observation values corresponded well for all seasons, with a general tendency of predicted wind to be over reported. Over-reporting is more common during times of high wind.

3.3.2.3 Comparisons and evaluations

3.3.2.3.1 GFS-SWAN model testing

The forecasted significant wave height using SWAN with GFS meteorological 10m input, was compared to observations at four NOWPHAS points. These points are situated in locations open to the sea (not in Bays or Inlets). The four selected points for comparison were: (1) Wajima (136°54′ 08″E, 37°25′51″N); (2) Kanazawa (136°34′03″E, 36° 36′50″N); (3) Tottori (134°09 ′41″E,35°33′16″N); and (4) Monbetsu (143°36′25″E, 44°19′04″N).

The testing period included three seasons in Japan: (1) 61 days in Winter from November 1st through December 31st, 2004; (2) 61 days in Spring from March 1st through April 30th, 2005; and (3) 62 days in Fall from August 20th through October 20th, 2005.

The computational domain had spatial resolution of 0.25 degrees, covering the seas surrounding Japan (a longitudinal area from 120° E to 175° E and a latitudinal area from 5° N to 55° N), shown in Figure 3.3 (upper left). GFS 10 m wind data with a spatial resolution of 1.0 degrees and temporal resolution of three hours was used as input. DBDB-V bathymetric data from Naval Oceanographic Office, with a 10 min spatial resolution was used.
GFS data was downloaded once daily at nine o'clock and a 72 hour forecast was calculated using the SWAN wind-wave model. The SWAN model was setup to use the default wave growth formulation of Komen with triads, quadruple wave-wave interaction, and wave-breaking set to on.

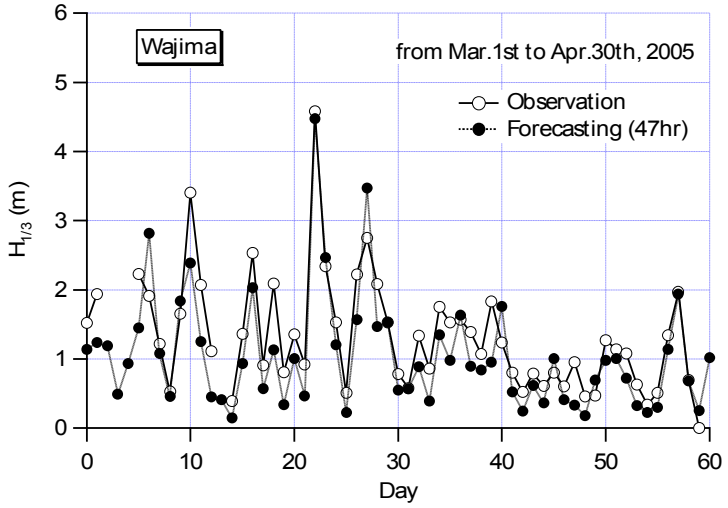

Fig. 3.15 GFS-SWAN significant wave height comparison for spring

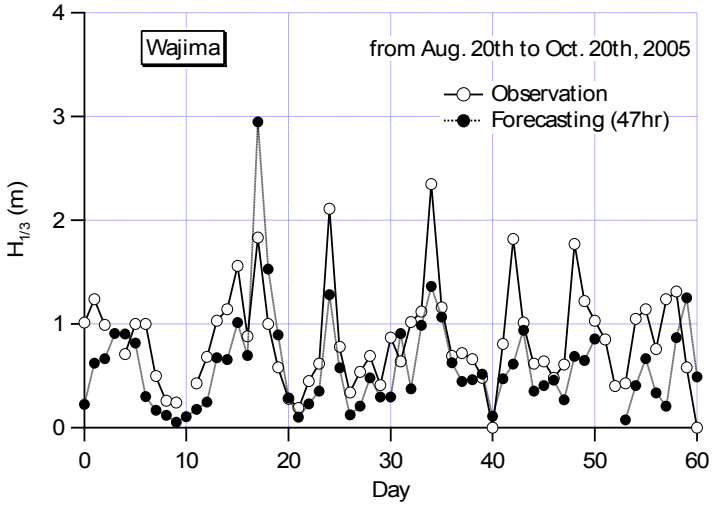

Fig. 3.16 GFS-SWAN significant wave height comparison for fall

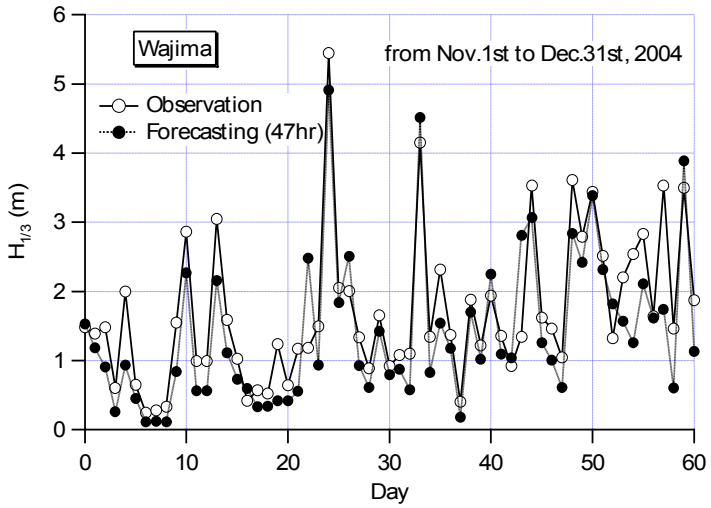

Fig. 3.17 GFS-SWAN significant wave height comparison for winter

Figures 3.15 to 3.17, are comparison of significant wave height prediction vs. observation for 60 days at the Wajima NOWPHAS buoy for three seasons. The horizontal axis represents the day of testing and the vertical axis represents significant wave height of NOWPHAS observations and GFS-SWAN forecast at the 47th hour of calculation.

Time series comparison of observed and predicted wave height corresponded well for all seasons. The forecasted significant wave height tended to be under-reported as compared to observations from the NOWPHAS buoy.

Figures 3.18 to 3.20, plot the correlation coefficient of the forecasted value for the time series of 60 hours with the NOWPHAS observational values, for three seasons. Each figure includes calculations for four NOWPHAS buoy locations: Kanazawa, Tottori, Monbetsu, and Wajima. The horizontal axis represents forecasted hour and the vertical axis represents the calculated correlation coefficient of the NOWPHAS buoy and forecast values.

The correlation coefficient of the four points in the winter testing, Figure 3.20, is high throughout the 60 hour forecast and shows good correlation. Forecast during the spring, Figure 3.18, shows high correlation coefficient values for the four points throughout the time series if Monbetsu is excluded after 50 hours. During Fall, Figure 3.19, the correlation coefficient starts good then decreases as along the forecast time series and Kanazawa showing low correlation throughout the time series. Fall is a period where there Typhoon activity is high.

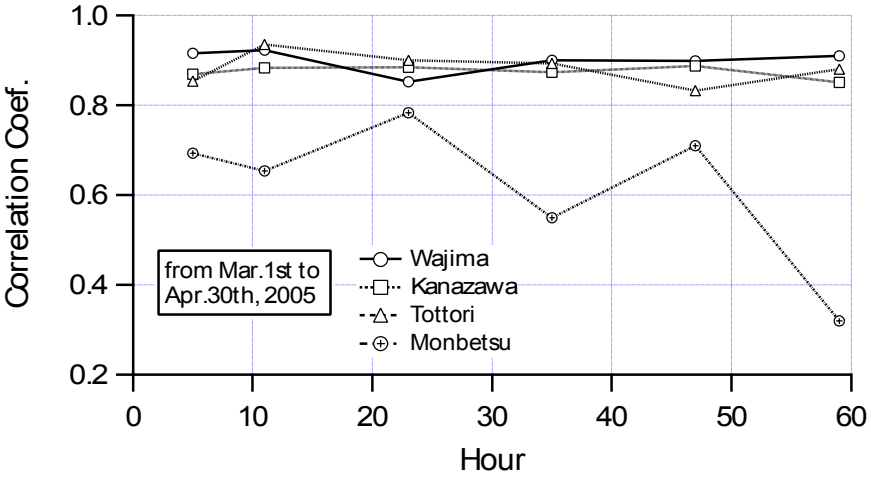

Fig. 3.18 GFS-SWAN correlation coefficient for spring

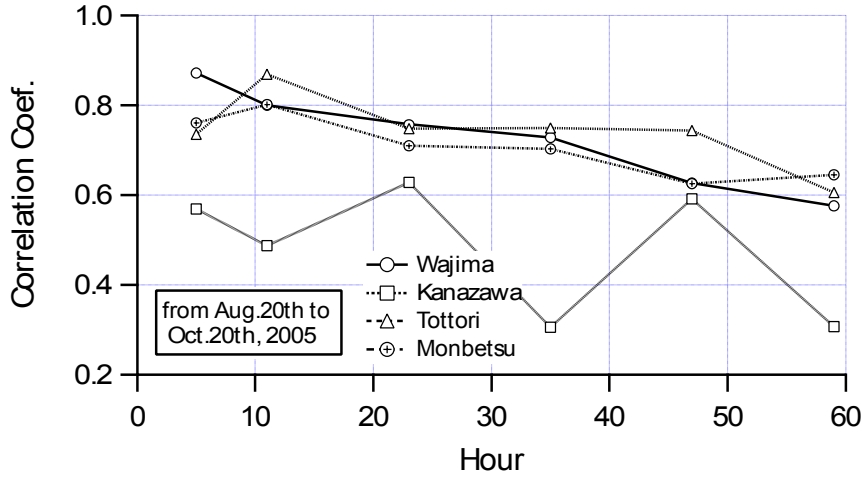

Fig. 3.19 GFS-SWAN correlation coefficient for fall

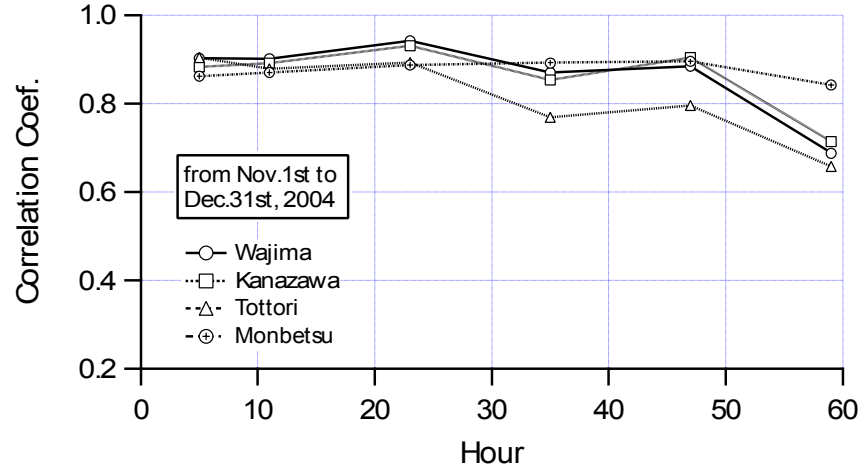

Fig. 3.20 GFS-SWAN correlation coefficient for winter

Generally the correlation coefficient is consistent and high during Spring and Winter but, a proportional decreases as the forecast time increase is seen, during Fall. Monbetsu showed overall lower correlation compared to the other points in Spring and Kanazawa showed marked low coefficient in Fall. The forecast during each season showed general consistency with the exception of the outlying points. Additional study needs to be performed to determine the causes of discrepancies at the outlying points.

3.3.2.3.2 GFS-WRF-SWAN model testing

GFS is a synoptic numerical weather model and has a spatial resolution of 1.0 degrees that is suitable for wave modeling on synoptic scaled computational grids. Small wind systems on the meso-scale and with geographical features greatly influence the wind flow on meso-scale computational grids. Since GFS does not accurately show small pressure systems, meso-scaled wind in input is required.

Weather Research and Forecasting (WRF) is a meso-scale numerical weather prediction model that uses synoptic forecast, such as GFS, to calculate meso-scaled forecast. The GFS forecast is downloaded then used as input into WRF to calculate a meso-scaled forecast. WRF calculated domain has a spatial resolution of 5 km with a 4.97 degree by 2.91 degree computational area. The WRF 10 m wind forecast is used as input into the inner wind-wave model domain, covering the Sagami-Bay Area (a longitudinal area from 136.4° E to 142.3° E and a latitudinal area from 33° N to 36.2° N) with a spatial resolution of 0.0165 degrees. Figure 3.3 shows the outer (GFS-SWAN) and inner (GFS-WRF-SWAN) domains. The boundary input for the inner computational grid is provided by the GFS-SWAN calculation run described in the previous section, section 3.3.2.3.1 GFS-SWAN model testing. Refer to Section 3.2 for details of the processing/data flow. Bathymetry consisted of a spatial resolution of 5 km. This series of processing will be henceforth referred to as the GFS-WRF-SWAN model in this section.

The GFS-WRF-SWAN model tested for two periods: (1) March 1st through April 30th 2005, 61 days, and (2) August 20th through October 20th, 62 days. The forecasted value was compared with the observation data from the NOWPHAS buoy at Shimizu (138°30′22″E, 35°01′16″N) and Shimoda (138°57′11″E, 34°38′48″N).

The correlation of the forecast and observation values at the NOWPHAS buoy points Shimoda and Shimizu, for both GFS-SWAN and GFS-WRF-SWAN model testing, are shown in Figure 3.21 and Figure 3.22 respectively. Figure 3.21, shows data from the Shimoda point during the March through April test period. In this figure, the forecast value of GFS-SWAN (○) excludes the case where the forecasted wave height compared with the observation value is extremely large. Figure 3.22, shows data from the Shimizu point during the August through October test period.

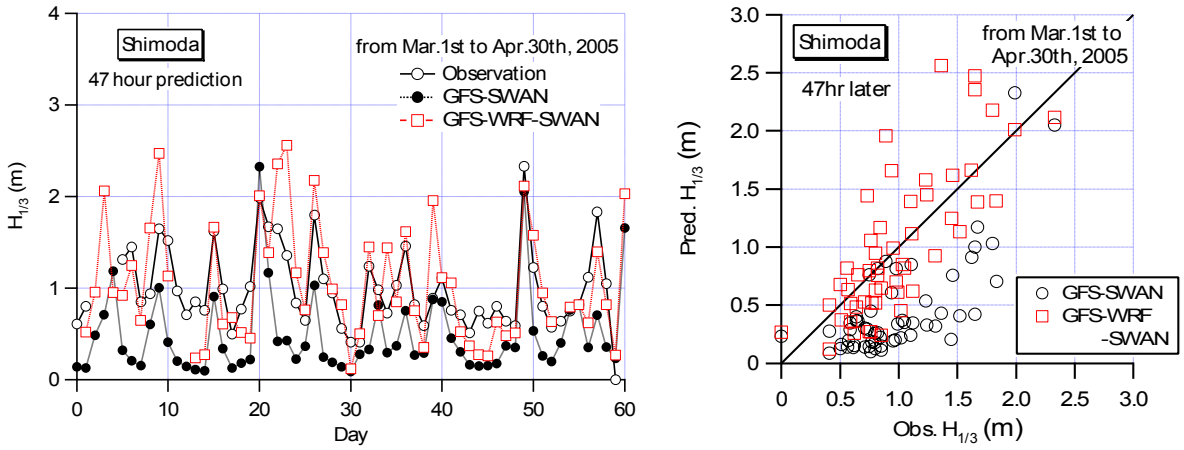

Fig. 3.21 Predicted and observed wave height comparison at Shimoda

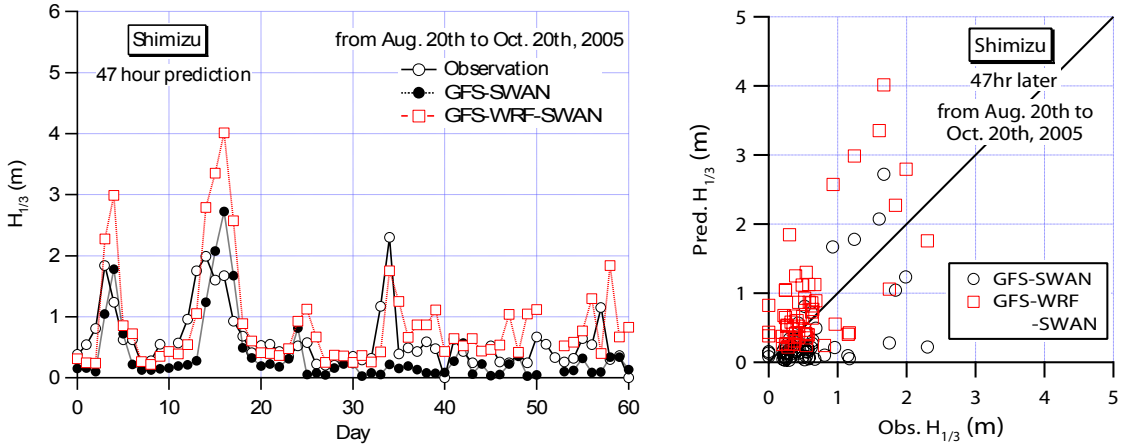

Fig. 3.22 Predicted and observed wave height comparison at Shimizu

The March through April testing is characterized by periods of higher close to shore wind systems that generated wind-waves in the computational domain. August through October testing is characterized by lower closer to shore wind systems but higher occurrence of winds of typhoon speeds. As a Significant wave height during the March through April test period was on the average higher than the August through October test period. The significant wave height during the August through October test period was generally under one meter with larger waves generated by typhoons.

At Shimoda, the GFS-WRF-SWAN (□) showed improved forecast and observation correspondence over the GFS-SWAN throughout the test period. GFS-SWAN shows a tendency of under predicting wave height. Improvement can be attributed to WRF being able to resolve the smaller wind systems that were predominant during this test period. GFS-SWAN with a spatial resolution of 25 km is not able to account for both meso-scaled weather systems as well as changes in wind patterns due to geographical features influencing the

calculation domain. Testing shows that a spatial resolution of at least five km as shown in the GFS-WRF-SWAN model, is necessary to resolve meso-scaled wind systems and surrounding topography.

A similar tendency is seen at Shimizu during the August through October test period. GFS-SWAN wave height forecast compared against NOWPHAS observation data showed that forecast are generally under-predicted. GFS-WRF-SWAN shows overall improvement in wave height forecast correspondence with observed values. This test showed the importance of meso-scaled wind input when forecasting wave heights during periods of low wind. The detailed 5 km spatial resolution of the WRF computational grid was able to show wind systems that GFS was not able to detect.

3.3.2.3.3 Influence of setup parameters on forecast results

In the above-mentioned forecast calculation testing, the default setting as provided by the SWAN model has been used. SWAN defaults to third generation mode with formulation by Komen et al. (1984). Moreover, wave calculations during the three season testing used a frequency range of 0.01 Hz to 1.0 Hz. This section examines the effects to wave calculations when SWAN parameters are changed.

The GFS-SWAN model was tested using three energy transfer models: Komen et al. (1984), Janssen (1991), and a modified Janssen model proposed by Lalbeharry et al. (2004). SWAN offers two types of energy transfer models to be selected: formulations by Komen et al. (1984) and Janssen (1991), where Komen eis the default setting. For a discussion of the two energy transfer models refer to Section 2.4.3.2.1.2, Modified wind growth formulation in SWAN. Lalbeharry et al. (2004) describe modifications to SWAN's implementation of Janssen's formulation (1991) where (1) the shift growth parameter z_α = 0.011 in the exponential wind growth source term was added, and (2) the wave growth limiter was modified to be similar to WAM Cycle-4. For a discussion on modifications by Lalbeharry et al. (2004) to the SWAN implementation of Janssen (1991) formulations refer to section 2.3.3.2.1.2 Modified wind growth formulation in SWAN.

Each formulation was tested using two frequency ranges were tested using each energy transfer model: 0.01 to 1.0 Hz and 0.01 to 0.5 Hz. The three season test performed using the GFS-SWAN model and GFS-WRF-SWAN model used 0.01 to 1.0 Hz as a default setting.

Figure 3.23 and 3.24 shows the wave height and wave period results respectively from the six different calculations using different parameters. It is shown that the wave height forecast performance of each formulation were relatively same for both frequency ranges. Lalbeharry et al. (2004) performing better than the default formulation of Komen et al. (1984) and Janssen (1991) formulation showing large under reporting of wave heights.

Different results were observed for wave period forecast using the two ranges:

1) Komen et al. (1984) although still under reported, period forecast showed improvement using the frequency range 0.01 to 0.5 Hz over the range 0.01 to 1.0 Hz;
2) Janssen (1991) shows slightly better period forecast than Komen et al.(1984) and both frequency ranges performed similarly;
3) Lalbeharry et al. (2004) showed better overall performance in period forecast than Komen et al. (1984) using the frequency range of 0.01 and 0.5 Hz but similar performance with Komen et al. (1984) using the frequency range of 0.01 and 1.0 Hz.

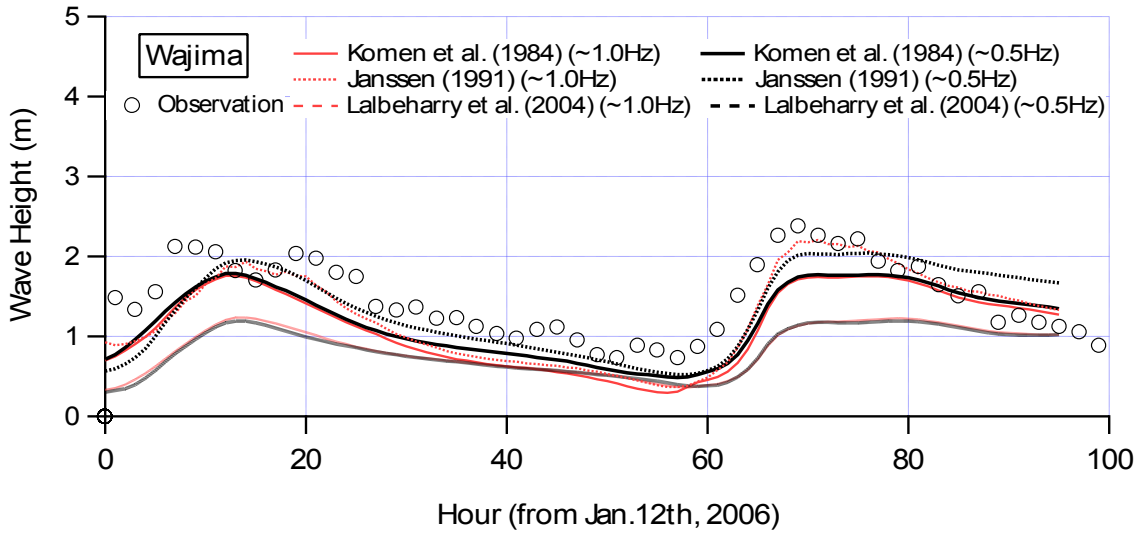

Fig. 3.23 Wave height calculation results using six different parameters

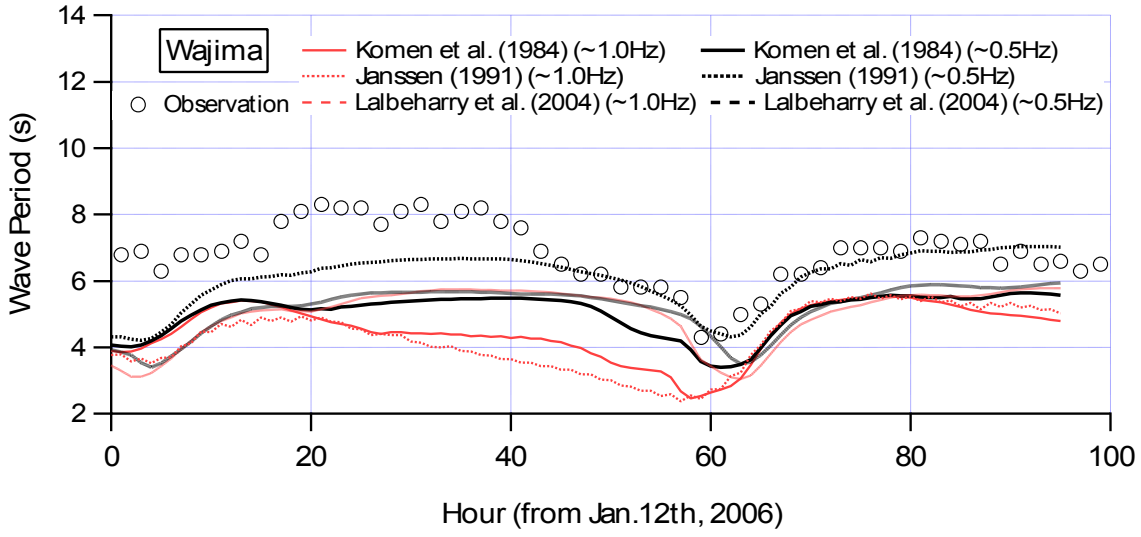

Fig. 3.24 Wave period calculation results using six different parameters

.

3.3.2.4 Summary

This study examined the individual components of the wind-wave analysis system when employed for wave forecasting. Wind forecast accuracy was examined first by examining the ability of GFS to predict typhoon routes. The study then examined the accuracy GFS-WRF wind forecast in the Mutsu Bay area. Wave forecast accuracy was examined by verifying the performance of two models. The first model, GFS-SWAN, used GFS as input into a computational domain with a large spatial resolution. The second mode, GFS-WRF-SWAN, use WRF as input into a computational domain with a small fine spatial resolution. This model used boundary input provided by the GFS-SWAN model. As a result of this study the following can be concluded:

1) GFS shows an ability to accurately predict typhoon routes given accurate initial typhoon location and conditions.
2) GFS-WRF wind forecast comparisons showed a tendency of over prediction with good agreement with the AMEDAS wind observations at Aomori and Mutsu.
3) GFS-SWAN model prediction results show good correlation coefficient of wave forecast in the Winter and Spring. Forecast during Fall shows decreasing correlation coefficient as the forecast time series progresses into the future. The rate of decrease is dependent on the ability of GFS to reproduce pressure systems. The greatest limitation of GFS during times of typhoon strength winds is the spatial resolution of three hours, where actual typhoon movement and strength is not tracked accurately.
4) WRF meso-scaled spatial resolution resolves small scale weather systems better than the synoptic-scale wind mesh of GFS. The GFS-WRF-SWAN model shows better performance over the GFS-SWAN model where complex topological features and meso-scaled wind systems influenced wind patterns.
5) Energy transfer model modifications in SWAN by Lalbeharry et al. (2004) has been shown improve wave height and period forecast correspondence with NOWPHAS buoy test points. In addition, using a large frequency range of 0.05 to 1.0 Hz decreases the forecast performance of the Lalbeharry et al. (2004) formulations. Showing its dependency on higher frequencies on the energy spectrum.

Chapter 4 Wave hindcasting and analysis

4.1 Introduction

Meteorological events such as typhoons and strong pressure systems are hazards that generate high waves and surges. Typhoon season in Japan last from August until December and high waves are frequently generated in the seas surrounding Japan. The majority of the typhoons generated in a season stay out at sea but the ones that make landfall generate high waves and large storm surges, causing damage to coastal structures in its path. Japan is well prepared for natural disasters as many protective structures have been built since the 1950's. Structures are built to withstand large surge and protect from flooding but occasionally failure occurs and heavy damage and loss of life occurs.

Evaluation after a disaster is important to assess the events that unfolded, locate the areas of weakness, and prepare for future events to prevent disaster. Hindcasting is an important tool used to investigate ocean waves during previous events.

A hindcast uses analysis datasets produced from available observational data as input and can be produced as soon as the analysis dataset becomes available. This section employs the wind-wave analysis system for wave hindcasting. Two tests were performed to determine the accuracy of the wind-wave analysis system.

First, hindcasting was performed for a typhoon event using default settings the GFS meteorological data input determine the general ability of the system to estimate wave parameters.

Second, hindcasting was performed for a typhoon event using three types of energy transfer models, two types of frequency ranges, and three types of meteorological data input. This series of test aimed to determine the influence of parameter setting on calculated output by the system.

4.2 Model description

4.2.1 System architecture

A Class I Linux Beowulf style cluster computer provides the hardware base of the computational system used in hindcasting. The system consists of a multi CPU cluster running a Linux operating system with inter-process communication controlled by MPICH2 (portable implementation of the Message Passing Interface standard). Refer to Section 2.2 for a detailed description of the systems infrastructure. Figure 4.1 represents the wind-wave analysis system as employed for hindcasting.

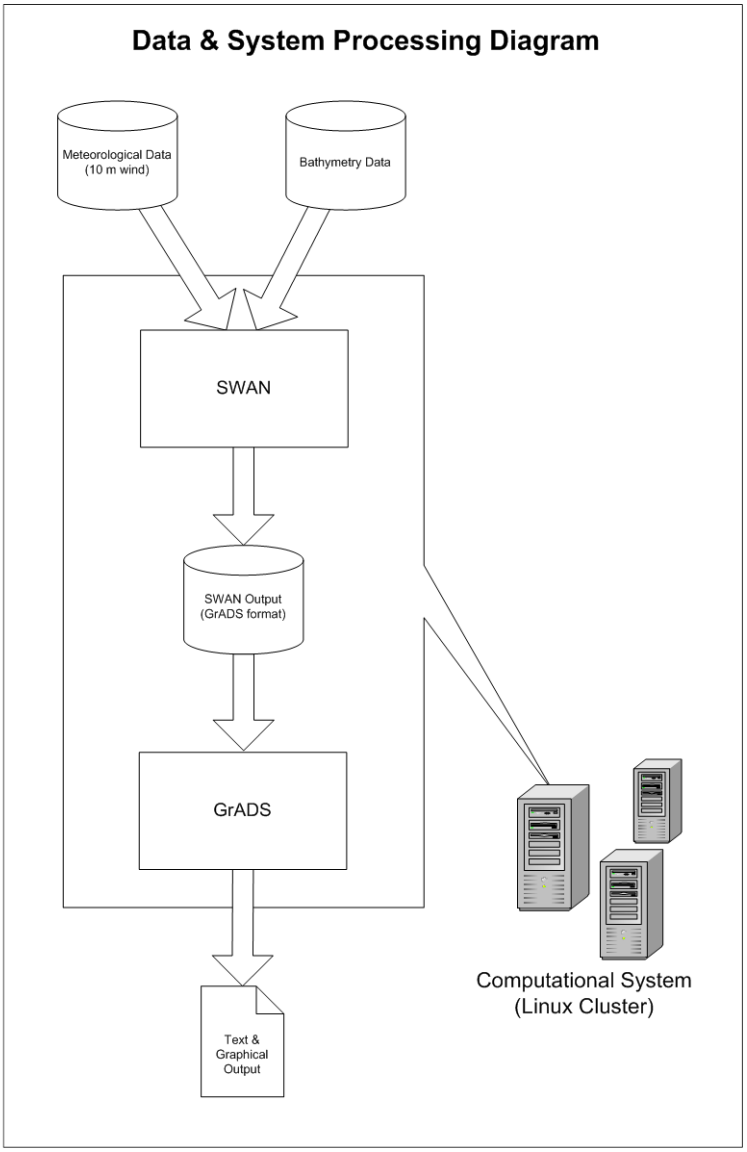

Fig. 4.1 System and data processing diagram

4.2.2 Wind analysis input

Meteorological wind input is required by the wind wave model and hindcasting requires datasets that best replicated the winds that have transcribed. Therefore the success of a hindcast system is not solely dependent on the wave model but also on the wind analysis grid.

All numerical weather prediction datasets start with an analysis grid, normally identified as a 00 dataset. The analysis data grid is calculated with available observational from various weather instruments and assimilated into a numerical weather prediction model. This analysis dataset is then used as a starting point for the model to produce a forecast.

The meteorological data described in Section 2.3, all contain an analysis data grid that can be used as input into the wave model. The temporal resolution of the dataset is equal to the time span between each data run, since only the analysis datasets are used as input. The GFS and FNL are calculated four times a day at (00, 06, 12, and 18 UTC) therefore the temporal resolution is six hours. The amount of observational data used to create the analysis data set of both the GFS and FNL represent the general differences. The GFS uses approximately two hours and forty five minutes and the FNL uses six hours of observations. NARR uses all available observations and is available with a temporal resolution of three hours.

Each dataset is available at different times for each processing run. The GFS is available roughly four hours after the analysis data start time. For example: the analysis dataset for 0000 GMT is available at 0400 GMT. FNL is not available until six hours after the dataset start time. NARR is not available in real-time, since all available data is used to create this dataset. See Figure 4.6 for an example of dataset availability.

The HAGPV dataset is produced every hour using observational data available from the wind profiler network, WINDAS. Data on the hour is delivered half past the hour. For example: the wind analysis dataset for 0100 is delivered on 0130. For a detailed discussion of the meteorological datasets refer to Sections 2.3.2, Synoptic-scale forecast and 2.3.3, Meso-scale forecast.

4.3 Verification

4.3.1 Analysis of the damaging effects caused by Typhoon Tokage

4.3.1.1 Event overview

On October 20th, 2004, described as the deadliest storm in a decade, Typhoon 0423 (named Tokage), made landfall in Japan over Tosa-Shimizu, near the southern tip of Shikoku while still at typhoon strength, causing severe coastal damage. When making landfall, it is estimated that the area of wind speed exceeding 25 m/s extended over a large area having a diameter of approximately 440km.

Typhoon 0423 was the tenth typhoon to strike Japan in 2004, exceeding a record previously set in 1990 of six typhoons making landfall in one year. Typhoon 0423 was the worst storm to strike Japan since Typhoon Mireille thirteen years before. According to the Fire and Disaster Management Agency (FDMA), there were 59 dead, 22 missing and 340 injured across 20 prefectures from Miyazaki to Chiba.

Typhoon Tokage caused flooding to approximately 25,000 homes and damaged 500 non-residential properties. There were flood barrier breaches at 9 locations and landslides at over 590 locations. .

The wind wave analysis system was employed to estimate waves generated by the typhoon.

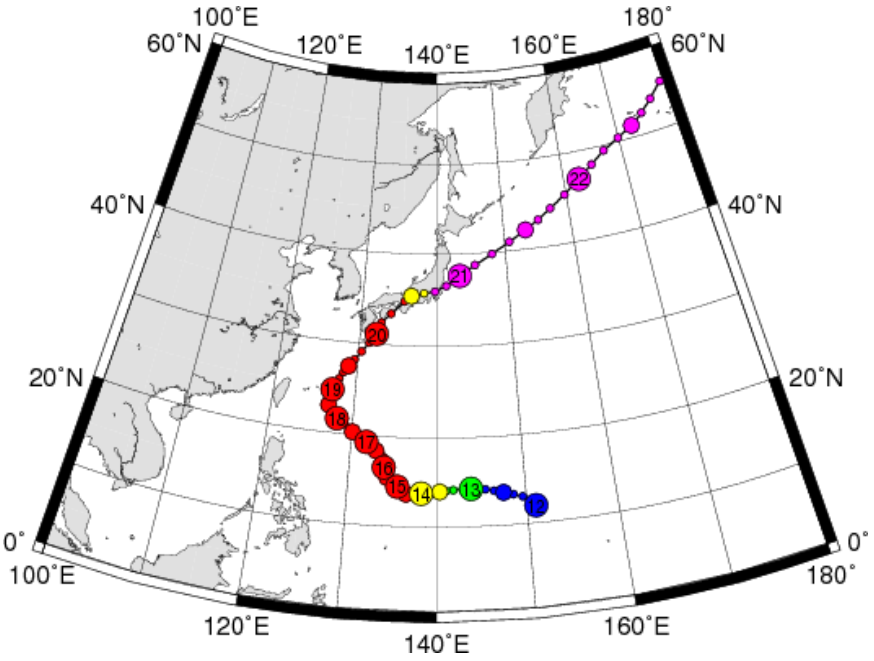

Fig. 4.2 Path of Typhoon 0423 (TOKAGI)

4.3.1.2 Model setup

The period of calculation was October 18th 2004 through October 21st 2004 with a temporal resolution of one hour. The calculation grid for testing used a spatial resolution of 0.25 degrees covering the typhoons path, (a longitudinal area from 120° E to 175° E and a latitudinal area from 5° N to 55° N).

The wave model SWAN was configured to use the default wave growth formulation of Komen et al. (1984) with Triads, quadruplet wave-wave interaction and whitecapping turned on.

GFS 10m wind data with a 1.0 degree spatial resolution from NCEP was obtained for the calculation period. Only analysis data was used and the temporal resolution of the GFS analysis data is six hours.

Bathymetric data consisted of 10 min spatial resolution, DBDB-V bathymetric data from Naval Oceanographic Office.

4.3.1.3 Observational data from NOWPHAS

Observational data from NOWPHAS for the point Murotsu (134°E 8' 52", 33°N 15' 59") was used to compare the forecasted wave heights and periods with the observed ones. The Murotsu buoy is a Doppler type directional wave meter with current measurement capability, located at a depth of 30 m with its sensor located .6 m from the bottom.

4.3.1.4 Comparison and evaluation

Figure 4.3 denotes the calculated wave height fields by using the hindcasted wind data with a 6 hour time interval. The typhoon caused severe damage along the coastal areas of Shikoku and Wakayama. Especially in Murotsu City, three people were killed when seawall parapets collapsed. The largest wave recorded at that time by the NOWPHAS gauges was 13.55 m and 15 sec (the largest recorded wave observation by the gauges since their activation).

Figure 4.4 shows the comparison of observed wave height change with the forecasted and hindcasted ones. There is little difference between forecasted and hindcasted wave heights. The tendency of change in observed wave height is rapid compared to calculated ones. The typhoon 0423 passed over the observed point; therefore, it is considered that wind direction and strength changed rapidly. Since the time interval of forecasting data is 3 hours and hindcast data is 6 hours, the time interval along with the 1.0 degree grid resolution is insufficient to reproduce the rapid change of wind fields, resulting in a smooth change of wave heights shown in Figure 4.3. Despite the tendency of wave height change, the peak value of wave heights agree fairy well.

Concerning with wave periods, due to the difference between definitions, the estimated values are smaller than the observed significant wave periods; however, the tendency of change in wave period is nearly the same, shown in Figure 4.5.

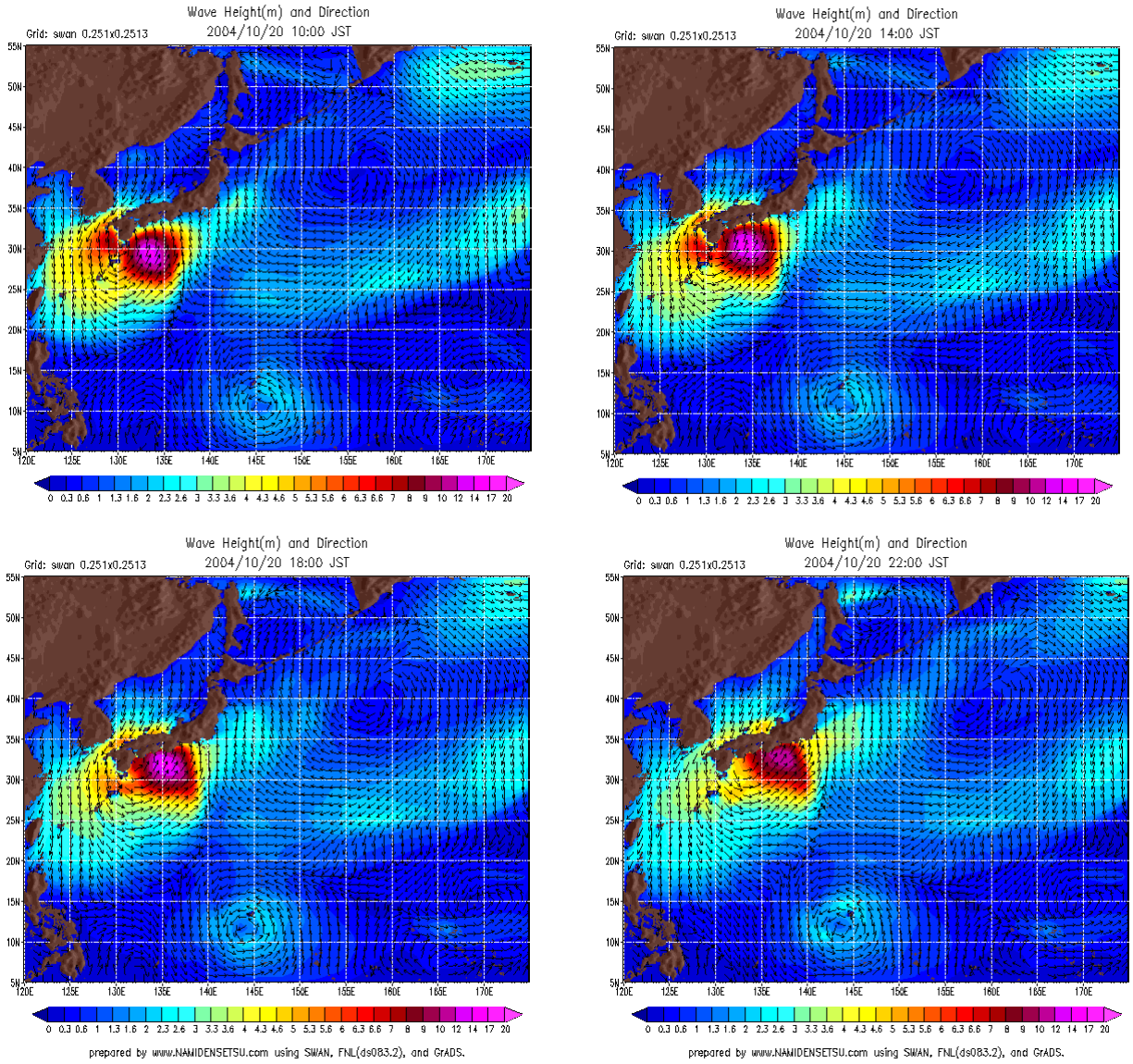

Fig. 4.3 Estimated wave heights due to Typhoon 0423

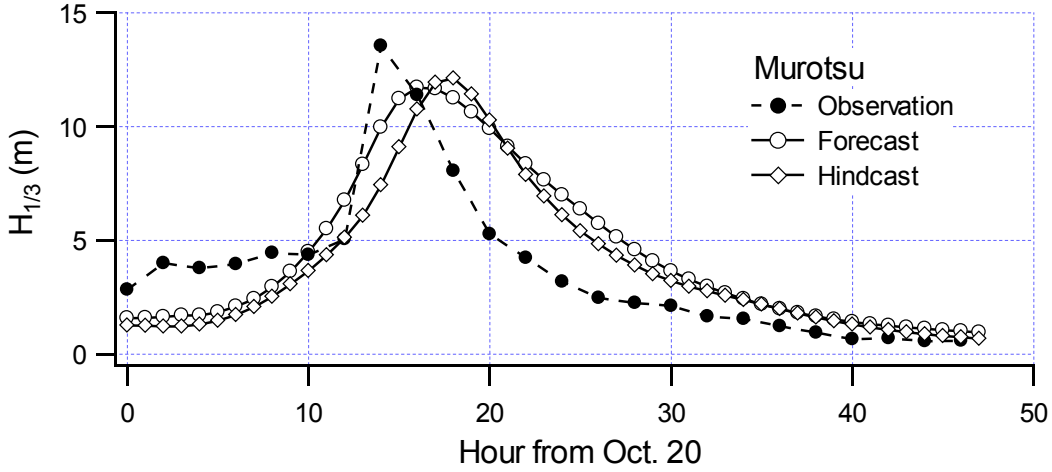

Fig. 4.4 Comparison of observed wave heights with forecasted and hindcasted ones

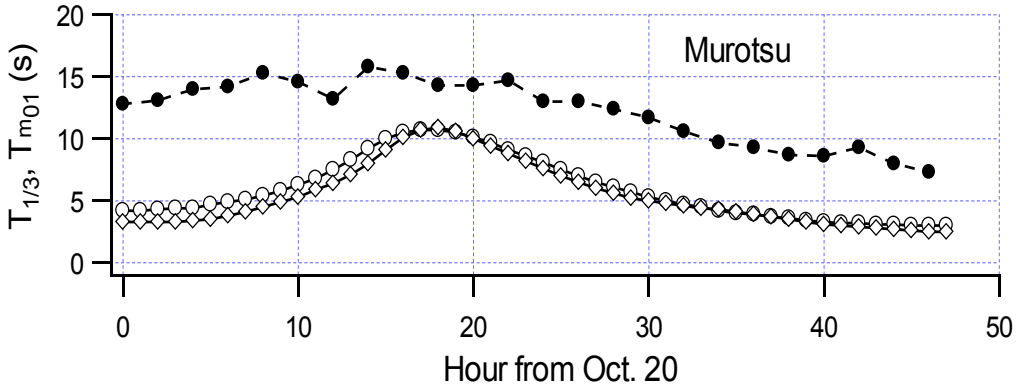

Fig. 4.5 Comparison of observed wave periods with forecasted and hindcasted ones

4.3.1.5 Summary

This study used GFS analysis data to hindcast the ocean conditions generated by Typhoon Tokage. Prediction accuracy was verified by comparing calculated results with the NOWPHAS buoy at Murotsu. Although slightly under reported, calculated hindcast showed good wave peak height prediction. The spatial and temporal resolution hindered the tendency of wave height change. The one hour temporal resolution of the computational domain could not account for sudden increases within an hour of wind change therefore hindering changes of wave height growth. The tendency of change for wave period is similar to the tendency of change for wave heights but overall wave period is generally under predicted. Overall hindcasting ability of the wind-wave system by the SWAN wave model to predict wave heights has been shown to be reliable.

4.3.2 Analysis of high waves generated by Hurricane Katrina

Hurricane Katrina was a devastating storm that inflicted catastrophic damage and high loss of life from Louisiana to Florida. The ability to accurately forecast high seas and storm surges remains a necessary skill to warn and prepare for potential disaster. This paper evaluated wave prediction accuracy by using three energy transfer models (Komen et al., 1984; Janssen, 1991; Lalbeharry et al., 2004) in SWAN (Simulating WAves Nearshore) version 40.41, together with three different meteorological 10m wind data (GFS, FNL and NARR). SWAN hindcast runs, using combinations of each energy transfer model and wind data, were performed employing two different frequency ranges for the calculation. Hindcast results were compared with observational data from 11 NDBC (National Data Buoy Center) stations to verify performance. Modified Janssen model by Lalbeharry et al. (2004) produced very good significant wave heights and mean wave periods using frequency range of 0.04 to 0.5 Hz. Good correlation coefficient and low error bias were shown in test cases when using the smaller frequency range. During the period of peak wind speeds at NDBC station 42040, Lalbeharry et al.'s model using the smaller frequency range well estimated the hurricane's peak significant wave height. Conversely, results using the frequency range of 0.04 to 1.0 Hz were undesirable. Modifications by Lalbeharry et al. (2004) showed dependency on upper frequencies in the calculation.

4.3.2.1 Event Overview

During August 25th to 31st, 2005, Hurricane Katrina created a path of destruction first in Southern Florida then in parts of Southwest Louisiana, Mississippi, and Alabama. According to Knabb et al. (2005), Katrina formed as a tropical storm in the southern Bahamas and strengthened over the central Bahamas on its way to making its first landfall on Southern Florida as a Category 1 hurricane (Saffir-Simpson Hurricane Scale) on August 25th, 2005. Weakening over land, it re-emerged over the Gulf of Mexico then rapidly intensified. About 314.8 km southeast of the mouth of the Mississippi River, Katrina attained its peak intensity as a Category 5 hurricane on August 28th, with winds of 77 m/s. Tropical storm force winds extended 370.4 km from its center, making Katrina not only extremely intense but also very large. On August 29th it made its second landfall in Louisiana as a Category 3 hurricane with estimated maximum sustained winds of 56.5 m/s and central pressure of 920 hPa. Katrina then headed northward across the Louisiana delta and made a third landfall at the mouth of Pearl River on the Louisiana and Mississippi border with the wind speed of 54 m/s. Katrina weakened rapidly after moving inland over Mississippi and continued to weaken as it moved north northeastward. By August 30th, Katrina was a tropical depression over Tennessee.

Very high winds occurring along a rather large area in Katrina's path just prior to landfall, with the highest winds in the right-front quadrant, generated high seas with an enormous storm surge. The storm surge and high waves produced by Katrina severely strained the levee system in New Orleans. The magnitude of damage, destruction and fatalities caused by

Katrina created a great need for assessment. Since all of the measurement gauges close to shore were destroyed, the only way of determining water levels were from markings on remaining structures. Wave and surge models were used to determine conditions created by Hurricane Katrina.

The two motivations behind this study are: (1) To determine conditions created by Hurricane Katrina by modeling waves that were generated and (2) To evaluate wave prediction accuracy using three energy transfer models (Komen et al., 1984; Janssen, 1991; Lalbeharry et al., 2004) in SWAN (Simulating WAves Nearshore) version 40.41, together with three different meteorological 10m wind data of Global Forecast System (GFS), Final Analysis (FNL) and North America Regional Reanalysis (NARR). SWAN hindcast runs, using combinations of each energy transfer model and wind data, are performed for two different frequency ranges in spectral calculations. Hindcast results are compared with observational data from 11 National Data Buoy Center (NDBC) stations to verify performance.

4.3.2.2 Model Setup

4.3.2.2.1 Computational domain

The calculation grid for testing used a spatial resolution of 0.25 degrees covering the general Gulf of Mexico area (a longitudinal area from 100° W to 80° W and a latitudinal area from 18° N to 33° N). Spectral directions were on a full 360 degrees divided into 20 degree bins. Two sets of discrete frequency ranges were used: (1) 0.04 Hz to 0.5 Hz with 25 frequencies, and (2) 0.04 Hz to 1.0 Hz with 25 frequencies. The calculation time step was set to 30 minutes.

4.3.2.2.2 Numerical prediction model

$$S_{in}(\sigma,\theta) = A + BE(\sigma,\theta) \tag{4.1}$$

SWAN offers two options for the coefficient B in Eq. (3) that can be optionally set. The first option was taken from the WAM Cycle-3 model (WAMDI group 1988) and is based on formulations of Komen et al. (1984). The second option was taken from the WAM Cycle-4 model (Komen et al. 1994) and is based on formulations of Janssen (1991). Where, winds and waves are coupled by having a feedback of growing waves on the wind profile. Feedback enhances the growth of younger wind waves over older wind waves for the same source wind.

Selecting the first option activates source term formulations by Komen et al. (1984) and the second option activates formulations by Janssen (1991). These two transfer models differ in the S_{in} and S_{ds} source terms. The S_{in} source term differ as described above and the S_{ds} source term use different formulation constants in wave energy dissipation.

This study examined the two available energy transfer models provided by SWAN along with a model that modifies Janssen's formulation (1991) described by Lalbeharry et al. (2004) who notes that implementation of the Janssen's formulation (1991) in SWAN differs from the formulation used in WAM Cycle-4. Two specific differences were noted:

1) The shift growth parameter $z_\alpha = 0.011$ has not been implemented in the exponential wind growth source term of SWAN, and
2) The wave growth limiter implemented in SWAN differs that in WAM Cycle-4.

SWAN was set to use third generation physics for testing with the triad wave-wave interaction option activated.

4.3.2.2.3 Meteorological input data

Three types of meteorological input data was used in this study. First, the Global Forecast System (GFS) distributed four times a day (00, 06, 12 and 18 UTC). The analysis grid of each run is produced by using observational data collected for 2 hours and 45 minutes past the synoptic time.

Second, the Final Global Data Assimilation System (FNL) is similar to the GFS and distributed run four times a day. The analysis grid of each run is produced by using, 'first guess' (3, 6, and 9 hour forecast from the previous synoptic time run) and observational data collected for up to 6 hours past the synoptic time.

Third, the North American Regional Reanalysis (NARR) has a horizontal resolution of 32 km and a vertical resolution of 45 layers. NARR assimilates all available observational data into each corresponding analysis dataset. The NARR is available in three hour increments.

For a discussion on GFS and FNL refer to Section 2.3.2.1 and for NARR refer to Section 2.3.2.2.

The only analysis dataset of each type of meteorological input data was used. The temporal resolution of GFS and FNL were six hours and the temporal resolution of NARR was three hours. Figure 4.6 shows the outline of each meteorological data mentioned above.

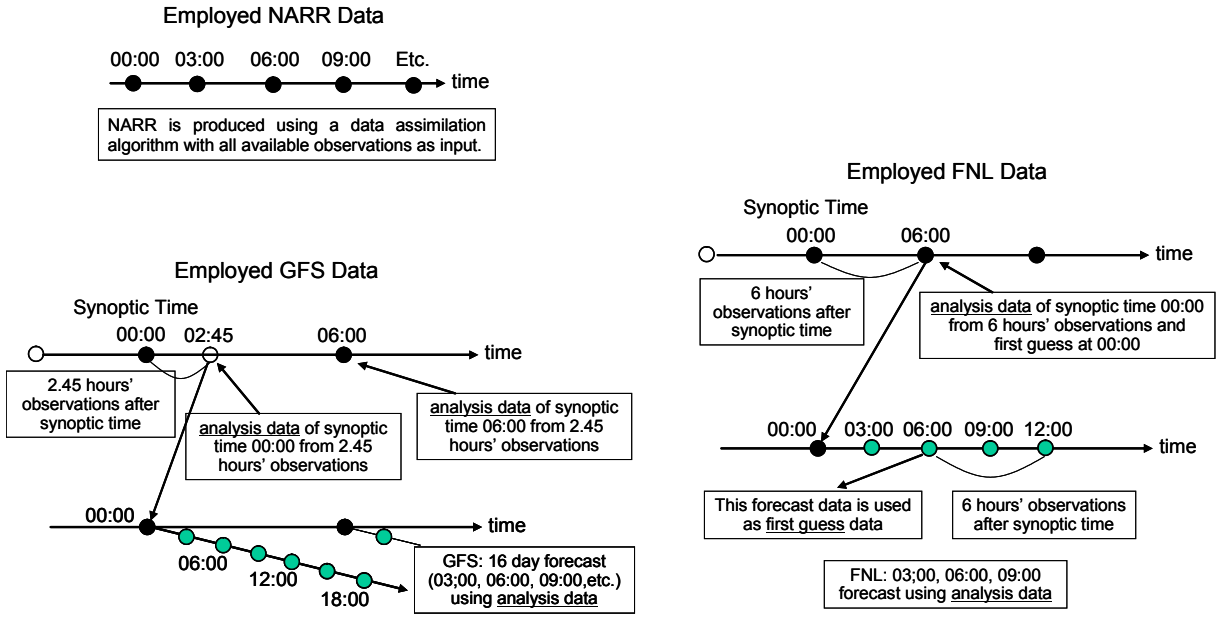

Fig. 4.6 Meteorological datasets used in this study

4.3.2.2.4 Bathymetric data

Bathymetric data for the Gulf of Mexico and surrounding shoreline was extracted from the, 'GEBCO 1-minute bathymetric grid'. The GEBCO (General Bathymetric Chart of the Oceans) dataset provides bathymetry data on a global grid with a one arc-minute spacing and is available to download from the following link: http://www.ngdc.noaa.gov/mgg/gebco/. GEBCO is an international project under the joint auspices of the International Hydrographic Organization and the Intergovernmental Oceanographic Commission of UNESCO. Its goal is to provide the most authoritative, publicly-available bathymetry for the world's oceans.

4.3.2.3 Observational data from NDBC

Model performance was examined by comparing calculated hindcast data with observational data from 11 locations National Data Buoy Center (NDBC) station throughout the Gulf of Mexico, as shown in Figure 4.7. Historical hourly observations (including wind speed and direction, significant wave height, and mean wave period) were obtained for the period from August 25th to 30th from the NDBC ftp server.

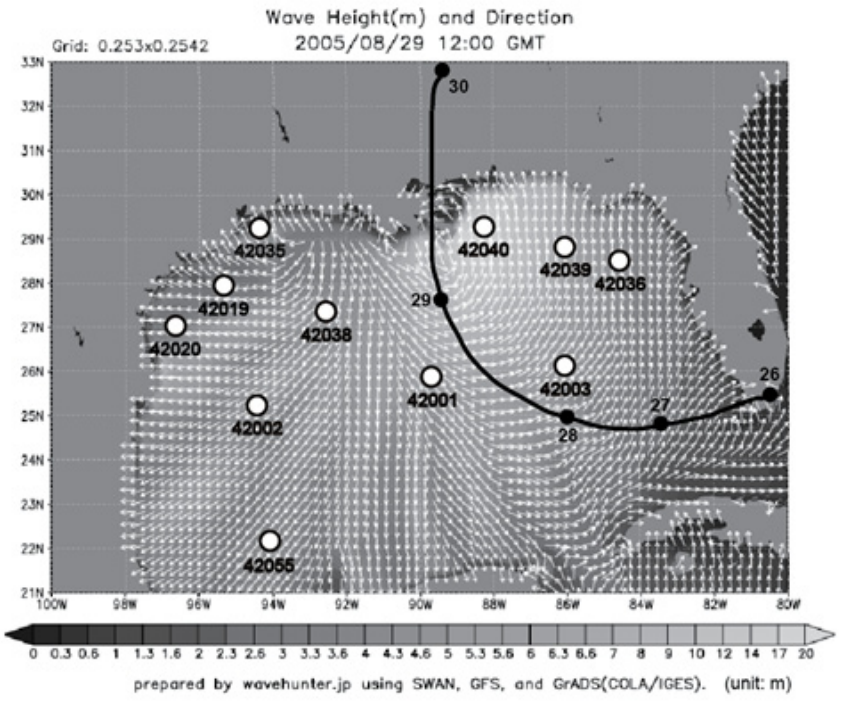

Fig. 4.7 NDBC station locations, Hurricane Katrina's track and significant wave height at 8/29/2005 12:00 GMT

4.3.2.4 Performance examination

4.3.2.4.1 Statistical Analysis

The following statistics were used to evaluate the accuracy of predicted significant wave height, H_s, and mean wave period, T_m. *Bias* shown in Eq. (4.2) allows examination of the calculated error margin to determine the tendency of over or under prediction. Correlation coefficient r in Eq. (4.3) measures the correlation between the predicted and observational values. Root mean-squared error *RMSE* in Eq. (4.4) is another way of examining error. Symmetric slope s of linear correlation plots is given in Eq. (4.5).

$$bias = \frac{1}{n}\sum_{i=1}^{n}\left(P_i - O_i\right) \tag{4.2}$$

$$r = \frac{1}{n}\sum_{i=1}^{n}\left(O_i - O_{mean}\right)\left(P_i - P_{mean}\right)/\left(\sigma_P \sigma_O\right) \tag{4.3}$$

$$RMSE = \sqrt{\frac{1}{n}\sum_{i=1}^{n}\left(P_i - O_i\right)^2} \tag{4.4}$$

$$s = \sqrt{\sum_{i=1}^{n}\left(O_i\right)^2 / \sum_{i=1}^{n}\left(P_i\right)^2} \tag{4.5}$$

In Eqs. (4.2) to (4.5), P_i represents prediction, O_i observation, n the number of observations, P_{mean} the prediction mean, O_{mean} the observation mean, σ_p the standard deviation of predictions and σ_o standard deviation of observations.

4.3.2.4.2 Meteorological Data Evaluation

In this section, the wind data of NARR, GFS and FNL are presented during Hurricane Katrina with the statistical parameters described in Section 4.1. The statistic of wind speeds are listed in Table A1.

4.3.2.4.2.1 NARR 10 m wind data

Of the three wind datasets used, the NARR data contained the most observational data, highest spatial and highest time resolutions; however, NARR data showed a tendency to contribute to under-prediction as listed in Table A1. When comparing *Bias* and *RMSE* of NARR with those of GFS and FNL, the average values for NARR show -0.35 and 1.59; in the cases of GFS and FNL, *Bias* and *RMSE* are presented -0.19 and 1.52, and -0.28 and 1.51, respectively. Although *RMSE* of NARR is similar to those of GFS and FNL, *Bias* of NARR is smaller than those of others. On the other hands, the correlation coefficient r and the symmetric slope s indicate the similar values for NARR, GFS and FNL.

NDBC station 42040 is located approximately 118.5 km south of Dauphin Island, Alabama. On August 29, 2005, a significant wave height of 16.91 m was reported, and the closest point of approach was 135.2 km. Wind speed at station 42040 during the report was 28.2 m/s and maximum sustained winds near the storms center was 64.8 m/s. The left figure in Figure 4.8 shows a scatter plot of wind speeds from NARR compared against observations at the NDBC station 42040. Generally, the NARR dataset shows under-estimation wind speed during the period of peak winds at the station.

4.3.2.4.2.2 GFS and FNL 10 m wind data

The averaged values of RMSE, r and s for both GFS and FNL are similar, but the averaged *bias* of GFS is slightly different from that of FNL; these are -0.19 and -0.28, respectively (see, Table A1). For example, the middle and right figures shown in Fig. 4.8 denote that GFS and FNL had a tendency to over-estimation wind speeds during the period of peak winds at NDBC station 42040. FNL data showed slightly better reporting of wind speed during this period at this station. However, both datasets showed similar results in each of the test cases that used these two datasets.

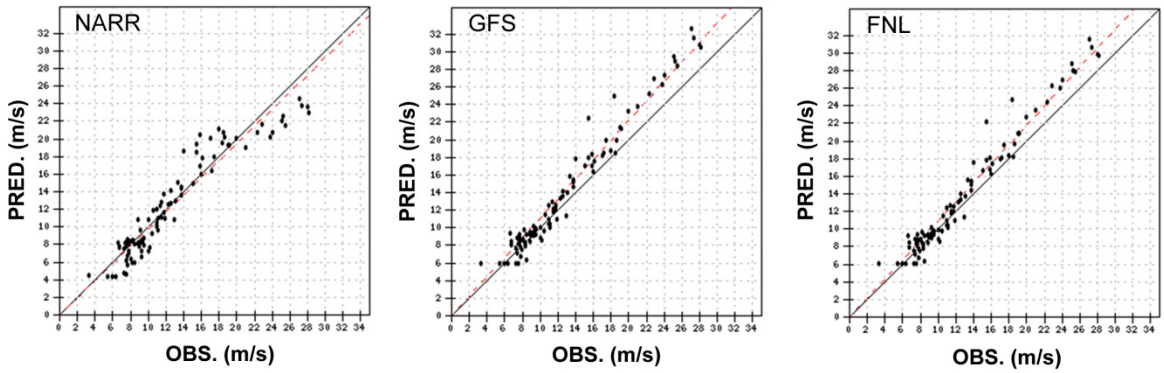

Fig. 4.8 Scatter plot of NARR, GFS and FNL wind speeds at NDBC station 42040

4.3.2.4.3 Energy Transfer Model Evaluation

The correlation coefficients for significant wave height and mean wave period at 11 locations are shown in Figures 4.9 and 4.10, respectively. Figure 4.11 shows time series of observations and estimations of wave height and period together with wind speed and direction at station locations, 42001, 42038, 42039 and 42040 when using GFS wind data.

Figures 4.15 and 4.16 show the comparisons of observed and predicted significant wave heights using the different frequency ranges in calculation. Concerning with wave periods, those scatter plots are depicted in Figs. 4.17 and 4.18.

4.3.2.4.3.1 Komen et al. (1984)'s formulation

First, significant wave heights (SWH) and mean wave periods (MWP) were examined using statistical analysis with respect to three wind data used in this study. The averaged correlation coefficients of SWH obtained from NARR were 0.92 and 0.93 for frequency ranges of 0.04 to 1.0 Hz and 0.04 to 0.5 Hz (Table 4.3). Also, those were 0.92 and 0.92, and 0.92 and 0.93 for GFS and FNL, respectively (Figs. 4.15 – 4.16 and Tables 4.4 - 4.5). The averaged correlation coefficients of MWP from NARR were 0.85 and 0.84 for each frequency range respectively (Table 4.6). Similarly, those were 0.85 and 0.86, and 0.85 and 0.87 for GFS and FNL, respectively (Figs. 4.7 – 4.18 and Tables 4.7 – 4.8). That is, Komen's formulation showed generally good averaged correlation coefficients for both SWH and MWP as indicated by similar results of the three types of wind data.

The statistical parameters of *bias* and *RMSE* for SWH and MWP showed similar results to the correlation coefficient associated with each type of wind data. Two parameters of SWH showed similar values for two frequency ranges of all wind data (Tables 4.3 to 4.4). But it was shown that the values of *RMSE* in MWP for two frequency ranges were slightly different (Tables 4.6 to 4.7).

Next, predicted SWH and MWP using GFS wind data were compared with observations at four stations (Fig. 4.15 to 4.18). At stations 42039 and 42040, located on the right of the Hurricane's track, predicted SWH for two frequency ranges were generally under-estimated, especially for larger wave heights at station NDBC 42040. At station 42038, which is far from the track, predicted SWH was similarly under-estimated. At station 42001, which is closest to the track, predicted SWH was over-estimated for two frequency ranges. In the case of MWP, predicted MWP were generally under-estimated at all stations. The mean wave period was more sensitive to various wind fields than was the significant wave height when using Komen et al. (1984)'s formulation. In addition, the change of the frequency range did not show notable influence on the significant wave height and the mean wave period.

4.3.2.4.3.2 Janssen (1991)'s formulation

In general, Janssen's formulation employed using GFS wind data, showed good correlation coefficients for two frequency ranges of both SWH and MWP, as shown in Figs. 4.9 and 4.10. The averaged *bias* and *RMSE* of SWH indicate that there were no large differences between results using frequency ranges of 0.04 to 1.0 Hz and 0.04 to 0.5 Hz as listed in Table 4.4. In the case of MWP, the averaged RMSE showed similar values for two frequency ranges. But there was a slight difference in the values of *Bias,* -1.05 and -0.44, between the frequency ranges of 0.04 to 1.0 Hz and 0.04 to 0.5 Hz, respectively.

When comparing the prediction to the observation in a scatter plot, the predicted significant wave height and mean wave period were under-estimated as shown in Figs. 4.15 to 4.18. Predicted wave heights for two frequency ranges were generally lower than those using Komen et al. (1984)'s formulation; on the other hand, mean wave period predictions became larger. Using a smaller frequency range of 0.04 to 0.5 Hz slightly improved both significant wave height and mean wave period results compared to the observations. Changing of the frequency range did not generally affect the correlation coefficient.

4.3.2.4.3.3 Modified Janssen (1991) formulation by Lalbeharry et al. (2004)

Modified Janssen's formulation (1991) by Lalbeharry et al. (2004) was employed using three types of wind data. To investigate the variations of SWH and MWP as changing the frequency ranges with three wind data types, the correlation coefficient was analyzed as shown in Figs. 4.9 and 4.10. The averaged correlation coefficients of SWH for 0.04 to 1.0 Hz frequency range and 0.04 to 0.5 Hz range were 0.84 and 0.94, 0.86 and 0.92, and 0.87 and 0.92 for NARR, GFS and FNL, respectively. In the case of MWP, those were 0.7 and 0.88, 0.69 and 0.87, and 0.69 and 0.89 for three wind data, respectively. From each averaged correlation coefficient, the values of SWH and MWP using the frequency range of 0.04 to 0.5 Hz became better than those using the range of 0.04 to 1.0 Hz.

Test cases employing the energy transfer model modifications by Lalbeharry et al. (2004) with GFS and FNL wind input using frequency range of 0.04 to 0.5 Hz showed generally good correlation coefficient, bias and *RMSE* for significant wave height and mean wave period wind input. Figures 4.11 to 4.14 shows time series of the significant wave height and the mean wave period calculated using modification model by Lalbeharry et al. (2004), together with GFS wind speed and direction at NDBC stations of 42001, 42038, 42039 and 42040. At stations 42001 and 42038, the predictions of SWH and MWP was over-estimated. On the other hand, at station 42039 and 42040 their predictions agreed well with the observations. In addition, it can be noted that this model provided good significant wave height during the period of peak wind strength at NDBC station 42040 as shown in Figs. 4.11 to 4.14. Station 42040 was located closest to Katrina during the hurricanes peak intensity.

When comparing all predicted results by changing the conditions, Lalbeharry et al.'s model produced the best overall results with good correlation coefficient and low error bias when using the smaller frequency range. Conversely, this model produced the worst results using the larger frequency range.

Table 4.1 shows the summary of the hindcast results judged from statistics shown by Eqs. (4.2) to (4.5): in this table the judgment is shown by 'good' using the symbol ○, 'relatively good' △, 'relatively bad' ▲ and 'bad' ●.

Table 4.1 Summary of simulations judged from statistics

	North American Regional Reanalysis (NARR)				Global Forecast System (GFS)						Final Global Data Assimilation		
NDBC	Komen et al (1984)		Lalbeharry et al (2004)		Komen et al (1984)		Janssen (1991)		Lalbeharry et al (2004)		Komen et al (1984)		Lalbeharry et al
Station	0-1.0 Hz	0-0.5 Hz	0-1.0 Hz	0-0.5 Hz	0-1.0 Hz	0-0.5 Hz	0-1.0 Hz	0-0.5 Hz	0-1.0 Hz	0-0.5 Hz	0-1.0 Hz	0-0.5 Hz	0-0.5 Hz
42001 (L)	○	○	○	○	▲	△	○	○	●	●	△	△	●
42002 (L)	○	○	●	○	△	△	○	○	△	▲	△	△	▲
42003 (R)	▲	○	△	△	○	○	▲	▲	△	○	○	○	○
42019 (L)	○	△	●	○	○	○	△	△	●	○	○	○	○
42020 (L)	○	○	●	○	○	○	○	○	●	○	○	○	○
42035 (L)	○	○	●	○	○	○	○	○	●	○	○	○	○
42036 (R)	○	○	●	○	○	○	△	△	△	○	○	○	○
42038 (L)	○	○	●	○	○	○	△	△	●	○	○	○	○
42039 (R)	△	△	●	○	△	△	●	●	△	○	△	△	○
42040 (R)	●	●	●	●	△	△	●	●	○	○	△	△	○
42055 (L)	○	○	●	○	○	○	○	○	▲	○	○	○	○

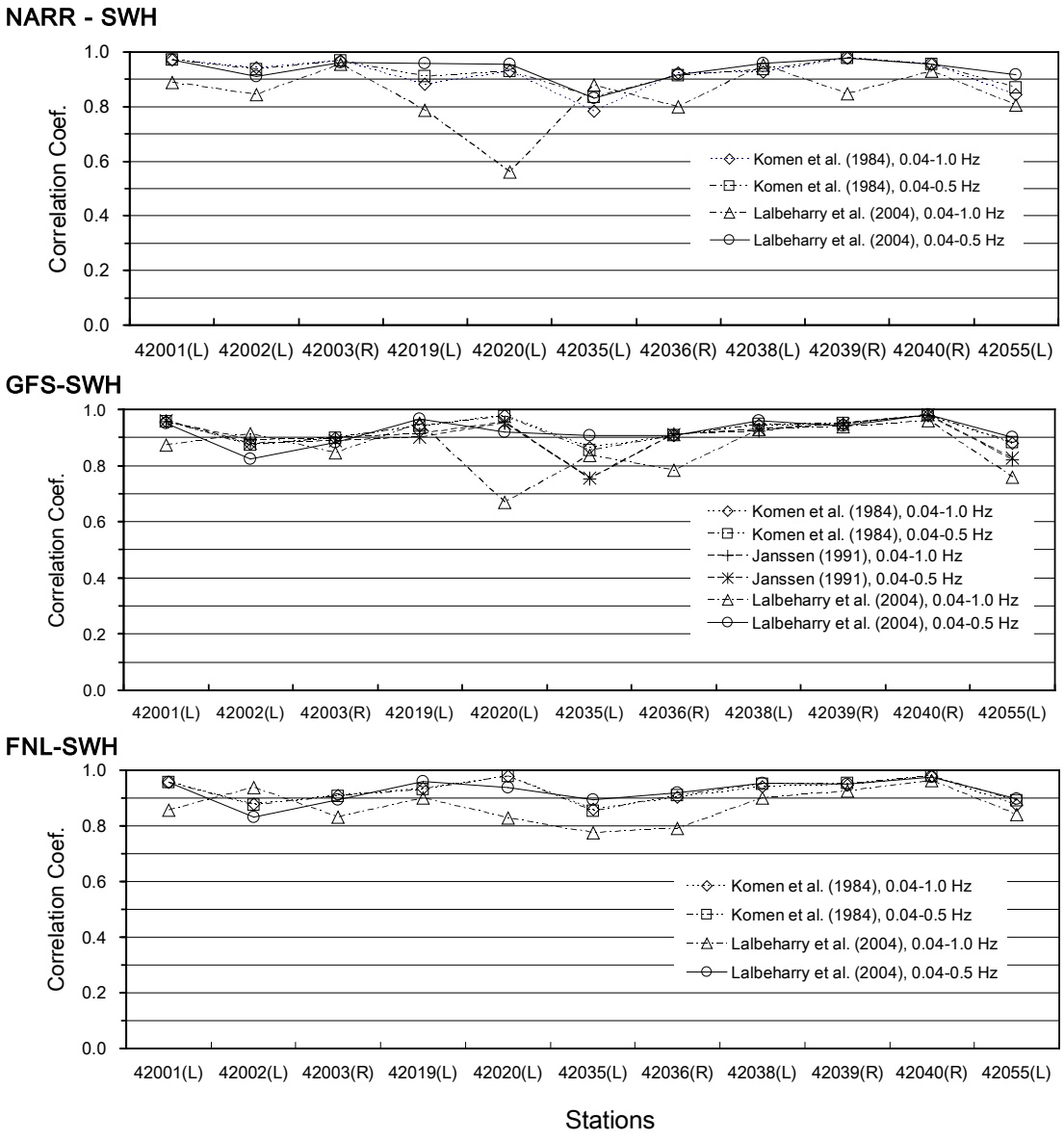

Fig. 4.9 Correlation coefficient for significant wave height (SWH) at 11 locations of NDBC station

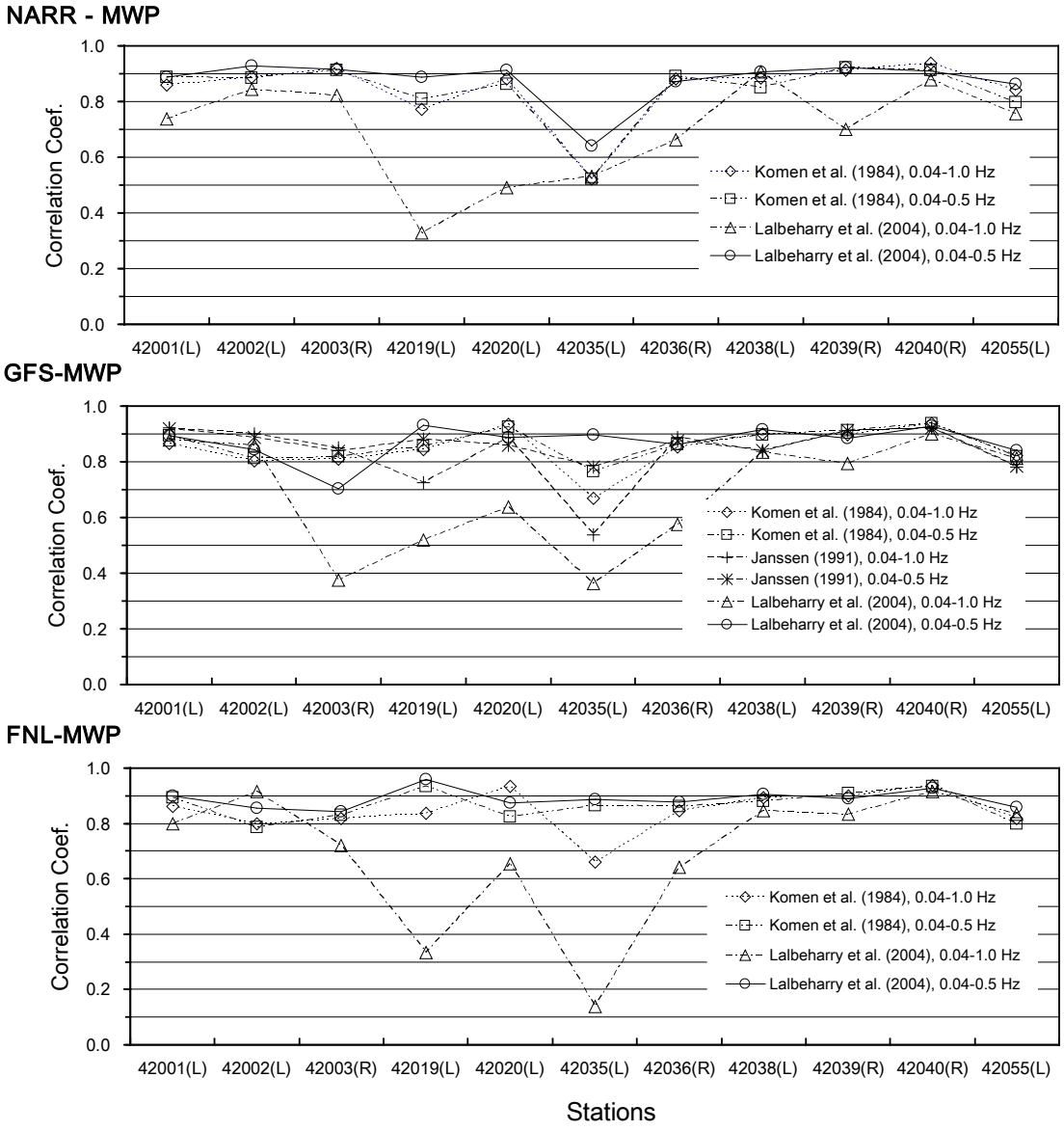

Fig. 4.10 Correlation coefficient for mean wave period (MWP) at 11 locations of NDBC station

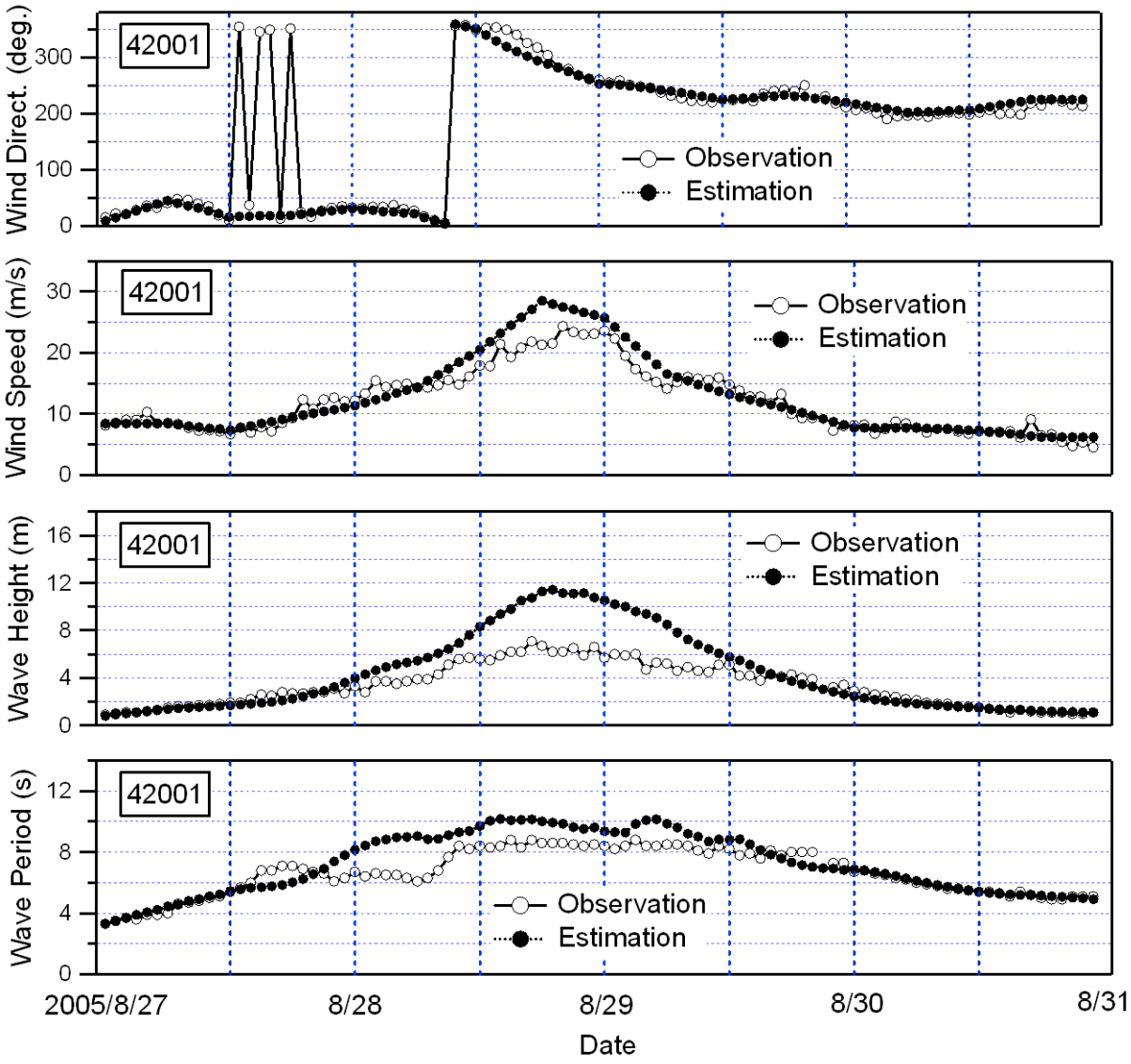

Fig. 4.11 Time series of significant wave height and mean wave period calculated using modification model by Lalbeharry et al. (2004), together with GFS wind speed and direction at NDBC stations 42001

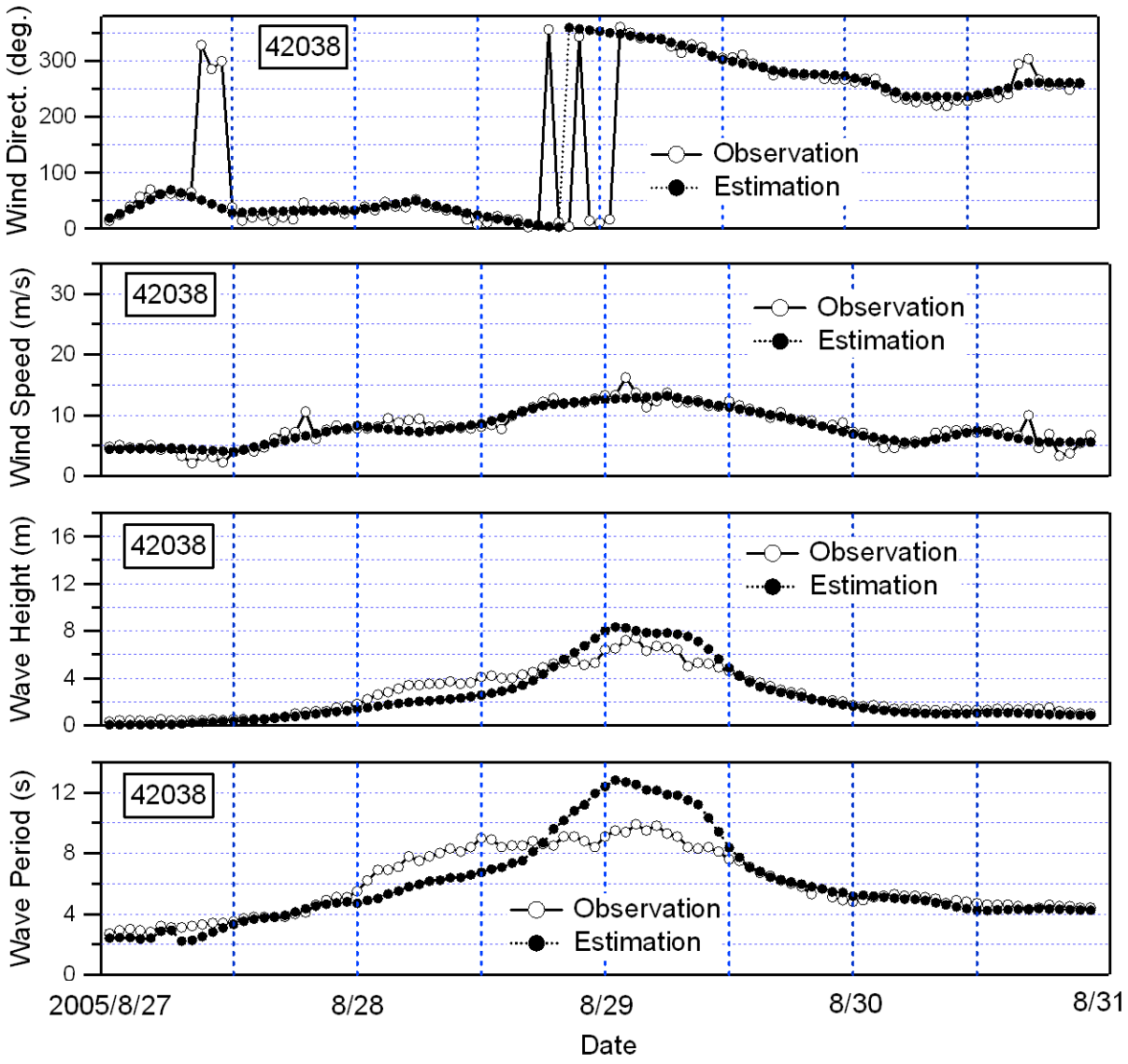

Fig. 4.12 Time series of significant wave height and mean wave period calculated using modification model by Lalbeharry et al. (2004), together with GFS wind speed and direction at NDBC stations 42038

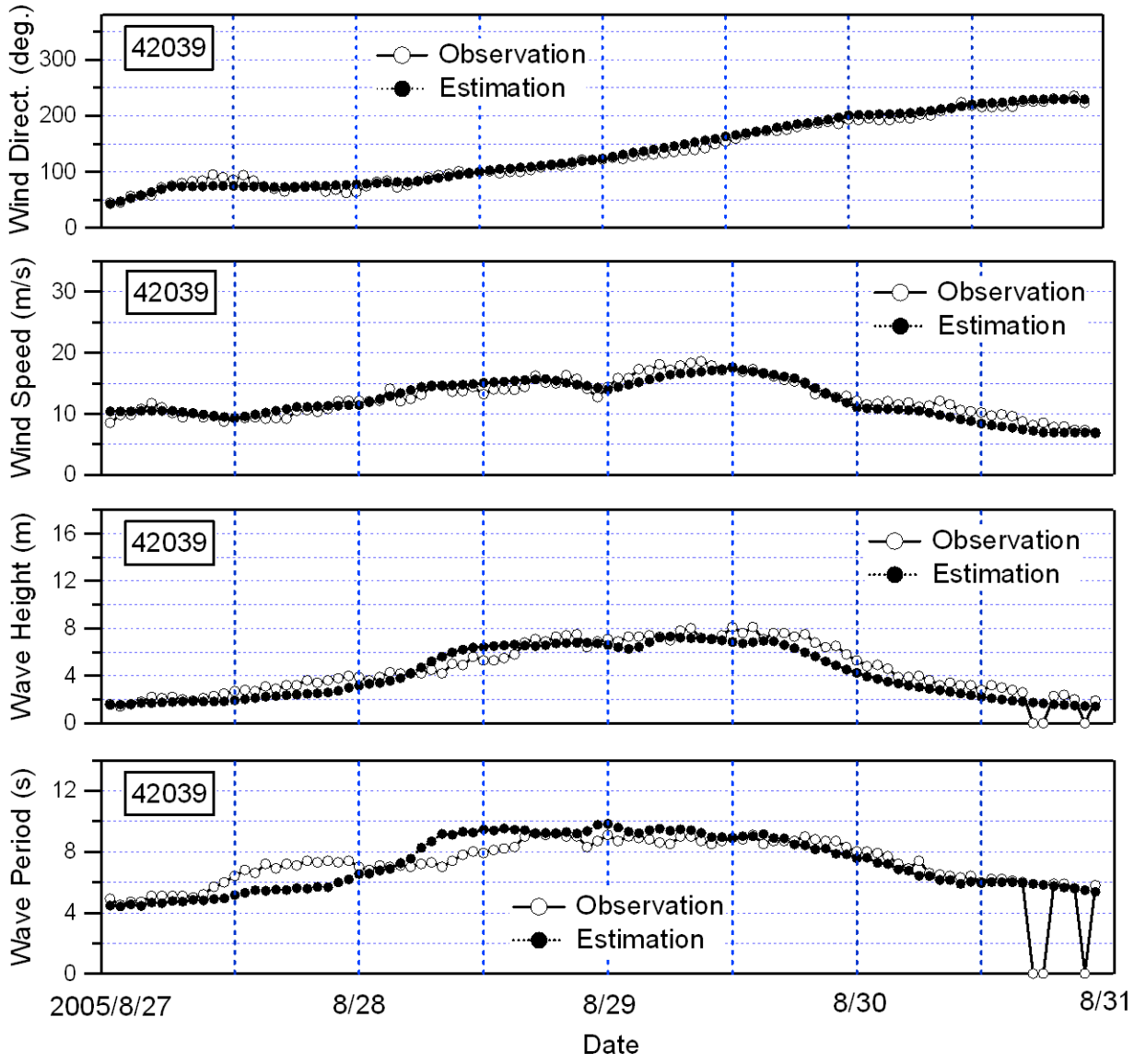

Fig. 4.13 Time series of significant wave height and mean wave period calculated using modification model by Lalbeharry et al. (2004), together with GFS wind speed and direction at NDBC stations 42039

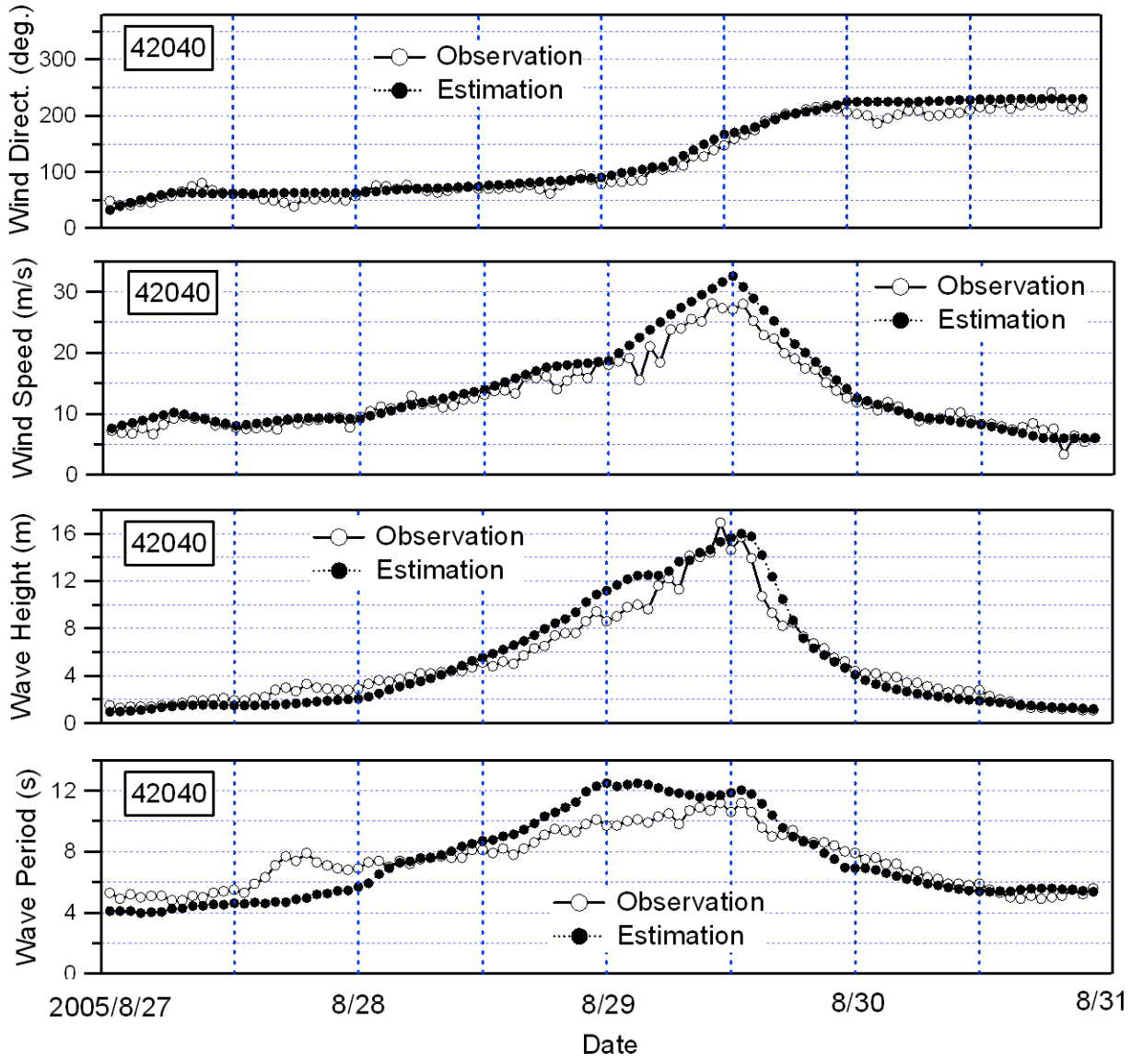

Fig. 4.14 Time series of significant wave height and mean wave period calculated using modification model by Lalbeharry et al. (2004), together with GFS wind speed and direction at NDBC stations 42040

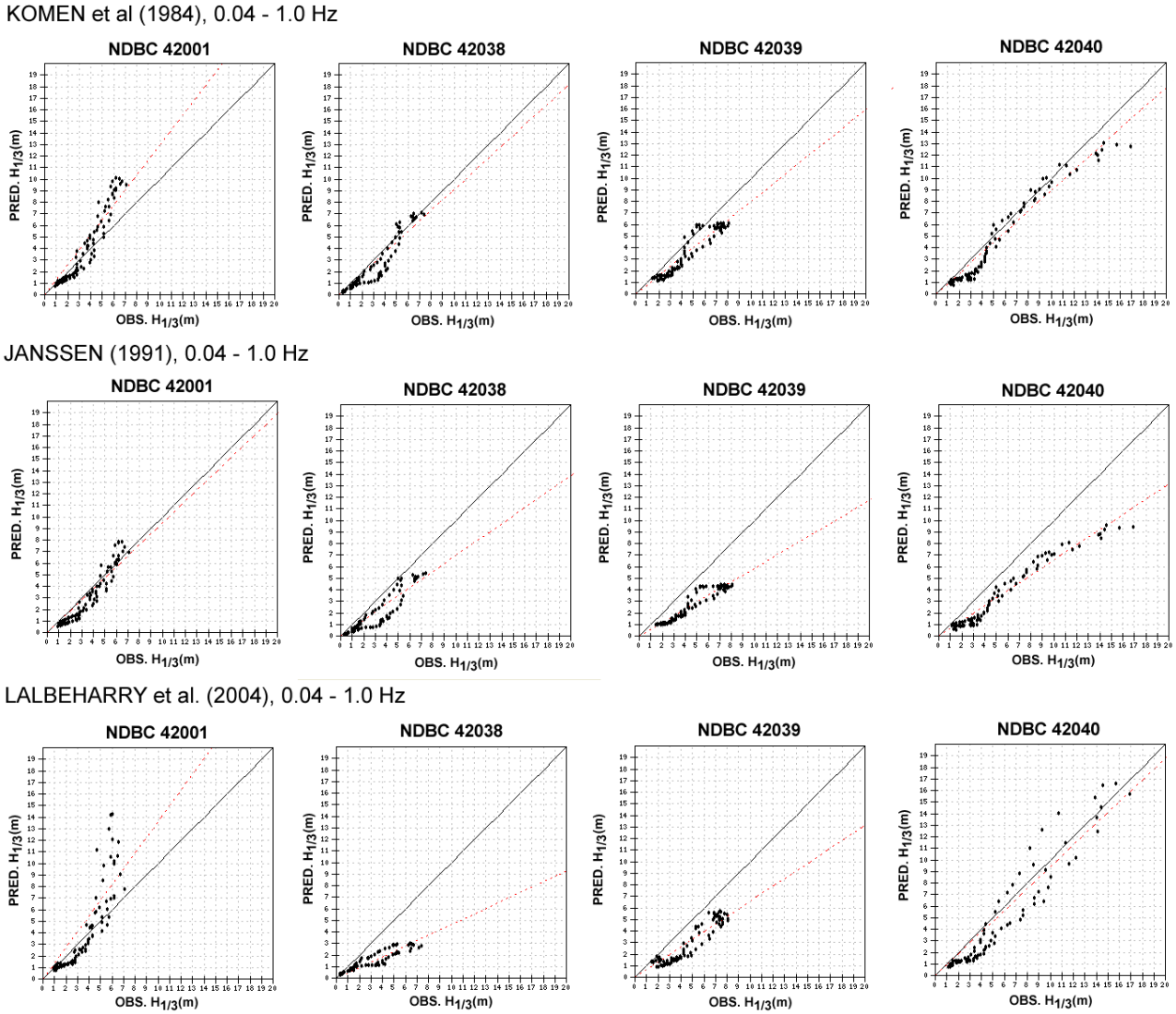

Fig. 4.15 Comparison between observed and predicted significant wave heights using 0.04 – 1.0 Hz frequency range with the wind data of GFS

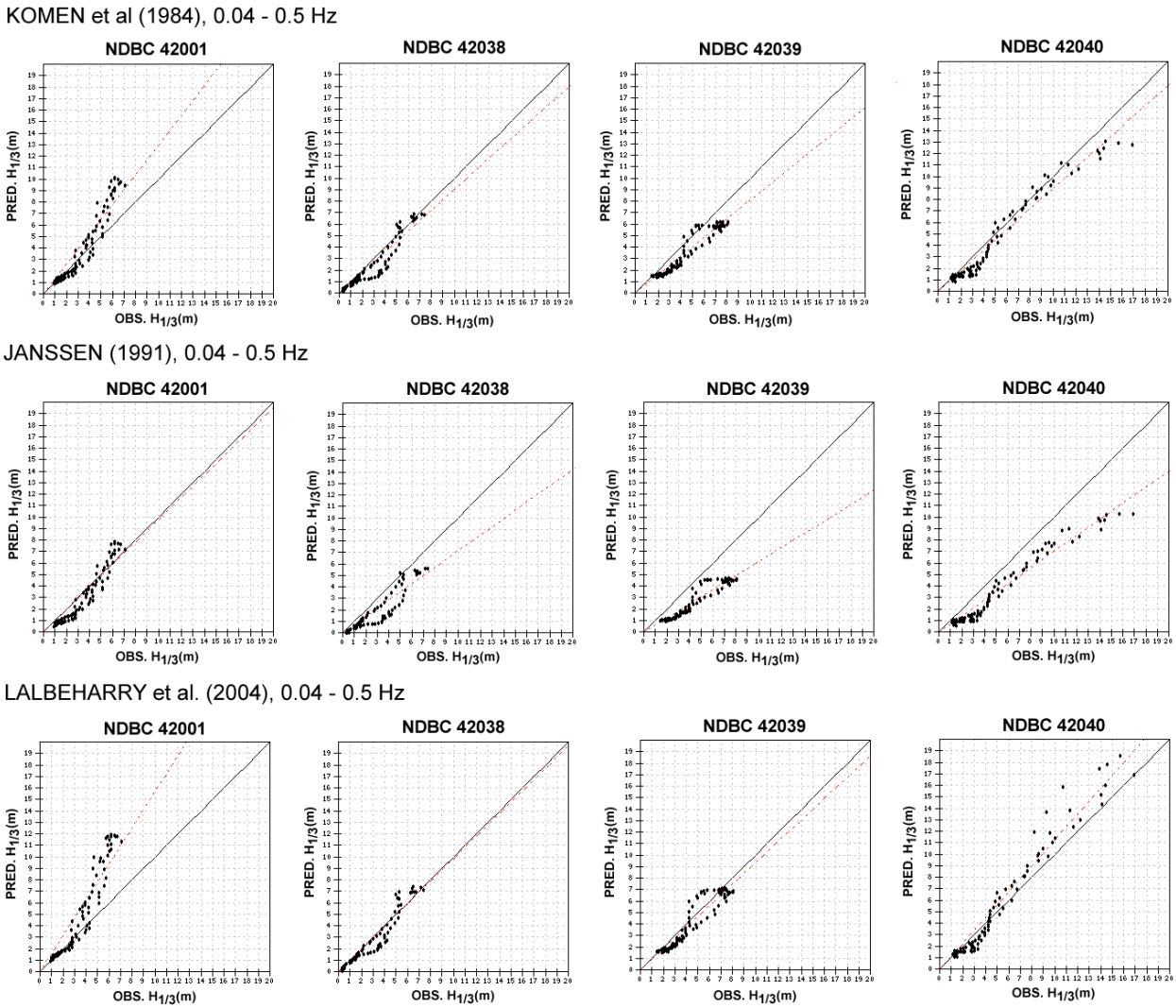

Fig. 4.16 Comparison between observed and predicted significant wave heights using 0.04 – 0.5 Hz frequency range with the wind data of GFS

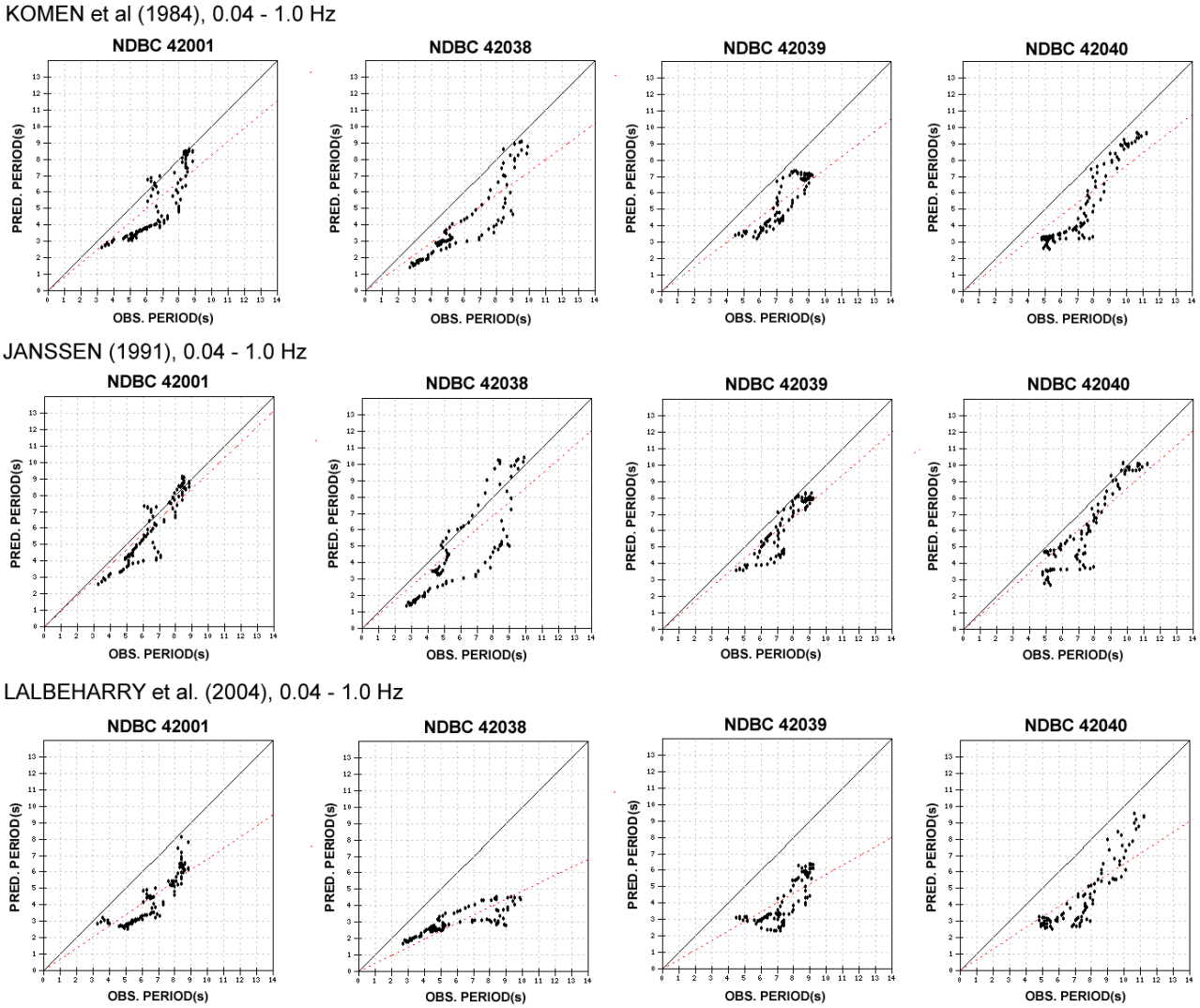

Fig. 4.17 Comparison between observed and predicted mean wave periods using 0.04 – 1.0 Hz frequency range with the wind data of GFS

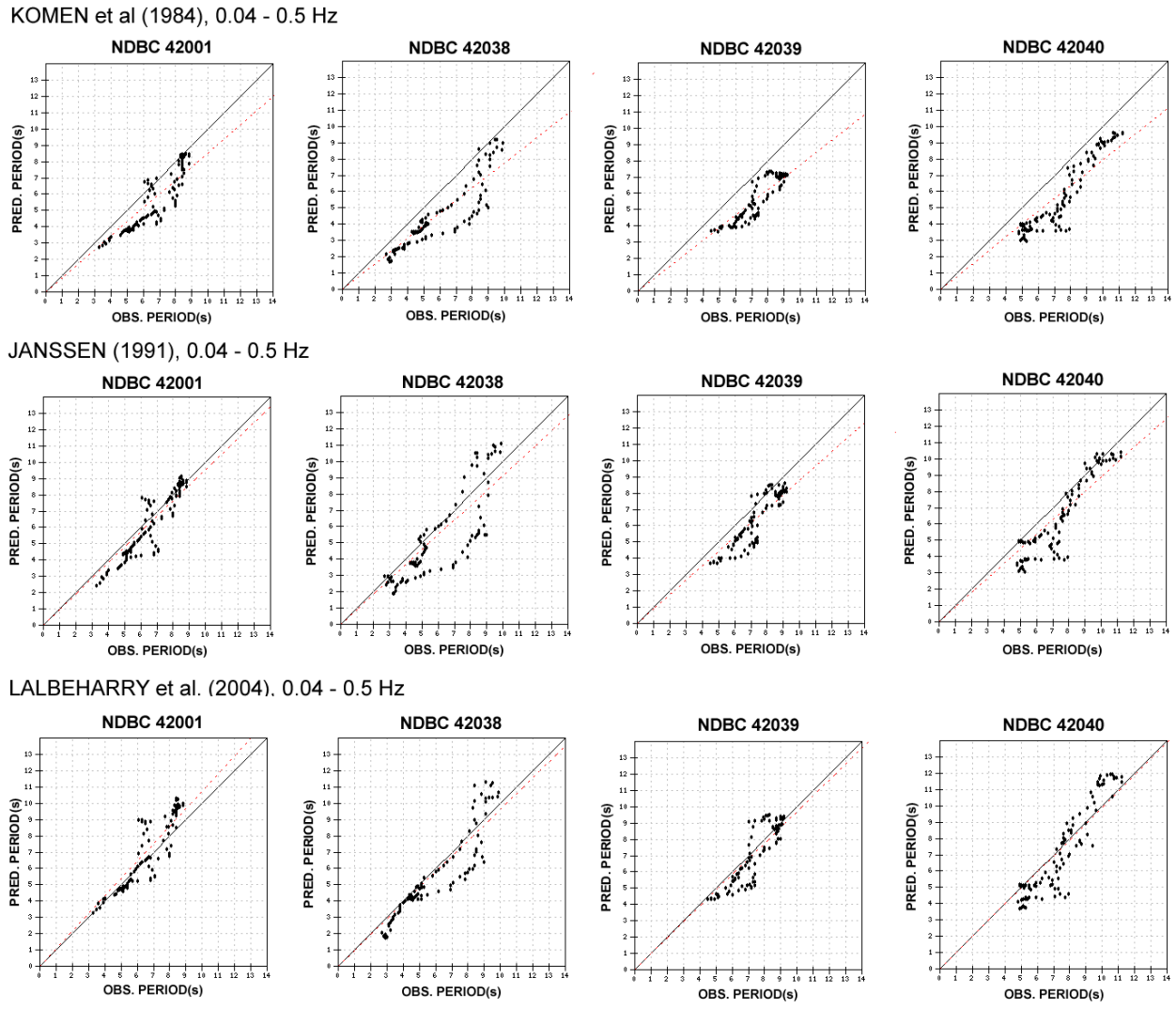

Fig. 4.18 Comparison between observed and predicted mean wave periods using 0.04 – 0.5 Hz frequency range with the wind data of GFS

Table 4.2 NARR, GFS, and FNL wind speed validation statistics

		NARR				GFS				FNL			
St.	**n**	**bias**	**RMSE**	**r**	**s**	**bias**	**RMSE**	**r**	**s**	**bias**	**RMSE**	**r**	**s**
42001 (L)	95	-0.085	2.148	0.923	1.039	0.673	2.105	0.965	0.92	0.605	2.067	0.963	0.925
42002 (L)	96	-0.341	1.224	0.831	1.072	-0.671	1.316	0.848	1.137	-0.65	1.298	0.857	1.139
42003 (R)	30	-1.333	2.126	0.964	1.089	-0.32	2.029	0.942	1.003	-0.55	2.059	0.941	1.015
42019 (L)	95	-0.374	1.351	0.845	1.089	-1.059	1.802	0.804	1.231	-1.059	1.794	0.805	1.236
42020 (L)	94	0.045	1.338	0.71	0.983	-0.532	1.439	0.625	1.161	-0.582	1.464	0.619	1.177
42035 (L)	95	-1.244	2.109	0.828	1.305	-1.179	1.855	0.894	1.318	-1.214	1.88	0.893	1.325
42036 (R)	95	-0.227	1.04	0.855	1.024	0.118	0.826	0.914	0.995	-0.007	0.811	0.918	1.006
42038 (L)	95	-0.295	1.092	0.94	1.046	-0.164	1.115	0.934	1.03	-0.289	1.159	0.933	1.049
42039 (R)	96	0.201	1.287	0.938	0.975	-0.207	1.073	0.94	1.015	-0.372	1.099	0.942	1.028
42040 (R)	96	-0.338	1.898	0.949	1.026	1.124	2.024	0.983	0.902	0.963	1.793	0.983	0.917
42055 (L)	96	0.179	1.827	0.453	0.986	0.078	1.18	0.779	1.013	0.08	1.137	0.796	1.009
Average		-0.35	1.59	0.84	1.06	-0.19	1.52	0.86	1.07	-0.28	1.51	0.88	1.08

Table 4.3 Significant wave height validation statistics using the North American Regional Reanalysis (NARR) 10m wind input

		North American Regional Reanalysis															
		Komen et al. (1984)								Lalbeharry et al. (2004)							
		0.04-1.0 Hz				0.04-0.5 Hz				0.04-1.0 Hz				0.04-0.5 Hz			
St.	n	bias	RMSE	r	s	bias	RMSE	r	s	bias	RMSE	r	s	bias	RMSE	r	s
42001 (L)	95	-0.387	0.597	0.971	1.078	-0.233	0.496	0.971	1.05	-0.697	1.09	0.89	1.184	-0.169	0.452	0.972	1.041
42002 (L)	96	-0.102	0.378	0.943	1.013	-0.087	0.382	0.936	1.017	-0.699	1.017	0.844	2.119	-0.03	0.483	0.91	0.961
42003 (R)	30	-1.977	2.097	0.967	1.418	-1.861	1.986	0.967	1.386	-1.425	1.564	0.954	1.249	-1.627	1.756	0.963	1.319
42019 (L)	95	-0.424	0.742	0.881	1.465	-0.417	0.723	0.911	1.508	-0.823	1.289	0.786	3.124	-0.336	0.554	0.96	1.364
42020 (L)	92	-0.215	0.442	0.929	1.237	-0.198	0.459	0.929	1.271	-0.673	1.116	0.561	2.98	-0.151	0.344	0.955	1.158
42035 (L)	94	-0.288	0.614	0.785	1.24	-0.291	0.555	0.833	1.29	-0.639	0.893	0.88	2.838	-0.154	0.559	0.83	1.032
42036 (R)	94	-1.118	1.185	0.922	1.412	-0.951	1.036	0.914	1.336	-1.651	1.772	0.8	1.818	-0.741	0.841	0.918	1.24
42038 (L)	95	-0.801	1.117	0.926	1.362	-0.702	1.033	0.937	1.338	-1.33	1.76	0.951	2.086	-0.602	0.857	0.959	1.262
42039 (R)	93	-1.33	1.417	0.977	1.344	-1.16	1.264	0.978	1.299	-2.093	2.394	0.848	1.754	-0.886	0.998	0.977	1.207
42040 (R)	96	-1.572	2.122	0.955	1.408	-1.396	2.016	0.956	1.378	-2.354	3.108	0.931	1.83	-1.126	1.743	0.957	1.285
42055 (L)	95	-0.236	0.516	0.844	1.151	-0.239	0.48	0.868	1.183	-0.757	1.01	0.806	2.335	-0.193	0.393	0.916	1.115
Average		-0.77	1.02	0.92	1.28	-0.69	0.95	0.93	1.28	-1.19	1.55	0.84	2.12	-0.55	0.82	0.94	1.18

Table 4.4 Significant wave height validation statistics using the Global Forecasting System (GFS) 10m wind input

		Global Forecast System																							
		Komen et al. (1984)								Janssen (1991)								Lalbeharry et al. (2004)							
		0.04-1.0 Hz				0.04-0.5 Hz				0.04-1.0 Hz				0.04-0.5 Hz				0.04-1.0 Hz				0.04-0.5 Hz			
St.	n	bias	RMSE	r	s	bias	RMSE	r	s	bias	RMSE	r	s	bias	RMSE	r	s	bias	RMSE	r	s	bias	RMSE	r	s
42001 (L)	95	0.535	1.497	0.957	0.773	0.592	1.456	0.957	0.773	-0.495	0.863	0.956	1.057	-0.423	0.864	0.959	1.024	0.44	2.183	0.873	0.735	1.335	2.433	0.952	0.639
42002 (L)	96	0.16	0.788	0.877	0.806	0.146	0.755	0.873	0.822	-0.3	0.581	0.893	1.099	-0.315	0.64	0.879	1.079	-0.685	0.94	0.912	2.006	0.278	1.058	0.823	0.734
42003 (R)	30	-0.996	1.511	0.898	1.126	-0.985	1.499	0.898	1.125	-2.619	2.784	0.897	1.583	-2.324	2.543	0.888	1.443	-1.759	2.183	0.846	1.394	0.243	2.141	0.882	0.888
42019 (L)	95	-0.323	0.518	0.941	1.213	-0.347	0.534	0.942	1.244	-0.579	0.788	0.912	1.556	-0.615	0.818	0.901	1.538	-0.906	1.293	0.952	3.508	-0.338	0.463	0.965	1.21
42020 (L)	92	0.061	0.264	0.978	0.918	0.008	0.235	0.976	0.965	-0.235	0.382	0.954	1.188	-0.229	0.383	0.951	1.144	-0.685	1.091	0.669	2.96	0.18	0.608	0.918	0.804
42035 (L)	94	-0.098	0.572	0.864	0.926	-0.129	0.576	0.853	0.955	-0.269	0.726	0.751	1.055	-0.277	0.754	0.755	1.023	-0.671	0.934	0.837	3.063	-0.045	0.526	0.908	0.879
42036 (R)	94	-0.747	0.875	0.907	1.222	-0.659	0.793	0.908	1.195	-1.395	1.458	0.913	1.58	-1.34	1.403	0.911	1.533	-1.69	1.803	0.782	1.811	-0.267	0.577	0.906	1.055
42038 (L)	95	-0.472	0.823	0.945	1.099	-0.438	0.775	0.948	1.11	-0.998	1.268	0.924	1.438	-0.996	1.238	0.93	1.406	-1.345	1.833	0.928	2.159	-0.233	0.656	0.96	1.018
42039 (R)	93	-1.061	1.249	0.948	1.254	-0.979	1.173	0.951	1.239	-2.002	2.192	0.952	1.707	-1.891	2.066	0.947	1.625	-1.793	1.939	0.939	1.522	-0.413	0.831	0.94	1.072
42040 (R)	96	-0.781	1.124	0.978	1.118	-0.692	1.053	0.979	1.114	-1.884	2.315	0.979	1.521	-1.722	2.068	0.981	1.427	-0.881	1.503	0.961	1.064	0.263	1.272	0.982	0.89
42055 (L)	95	0.088	0.545	0.878	0.886	0.078	0.491	0.881	0.911	-0.351	0.603	0.819	1.245	-0.388	0.621	0.827	1.258	-0.629	0.884	0.759	1.907	0.272	0.728	0.902	0.768
Average		-0.33	0.89	0.92	1.03	-0.31	0.85	0.92	1.04	-1.01	1.27	0.90	1.37	-0.96	1.22	0.90	1.32	-0.96	1.51	0.86	2.01	0.12	1.03	0.92	0.91

Table 4.5 Significant wave height validation statistics using the Final Global Data Assimilation System (FNL) 10m wind input

		Final Global Data Assimilation System															
		Komen et al. (1984)								Lalbeharry et al. (2004)							
		0.04-1.0 Hz				0.04-0.5 Hz				0.04-1.0 Hz				0.04-0.5 Hz			
St.	n	bias	RMSE	r	s	bias	RMSE	r	s	bias	RMSE	r	s	bias	RMSE	r	s
42001 (L)	95	0.492	1.459	0.956	0.781	0.582	1.431	0.956	0.776	0.243	1.954	0.857	0.785	1.044	2.01	0.956	0.688
42002 (L)	96	0.142	0.77	0.879	0.815	0.109	0.744	0.875	0.833	-0.703	0.958	0.939	2.073	0.286	1.112	0.831	0.716
42003 (R)	30	-1.089	1.554	0.908	1.139	-1.049	1.53	0.905	1.134	-1.269	1.991	0.831	1.157	-0.569	1.565	0.894	1.029
42019 (L)	95	-0.338	0.547	0.933	1.224	-0.376	0.576	0.932	1.272	-0.912	1.318	0.901	3.592	-0.32	0.468	0.958	1.183
42020 (L)	92	0.05	0.26	0.977	0.928	-0.007	0.222	0.978	0.98	-0.713	1.098	0.827	3.243	0.185	0.572	0.938	0.798
42035 (L)	94	-0.102	0.579	0.86	0.927	-0.135	0.595	0.852	0.944	-0.631	0.9	0.775	2.671	0.017	0.628	0.894	0.814
42036 (R)	94	-0.79	0.915	0.903	1.239	-0.671	0.799	0.908	1.202	-1.726	1.842	0.792	1.877	-0.359	0.585	0.92	1.084
42038 (L)	95	-0.513	0.854	0.942	1.122	-0.45	0.769	0.949	1.12	-1.358	1.868	0.9	2.176	-0.185	0.795	0.954	0.963
42039 (R)	93	-1.118	1.303	0.946	1.274	-0.993	1.181	0.954	1.247	-1.878	2.048	0.925	1.571	-0.517	0.828	0.951	1.098
42040 (R)	96	-0.872	1.205	0.978	1.147	-0.743	1.106	0.979	1.138	-0.794	1.517	0.961	1.036	-0.006	1.046	0.976	0.952
42055 (L)	95	0.071	0.538	0.876	0.896	0.03	0.469	0.89	0.932	-0.626	0.867	0.841	1.921	0.147	0.651	0.898	0.819
Average		-0.37	0.91	0.92	1.04	-0.34	0.86	0.93	1.05	-0.94	1.49	0.87	2.01	-0.03	0.93	0.92	0.92

Table 4.6 Mean wave period validation statistics using the North American Regional Reanalysis (NARR) 10m wind input

		North American Regional Reanalysis															
		Komen et al. (1984)								Lalbeharry et al. (2004)							
		0.04-1.0 Hz				0.04-0.5 Hz				0.04-1.0 Hz				0.04-0.5 Hz			
St.	n	bias	RMSE	r	s	bias	RMSE	r	s	bias	RMSE	r	s	bias	RMSE	r	s
42001 (L)	95	-1.945	2.111	0.858	1.373	-1.485	1.639	0.889	1.28	-2.975	3.144	0.737	1.777	-0.443	0.826	0.887	1.074
42002 (L)	96	-1.671	1.862	0.887	1.402	-0.844	1.18	0.883	1.187	-2.561	2.895	0.845	2.032	0.462	1.06	0.929	0.897
42003 (R)	30	-2.589	2.647	0.918	1.424	-2.427	2.497	0.912	1.39	-3.648	3.725	0.822	1.719	-1.529	1.624	0.917	1.216
42019 (L)	95	-2.584	2.84	0.773	1.795	-1.555	1.93	0.809	1.41	-3.119	3.588	0.328	2.406	-0.429	0.993	0.887	1.071
42020 (L)	92	-2.966	3.144	0.881	1.837	-1.871	2.166	0.863	1.416	-3.783	4.294	0.491	2.832	-0.528	1.212	0.911	1.053
42035 (L)	94	-2.361	2.859	0.523	1.642	-0.934	1.761	0.521	1.208	-2.983	3.311	0.531	2.408	0.445	1.496	0.642	0.92
42036 (R)	94	-2.268	2.306	0.882	1.482	-1.798	1.84	0.89	1.351	-3.315	3.375	0.662	1.935	-0.639	0.814	0.873	1.096
42038 (L)	95	-2.224	2.44	0.885	1.531	-1.559	1.955	0.85	1.361	-3.129	3.493	0.907	2.152	-0.558	1.061	0.906	1.105
42039 (R)	93	-2.276	2.352	0.911	1.414	-1.845	1.914	0.923	1.322	-3.558	3.685	0.699	1.924	-0.675	0.871	0.923	1.094
42040 (R)	96	-2.484	2.593	0.938	1.423	-1.944	2.089	0.913	1.328	-3.657	3.801	0.879	1.94	-0.712	1.078	0.909	1.097
42055 (L)	95	-2.557	2.819	0.841	1.717	-1.677	2.117	0.798	1.402	-3.439	3.907	0.757	2.501	-0.355	1.192	0.863	1.049
Average		-2.36	2.54	0.85	1.55	-1.63	1.92	0.84	1.33	-3.29	3.57	0.7	2.15	-0.45	1.11	0.88	1.06

Table 4.7 Mean wave period validation statistics using the Global Forecasting System (GFS) 10m wind input

		Global Forecast System																							
		Komen								Jansen (1991)								Lalbeharry et al. (2004)							
		0.04-1.0 Hz				0.04-0.5 Hz				0.04-1.0 Hz				0.04-0.5 Hz				0.04-1.0 Hz				0.04-0.5 Hz			
St.	n	bias	RMSE	r	s	bias	RMSE	r	s	bias	RMSE	r	s	bias	RMSE	r	s	bias	RMSE	r	s	bias	RMSE	r	s
42001 (L)	95	-1.358	1.679	0.867	1.209	-1.079	1.336	0.893	1.167	-0.567	0.997	0.923	1.066	-0.42	0.915	0.919	1.045	-2.278	2.396	0.877	1.475	0.376	1.08	0.894	0.93
42002 (L)	96	-1.225	1.818	0.802	1.201	-0.751	1.471	0.813	1.109	-0.207	1.798	0.9	0.927	0.308	1.807	0.887	0.866	-2.417	2.713	0.858	1.91	0.967	2.281	0.845	0.784
42003 (R)	30	-2.005	2.159	0.809	1.293	-1.938	2.084	0.818	1.282	-1.726	1.864	0.849	1.243	-1.681	1.839	0.838	1.233	-3.943	4.126	0.376	1.851	-1.295	1.628	0.702	1.173
42019 (L)	95	-2.291	2.51	0.845	1.57	-1.602	1.871	0.855	1.369	-1.524	2.294	0.724	1.238	-0.254	1.423	0.88	0.983	-3.204	3.617	0.519	2.481	-0.43	1.015	0.931	1.039
42020 (L)	92	-2.276	2.426	0.933	1.448	-1.066	1.394	0.925	1.165	-0.931	2.066	0.889	1.038	0.595	2.463	0.858	0.829	-3.808	4.271	0.638	2.845	0.836	2.382	0.887	0.81
42035 (L)	94	-1.981	2.516	0.668	1.422	-1.088	1.625	0.767	1.205	-1.055	2.417	0.536	1.117	0.488	1.566	0.781	0.884	-3.074	3.433	0.361	2.528	0.219	1.21	0.897	0.919
42036 (R)	94	-1.918	1.988	0.852	1.372	-1.647	1.71	0.861	1.308	-1.09	1.227	0.888	1.175	-0.909	1.105	0.874	1.138	-3.621	3.689	0.575	2.105	-0.45	0.838	0.864	1.057
42038 (L)	95	-1.905	2.134	0.899	1.375	-1.476	1.757	0.896	1.286	-1.218	1.9	0.836	1.164	-0.795	1.626	0.84	1.093	-3.005	3.379	0.834	2.051	-0.396	1.105	0.915	1.036
42039 (R)	93	-1.956	2.062	0.898	1.334	-1.709	1.798	0.911	1.288	-1.16	1.342	0.913	1.167	-0.977	1.193	0.911	1.135	-3.287	3.395	0.794	1.743	-0.322	0.943	0.883	1.029
42040 (R)	96	-2.039	2.228	0.939	1.299	-1.735	1.895	0.938	1.257	-1.256	1.579	0.922	1.159	-1.021	1.408	0.923	1.12	-2.893	3.027	0.899	1.539	-0.329	1.219	0.929	1.009
42055 (L)	95	-1.909	2.265	0.823	1.405	-1.411	1.878	0.819	1.273	-0.817	1.977	0.781	1.073	-0.216	1.866	0.785	0.977	-3.026	3.418	0.813	2.106	0.399	2.033	0.841	0.875
Average		-1.90	2.17	0.85	1.36	-1.41	1.71	0.86	1.25	-1.05	1.77	0.83	1.12	-0.44	1.56	0.86	1.03	-3.14	3.41	0.69	2.06	-0.04	1.43	0.87	0.97

Table 4.8 Mean wave period validation statistics using the Final Global Data Assimilation System (FNL) 10m wind input

	Final Global Data Assimilation System															
	Komen								Lalbeharry et al. (2004)							
	0.04-1.0 Hz				0.04-0.5 Hz				0.04-1.0 Hz				0.04-0.5 Hz			
n	bias	RMSE	r	s	bias	RMSE	r	s	bias	RMSE	r	s	bias	RMSE	r	s
95	-1.384	1.704	0.862	1.215	-0.924	1.19	0.894	1.142	-2.281	2.467	0.799	1.479	0.552	1.112	0.899	0.911
96	-1.245	1.826	0.8	1.209	-0.391	1.348	0.786	1.048	-2.483	2.758	0.916	1.958	1.305	2.584	0.855	0.742
30	-2.089	2.235	0.819	1.306	-1.945	2.084	0.829	1.283	-3.312	3.439	0.721	1.603	-0.82	1.14	0.842	1.098
95	-2.302	2.536	0.835	1.571	-1.099	1.283	0.934	1.224	-3.224	3.677	0.334	2.51	0.271	1.219	0.96	0.902
92	-2.251	2.408	0.934	1.433	-0.297	1.76	0.824	0.989	-3.871	4.339	0.654	2.938	1.422	2.929	0.875	0.747
94	-1.972	2.511	0.659	1.423	-0.595	1.123	0.864	1.093	-2.966	3.364	0.137	2.403	0.879	1.635	0.887	0.824
94	-1.958	2.027	0.846	1.384	-1.539	1.611	0.861	1.281	-3.398	3.459	0.642	1.977	-0.236	0.731	0.876	1.024
95	-1.888	2.14	0.892	1.365	-1.239	1.601	0.881	1.236	-3.002	3.343	0.846	2.033	0.02	1.331	0.905	0.953
93	-1.995	2.097	0.898	1.344	-1.595	1.691	0.91	1.264	-3.575	3.65	0.832	1.901	-0.11	0.871	0.89	1.001
96	-2.088	2.266	0.937	1.312	-1.619	1.787	0.933	1.239	-3.012	3.107	0.914	1.605	0.007	1.211	0.928	0.968
95	-1.921	2.285	0.817	1.409	-1.118	1.718	0.8	1.206	-3.114	3.525	0.832	2.187	0.605	1.974	0.858	0.857
Average	-1.92	2.19	0.85	1.36	-1.12	1.56	0.87	1.18	-3.11	3.38	0.69	2.05	0.35	1.52	0.89	0.91

4.3.2.5 Summary

The main objectives of this study were to model sea conditions generated by Hurricane Katrina and examine the prediction accuracy when using the different energy transfer models available in SWAN along with different types of wind input and frequency settings. Test case results were validated against observational data from 11 NDBC stations in the Gulf of Mexico.

Evaluation and comparison of each type of wind data were summarized as follows:

- NARR data contains more observational data at a higher resolution than GFS and FNL; however test cases using this wind input showed under-prediction of both significant wave height and mean wave period.
- GFS and FNL wind data produced overall similar results in test cases. The difference between the two datasets corresponds to the amount of observational data used to create a baseline analysis.
- GFS and FNL wind speed during peak wind speed was generally over-predicted. GFS data is slightly larger than FNL data, and NARR data is under-reported during this period.

Evaluation and comparison of each energy transfer model were summarized as follows:

- Komen et al.'s model (1984) provided overall good significant wave heights and mean wave periods for both frequency ranges and each wind data input. Validation statistics showed good correlation coefficient for both wave height and period. Significant wave height bias was generally low however significant wave heights during the peak of the Hurricane were under-predicted. Mean wave periods were generally under-predicted.
- Janssen's model (1991) tended to under-predict significant wave heights and periods. Using the frequency range of 0.04 to 0.5 Hz slightly increased period predictions. Significant wave height during the peak of the hurricane was greatly under-predicted. Mean wave period was under-predicted however showed better results than the Komen et al.'s model (1984).
- Modified Janssen model by Lalbeharry et al. (2004) produced very good significant wave heights and mean wave periods for frequency range of 0.04 to 0.5 Hz. Good correlation coefficient and low error bias were shown in test cases when using the smaller frequency range. During peak wind speeds at NDBC station 42040, the model well estimated the hurricane's peak significant wave height, using the smaller frequency range. Conversely, undesirable results were shown using the frequency range of 0.04 to 1.0 Hz. Modifications by Lalbeharry et al. (2004) shows a calculation dependency on upper frequencies.

Chapter 5 Real-time wave hindcast and forecast

5.1 Introduction

Accurate and timely wave information is vital to the mitigation of disaster prevention management. According to the Ministry of Land, Infrastructure, Transport, and Tourism (MLIT), the three main activities in Japan are: (1) disaster prevention, (2) crisis response, and (3) emergency measures and restoration/ recovery.

Disaster prevention focuses on improving forecasting/warning systems and protecting areas of concern. Threat from high seas and storm surges has prompted great effort to protect coastal areas by building many defense structures such as sea walls and floodgates. High importance is placed on accurate observational and calculated wave data to set design requirements. Protective structures are constructed according to standards based on peak tide level plus the highest known storm surge level produced by Typhoon Vera in 1959. Accurate wave prediction is invaluable to activate disaster evacuation plans and inundation countermeasures. There are ongoing researches to improve wind-wave model source/sink term formulation and model optimization. Real-time prediction is limited to the quality and timeliness of meteorological weather prediction models such as GFS (Global Forecast System) and Hourly Available GPV Atmospheric Analysis.

Disaster crisis response focuses on patrolling areas of concern, reporting damage status, monitoring prediction systems, and delivering warnings. Real-time marine information is essential for meteorologists to assess dangerous ocean conditions and issue warnings.

Disaster emergency measures and recovery focus on emergency restoration measures and implementing post-disaster recovery programs. Historical wave observations in conjunction with calculated wave hindcasts aid in the evaluation of disastrous events as well as the planning, designing, and construction of coastal/marine structures.

Many types of oceanographic observational data are available, such as remote satellite sensing and ship report measurements; however, the most accessible is observational data from buoys. NOWPHAS (Nationwide Ocean Wave information network for Ports and HArbourS) is a network of 61 wave stations (as of 2005) distributed throughout Japan, that provide wave information every ten minutes. The NOWPHAS network of wave gauges are generally situated in areas of high traffic and important harbors. Areas without coverage are left to be estimated from the closest available observational data.

JMA (Japan Meteorological Agency) provides an hourly available GPV (Grid Point Value) atmospheric analysis which is available roughly thirty minutes past each hour. This dataset is calculated using GPV-MSM (Meso-Scale Model) with available observational data, where the main two sources provided by the WINDAS network of Doppler Radar, and the

AMEDAS network of weather stations. The availability of analysis data, only delayed by 30 minutes, creates opportunities to calculate wave hindcast and forecast every hour. Hourly wave prediction can serve as a means to better estimate wave information at locations where observational equipment is not available.

Firstly, this section employs the wind-wave prediction system for both hindcasting and forecasting. Concepts described in Section 2 as well as knowledge gained during verification of both forecasting and hindcasting in Sections 3 and 4 respectfully were utilized to develop and test real-time wave prediction using hourly analyzed atmospheric GPV from JMA.

Secondly, a real-time virtual-buoy system is developed by applying the fore-mentioned concepts of real-time wave prediction using hourly analyzed atmospheric GPV (Grid Point Value). This system conceptually will calculate a hindcast and short term forecast (nowcast) to simulate virtual wave gauges. Allowing wind-wave information to be estimated at locations where actual wave gauge data is unavailable. In addition a graphical picture of the oceans current state can be drawn, since wave information is known at all locations within the computational domain. This virtual buoy system compliments wave instruments by providing current and near future ocean condition estimations at locations where wave observations are unavailable. Archives of hourly wave analysis can be extracted at any location within the computational domain, allowing immediate evaluation of hindcasts. Reducing the time and resources needed to reconstruct and analyze previous events, such as disasters or accidents caused by high wind, wave, and surge.

5.2 Model description

Real-time wave prediction involves employing the wind-wave analysis system to calculate, process, and disseminate wave hindcasts and forecasts every hour. Accurate and timely real-time prediction is accomplished with the following: (1) high speed calculations accomplished through parallel processing, (2) third generation (3G) wind-wave prediction, and (3) high quality input fields such as accurate bathymetry and atmospheric analysis fields. For a description of the wind-wave system refer to Section 2. Accurate hourly calculated wave prediction is attributed not only to the wind-wave model but also to the quality and availability of the wind analysis. This section describes the components and processes of the wind-wave system as employed for real-time wave prediction.

5.2.1 System architecture

The 3G wind-wave model, SWAN, is used to obtain predictions. Third generation models allow the wave spectrum to freely develop without a limit on spectral shape and the resulting spectrum is defined purely from the balance in the source/sink terms. The source/sink mechanisms are defined discretely in the frequency/direction domain, and not formulated by parameterization. These characteristics make predictions by 3G wind-wave models require computational power

Significant advances in computing technology have allowed sophisticated numerical wind-wave modeling to take advantage of the calculation power offered by today's High-Performance Computing (HPC) systems. The real-time prediction system is based on a Beowulf Class I cluster computer system where parallel processing is accomplished with a cluster of commodity personal computers as described in section 2.2.

The system operates 24 hours a day, 7 days a week therefore successful operation of the system requires the following:

- Uninterrupted delivery of atmospheric GPV analysis every hour
- Fault-tolerant system infrastructure of the head node, compute nodes, file servers, network connections
- Large storage area for data archiving
- Fast uninterrupted internet connection

5.2.2 Meteorological wind input

The real-time wind-wave prediction system requires two computational domains. The outer domain is required to model the synoptic scaled events that produce waves with longer frequencies. The inner domain models wave generation, dissipation and propagation on finer scale, especially in coastal areas. The outer domain provides the inner domain with boundary condition wave spectra input.

The outer domain covers an area where hourly atmospheric data analysis is unavailable therefore wind analysis input is provided by the GFS dataset. The GFS dataset is available every six hours, has an initial analysis with 180 hours of forecast with a temporal resolution of three hours, refer to Section 2.3.2.1.

The inner domain uses hourly available atmospheric GPV analysis provided by the Japan Meteorological Agency (JMA). This analysis (HAGPV), covering Japan and nearby seas, is created by assimilating observational data into the meso-scale model (MSM). Observational data include data from wind profilers (WINDAS), surface weather gauges (AMEDAS), aircraft reports (ACARS), and satellites (AMV). Refer to Section 2.3.3.4 for a discussion on HAGPV.

This real-time wind-wave prediction system can be adapted to predict in any area of the world that offers a atmospheric analysis hourly with meso-scale spatial resolution.

5.2.3 Wind-wave model

Wave prediction of the real-time system is calculated by the 3G wind-wave model SWAN wind wave model, used in Chapter 3 for forecasting and Chapter 4 for hindcasting. SWAN computes the evolution of wind waves in coastal regions using the wave action balance equation without any pre assumptions on the wave spectrum shape, described in Section 2.4. Although specifically designed for shallow water coastal applications, the basic calculation philosophy of SWAN is identical to WAM (WAMDI group 1988), and has the ability to calculate predictions on oceanic scales.

5.2.4 Post-processing

Post-processing of calculated results is similar as described in Section 3.2.4. SWAN produces a text file of calculated values which is converted to a binary file format, readable by GrADS. This grads file is then compressed and sent to: (1) archive server, and (2) data processing server.

The archive server stores both hindcast and forecast every hour. The data processing server uses GrADS to produces visual maps of different areas of interest. Once the maps are created, the binary GrADS formatted file, and graphical maps are sent to a web server.

The web server displays animated time sequences of graphical wave analysis. A html based interface allows users to input latitude and longitude values and the web server uses GrADS to extract point data in real-time

5.3 Analysis and verification

5.3.1 Real-time wave prediction using hourly analyzed atmospheric GPV

5.3.1.1 Study overview

This study develops a real-time wave prediction system by using SWAN (Simulating WAves Nearshore) together with 10 meter wind data from "Hourly Available GPV (Grid Point Value) Atmospheric Analysis". Validation of this system was carried out by comparing predictions with observations from NOWPHAS (Nationwide Ocean Wave information network for Ports and HArbourS) wave gauges during the month of December, 2007. The predicted wave heights and periods corresponded well to observed values. This system provides current and near future ocean condition estimations for locations where observational wave data is unavailable.

5.3.1.2 Model setup

5.3.1.2.1 Computational domain

The real-time prediction system requires two computational domains using spherical coordinates: an outer domain covering most of the Northern Pacific Ocean; a nested inner domain covering the seas surrounding Japan. The outer domain provides wave spectra input to the inner domain's boundary.

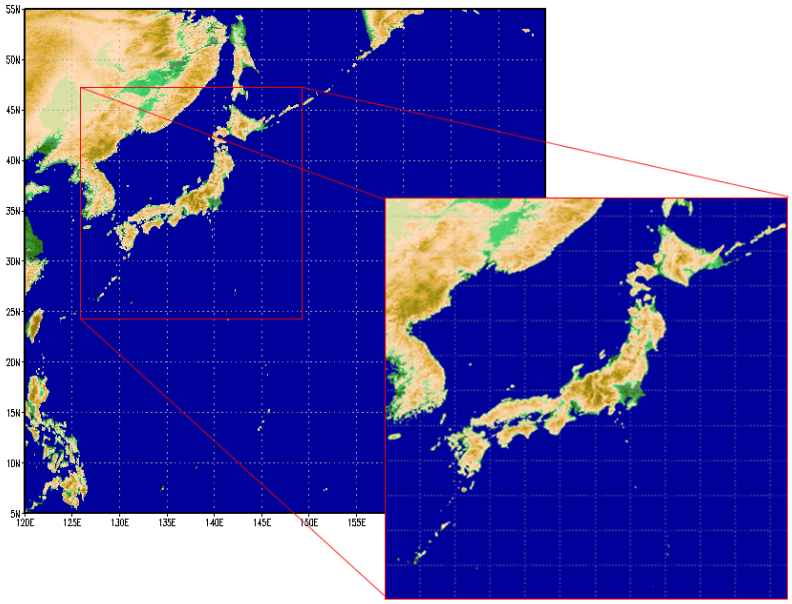

Fig. 5.1 Outer and inner computational domains

Figure 5.1 shows both the inner and outer computational SWAN domains of the real time prediction system. Details specific to each domain are as follows:

1) The outer domain from latitude 5° N to 55° N, and a longitude 120°E to 175°E, a spatial resolution of 0.25°, and a calculation time step of 20 minutes.
2) The inner domain from latitude 24°N to 47°N, and a longitude 126°E to 149°E, a spatial resolution of 0.02°, and a calculation time step of 10 minutes. Bottom friction and depth-induce wave breaking dissipation sink terms activated.

5.3.1.2.2 Wind-wave model

SWAN wind wave model version 40.41 for both domains was set to calculate using a spectral directional resolution of 180° and a frequency range from 0.041 to 0.42 Hz, with 24 frequency bins.

Both computational domains of the real-time prediction system used spherical coordinates with energy transfer formulation by Janssen (1991) modified by Lalbeharry et al. (2004). As shown in Tom et al. (2006), good overall prediction skill was observed in SWAN simulations using the scale independent limiter of Hersbach and Janssen (1999), hereafter referred to as HJ99-limiter. SWAN uses an implicit spatial propagation scheme where the time step is not bound by a CFL-restriction. Two areas of concern of the HJ99-limiter implementation in SWAN were pointed out by Niclasen (2006) and shown in Section 4.3.2. First, the time step size reduces the effects of the HJ99-limiter when needed since it is not bound by a CFL-restriction. Second the fixed cut-off frequency is not sea state dependent as the dynamical cut-off frequency used in WAM (WAMDI 1988) which leads to inconsistent prediction. Therefore, the inner and outer domain in this study used the parameter settings of:

1) spectral directional resolution of 360°, with 18 subdivisions,
2) frequency range from 0.041 to 0.42 Hz, with 25 frequency bins,
3) linear growth term and triad wave-wave interactions are both activated,
4) quadruplet wave-wave interaction is activated by default.

5.3.1.2.3 Meteorological input data

Wind forcing for the two SWAN computational domains are provided by two types of meteorological 10 meter wind data. GFS (Global Forecast System) 10 meter wind data with a spatial resolution of 0.5º is used to force the outer domain. Hourly Available GPV Atmospheric Analysis 10 meter wind data with a spatial resolution of roughly 0.05º is used to force the inner domain.

The 0.5 degree GFS data was received four times a day and contained an analysis dataset with forecast out to 72 hours with a three hour temporal resolution. Ideally a dataset that consist of only analysis data was preferred but forecast data was utilized since the outer domain covers an area where no real time analysis data is available. For more discussion on GFS refer to Section 2.2.2.1.

The Hourly Atmospheric Analysis GPV dataset (HAGPV) is a data grid that includes 17 levels of wind and temperature analysis provided every hour by JMA. The data grid covers an area between 22.4 to 47.6 degrees latitude and 120 to 150 longitude with a spatial resolution of 0.05º by 0.0625º degrees (481 x 505 grid points) respectively.

The dataset is produced by assimilating atmospheric observations into the GPV-MSM weather model to produce an analysis dataset. Wind observations are from WINDAS (Wind Profiler Network and Data Acquisition System), ACARS (Aircraft Communications Addressing and Reporting System), Satellite AMV (Atmospheric Motion Vector), and AMeDAS (Automated Meteorological Data Acquisition System). Temperature observations are obtained from ACARS and AMeDAS. For a discussion on HAGPV refer to Section 2.2.3.3.

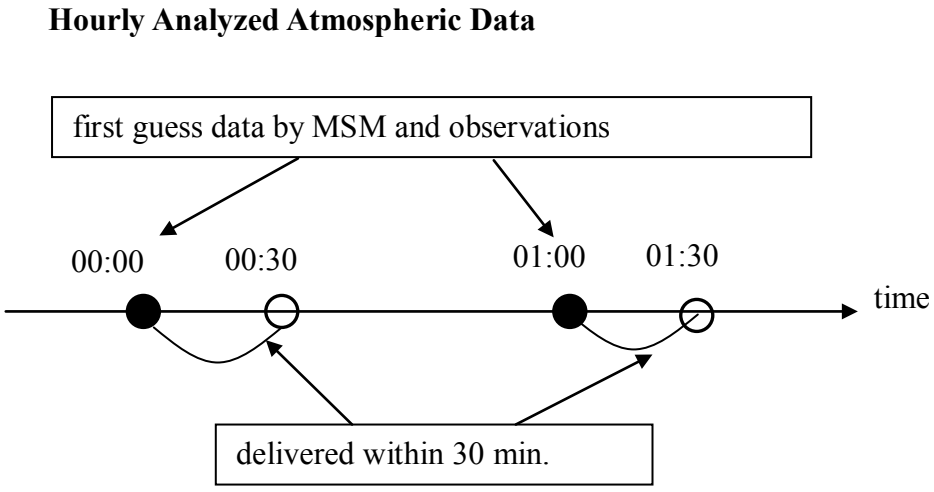

Fig. 5.2 Processing and delivery schedule of the hourly analyzed GPV atmospheric dataset

The HAGPV dataset is calculated 20 minutes after the hour and delivered 30 minutes after the hour. In figure 5.2, WINDAS and AMEDAS observational data for 00:00 is collected assimilated into the GPV-MSM model, calculating at 00:20 and delivered by 00:30. Similarly in Figure 5.2, observational data for 01:00 is collected and distributed by 01:30.

5.3.1.2.4 Bathymetric data

Bathymetric input for both computational domains are extracted from two different sources. Each domain uses data that is roughly similar in spatial resolutions, where the spatial resolutions of the inner and outer domain are 0.25° and 0.02° respectively.

The outer domain used 10 minutes' bathymetric data provided by the Digital Bathymetric Data Base Variable resolution (DBDBV) from Naval Oceanographic Office (NAVOCEANO). The DBDBV was developed to provide bathymetric data for ocean modeling.

The inner domain used bathymetric data provided by the ETOPO2v2 from NOAA/NGDC. ETOPO2v2 is based on satellite altimetry and contains a spatial resolution of two minutes where one minute of latitude is equal to 1.853 km at the Equator. ETOPO2v2 was released in 2006 and has many improvements over the earlier version released in 2001.

5.3.1.2.5 Process flow

The entire process cycle from start to finish basically involves calculating one hour of hindcast and one hour of forecast. Each process cycle is executed once every hour as new HAGPV analysis is received (half past the hour).

There are four steps in the entire process cycle:

1) Process outer domain forecast for step (2) boundary condition input;
2) Process inner domain hindcast;
3) Process outer domain forecast for step (4) boundary condition input; and
4) Process inner domain for forecast.

Each processing step requires three types of input data: 10m wind, initial condition, and bathymetry. Additionally, processing for the inter domains require a file containing boundary input. Each step has two types of output: initial condition for next hour, and statistical ocean parameters for the hour in question.

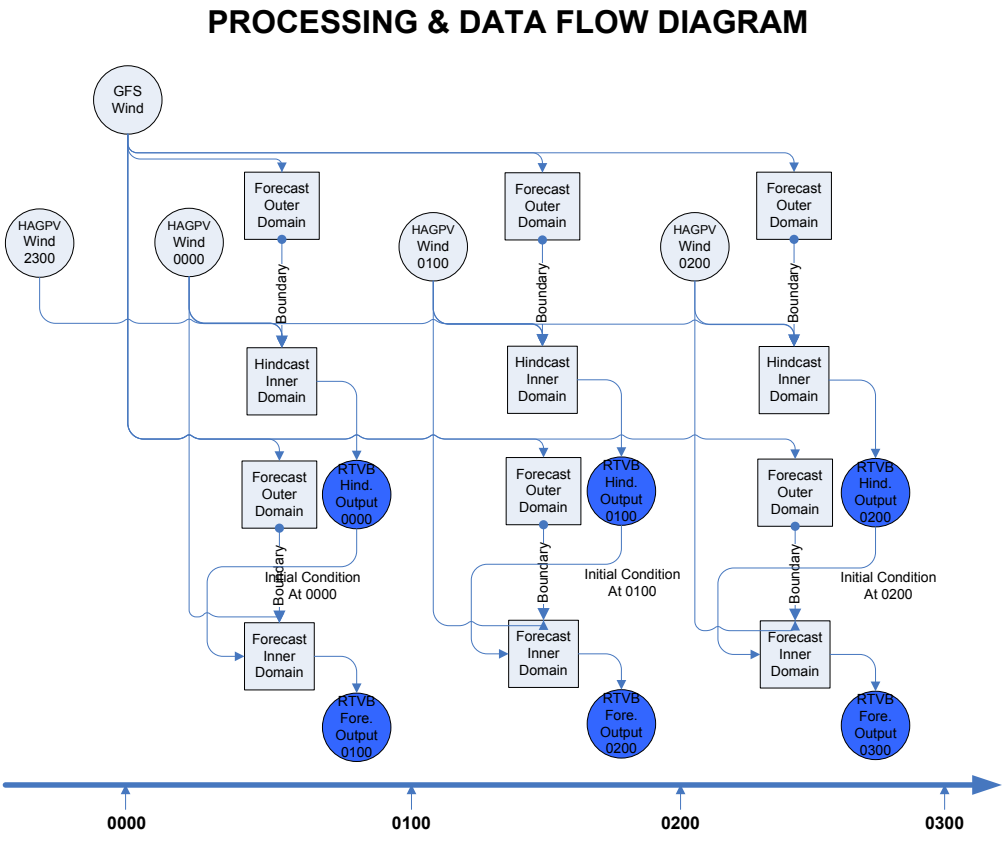

Fig. 5.3 Processing and data flow diagram of the hourly hindcast and forecast cycle

Figure 5.3 shows the processing and data flow of three process cycles. The first cycle is for the data hour 0000 and starts at roughly 0030, the second cycle is for the data hour 0100 and starts roughly at 0130, and the third cycle for the data hour 0200 and starts roughly at 0230.

The process cycle for the hour 0100, starts with the processing a forecast of outer domain for the inner domain hindcast. Input for this step includes: (1) GFS 10m wind data for the hours 0000 and 0100, (2) Initial condition file from the previous processing cycle at 0000, and (3) 10 minute DBDBV bathymetric data. Output for this step includes: (1) Initial condition for 0100 to be used during the next processing cycle, (2) Boundary file for the inner domain during the second step (3) Statistical ocean parameter data for 0100.

The second step processes a hindcast of inner domain. Input for this step includes: (1) HAGPV 10m wind data for the hours 0000 and 0100, (2) Initial condition file from the previous processing cycle at 0000, (3) Boundary file from the first processing step, "Forecast Outer Domain", and (4) Two minute ETOPO2v2 bathymetric data. Output for this step includes: (1) Initial condition for 0100 to be used during the next processing cycle (2) Statistical ocean parameter data for 0100.

The third step processes a forecast of outer domain for the inner domain. This step is a repeat of the first step but now the forecast for the hour 0200 is calculated. Input for this step includes: (1) GFS 10m wind data for the hours 0100 and 0200, (2) Initial condition file from step one, and (3) 10 minute DBDBV bathymetric data. Output for this step includes: (1) Initial condition for 0200 to be used during the next processing cycle, (2) Boundary file for the inner domain during the step four and (3) Statistical ocean parameter data for 0200.

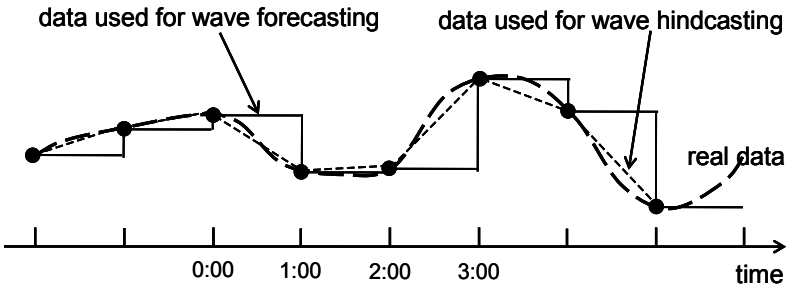

Fig. 5.4 10 m wind data used for both hindcast and forecast calculations

The fourth and final step processes a forecast of the inner domain for 0200. Input for this step includes: (1) HAGPV 10m wind data for the hour 0100 where wind input data is set to constant, (2) Initial condition of 0100 produced at step two, (3) Boundary file from processing step three, and (4) Two minute ETOPO2v2 bathymetric data. Output consists of only one type of data which is the statistical ocean parameter data for 0200. Figure 5.4 shows the data used for both hindcast and forecast calculations.

5.3.1.3 Observational data from NOWPHAS

Observation data from five NOWPHAS wave meters were obtained to compare with hindcasted and forecasted values of significant wave height (H_s) and mean wave period (T_{m01}) for the test duration of December 1st through 31st 2007. Wave gauges approximated to the open sea selected for comparison were: Kanazawa, Mutsuogawara, Tokachi, Tottori, and Wajima. Table 5.1 lists wave gauge locations, sensor depth gauge type.

Selected NOWPHAS locations use the Doppler Type Wave Directional Meter (DWDM), current-meter type wave directional meter (CWD), or an Ultra-sonic wave meter (UWD). Three types of meters are installed on the sea floor. The DWDM detects three components of water particle motion by applying the Doppler Principal. The method of obtaining the directional spectra from tri-dimensional water particle motion was developed by PARI (Takayama et al. 1994 and Hashimoto et al. 1996). CWD detects two components of horizontal water particle motion and dynamic pressure fluctuation due to wave action. The USW detects sea surface movement from wave action by using ultra-sonic waves.

Table 5.1 NOWPHAS wave gauge details

Location	Position	Depth(Sensor bot)	Meter Type
Kanazawa	36-36-39N, 136-34-13E	-20.2m (0.5m)	Ultra-sonic wave
Mutsuogawara	40-55-20N 141-25-40E	-9.0m (0.9m)	Current meter type directional
Tokachi	42-38-57N 143-41-22E	-23.0m (1.0m)	Doppler type directional
Tottori	35-33-05N, 134-09-51E	-30m (0.5m)	Doppler type directional
Wajima	37-25-40N 136-54-19E	-50.0m (0.8m)	Doppler type directional

5.3.1.4 Performance evaluation

Figure 5.5 show the comparison of wave forecast and observation time series for a one month period at five NOWPAHS buoy locations where significant wave comparisons on the left hand side and mean wave period comparisons on the right hand side. It must be noted that the forecasted result of significant wave period is determined by the zeroth- and first-order moments of the highest third of the spectral distribution. Whereas, the observation value is determined from the zero-up-crossing method (time series analysis). Therefore, it is expected that forecasted wave periods are generally smaller when compared to NOWPHAS observations. Overall, the forecasted wave height results displayed very good performance throughout the test period. A general tendency to under-predict wave heights during times of high seas was shown at most points except at Tottori where times of high seas showed over-predicted wave heights.

Wave period prediction is generally under predicted as described by ($T_{1/3}$=1.2T_m; Honda and Hicaeki, 1978); the difference of the forecast value and the observation value is expected. Under prediction is especially evident at Tokachi and Mutsuogawara.

Figures 5.6 and 5.7 show the correlation between predicted and observed values of significant wave height and wave period, respectively. Prediction is represented in the horizontal axis and observation in the vertical axis. The correlation coefficient (C.C.) is indicated in each figure. It is understood that the correspondence of wave height prediction to observation is overall good, with scores above 0.89 at all test locations. Wave period correspondence coefficient is poor at Tokachi; however, good overall at other test locations.

In Section 3.3.2, Three season study of GFS-WRF-SWAN forecast system, it was shown that forecasts by SWAN were generally under-predicted. Section 4.3.2, Analysis of high waves generated by Hurricane Katrina, showed wave prediction was improved using the Janssen (1991) energy transfer formulation, as modified by Lalbeharry et al. (2004). This study showed improved general forecast accuracy over results obtained in Section 4.3.2 greatly due to the improvement of wind forcing provided by HAGPV wind fields. Four factors that contributed to the improvement of HAGPV wind data were:

- Increase in temporal resolution. Section 4.3.2 compared prediction results using GFS and FNL datasets. GFS and FNL datasets showed good performance with FNL showing slightly better performance. FNL and GFS use the same forecast model with FNL containing more observational data in its analysis of initial condition's input data. These analysis datasets have a temporal resolution of six hours which did not resolve the quick increases in wind speeds. This study used HAGPV, hourly available GPV atmospheric analysis data, which was available approximately 30 minutes past each hour. The temporal resolution of one hour better depicts the quick changes of wind speed, especially during typhoons and other fast moving pressure systems.
- Increase in spatial resolution. GFS and FNL are synoptic datasets with spatial resolutions of approximately 100 km, whereas the hourly GPV atmospheric analysis is a meso-scale dataset with a spatial resolution of 5 km. The meso-scale resolution allows small pressure systems to be included in the calculation of local wind swells, improving the overall forecast.
- Increase in observational data. The hourly GPV atmospheric analysis data is produced using JMA-MSM with data assimilation from observational data obtained by the WINDAS and AMEDAS networks. The WINDAS network of Doppler radars a provide grid of atmospheric data for the general areas over and around Japan and the AMEDAS network of weather stations provide surface data for selected points throughout Japan. This coverage allows the JMA-MSM to produce an analysis grid comprised mostly of observational data.
- Increase in calculation time step. Improvement of period values in this study is also attributed to the computational time step used in the inner domain. Niclasen (2006) showed the HF99-limiter when implemented in SWAN, is influenced by the calculation

time step due to the HJ99-limiter not being bound by a CFL-restriction. Niclasen (2006) found wave height prediction is best with a time step of 20 minutes and wave period prediction improve as the time step is decreased. A time step of 10 minutes economically gives good wave height and period values.

Forecast by SWAN during the test period showed good ability to predict wave height and period one hour into the near future. Forecast using the hindcasted wave fields as initial condition input with constant wind forcing showed to be comparable to predicted hindcast. Using wave fields from the hindcast calculation as initial input condition for the forecast calculation greatly improved prediction results and shows the importance of accurate initial condition setup and initial wind forcing.

5.3.1.5 Summary

The real-time wave prediction system presented in this section utilizes the hourly available GPV atmospheric analysis to calculate a highly accurate forecast system that predicts ocean statistical parameters in real time. Hindcast of the previous hour and a forecast of the fore-coming hour were calculated every hour as GPV atmospheric data arrived.

NOWPHAS wave gauge instruments provide the main source of current ocean condition information with the greatest limitation being the location and number of instruments available. Accurate prediction by this real-time system can provide mariners information where wave gauge instruments do not cover.

Hindcast are normally calculated to show ocean conditions during past events, typically after disastrous events involving high surf and surge. The computational domain of this system encompasses the seas surrounding Japan eliminating the need to calculate hindcast for special locations, therefore allowing quicker analysis of any event occurring in the seas surrounding Japan.

Calculated results were compared with data from six NOWPHAS buoy points located at positions open to the sea and evaluated for accuracy. It was shown that both calculated hindcast and forecast showed a high degree of accuracy. The improvement of wave prediction shown through this test is attributed to three factors: (1) increase in temporal resolution of wind input to one hour, (2) increase in spatial resolution to two kilometers and, (3) increase in observational data assimilated into the wind analysis.

Although the results presented here are encouraging, further examination of this system is needed to test model performance during high wind and sea conditions, especially during the typhoon season in Japan. These typhoon strength winds rapidly change within a short time span and greatly affect the ability of the wave model to calculate wave growth and dissipation.

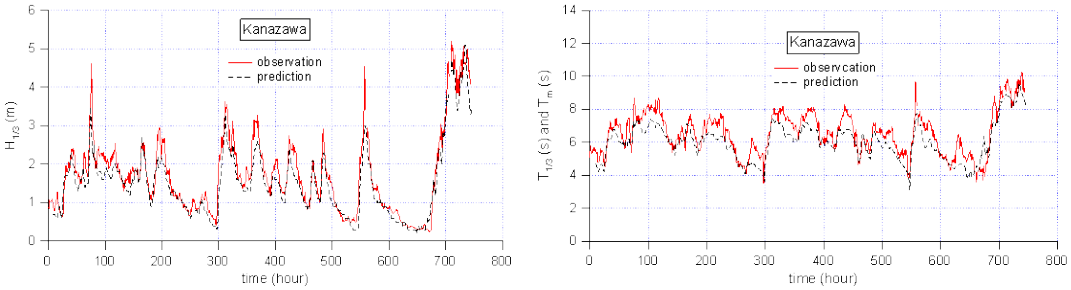

(a) Kanazawa

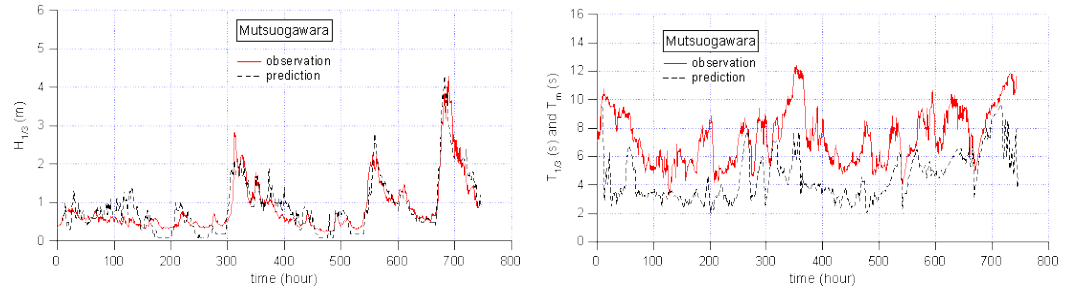

(a) Mutsuogawara

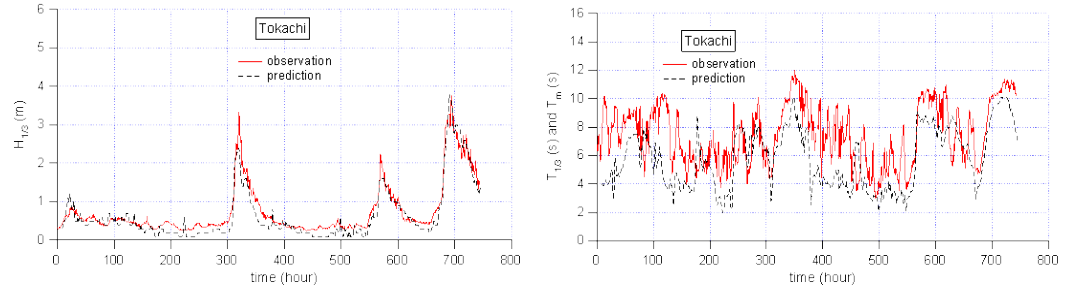

(a) Tokachi

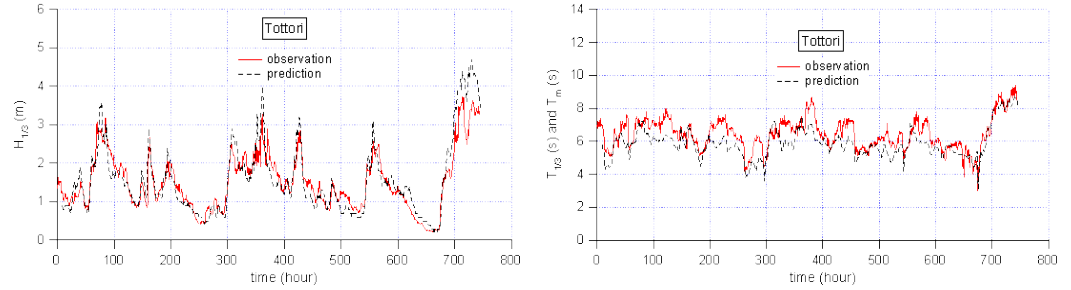

(a) Tottori

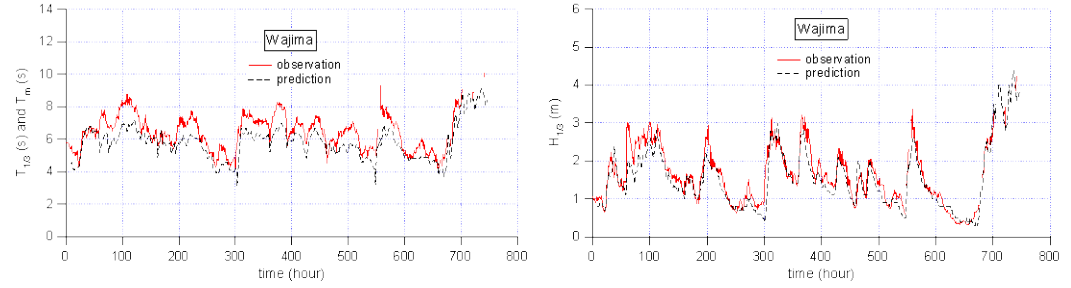

(a) Wajima

Fig. 5.5 Significant wave height and mean wave period time series of predicted and observed values

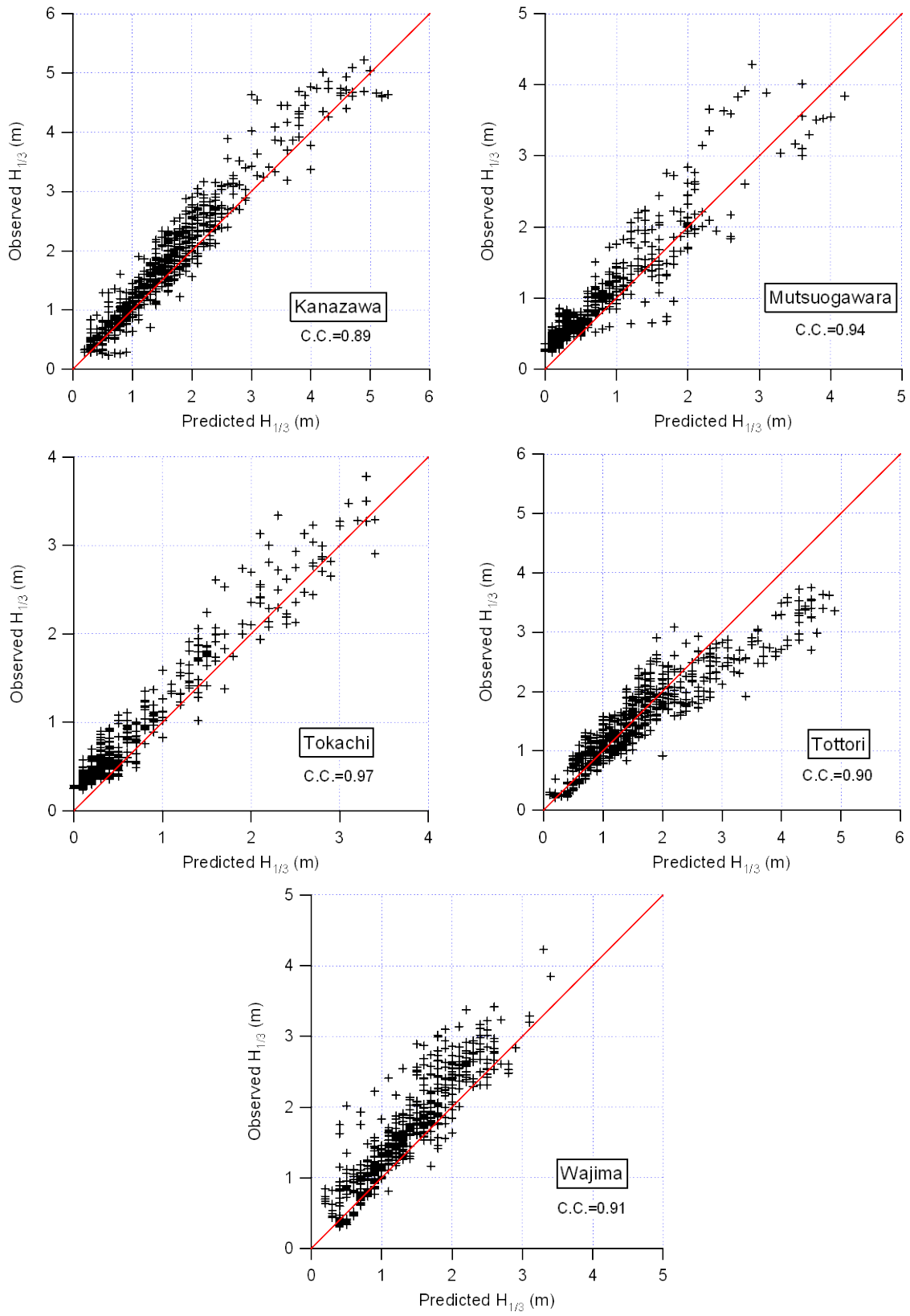

Fig. 5.6 Comparison of predicted vs. observed wave heights

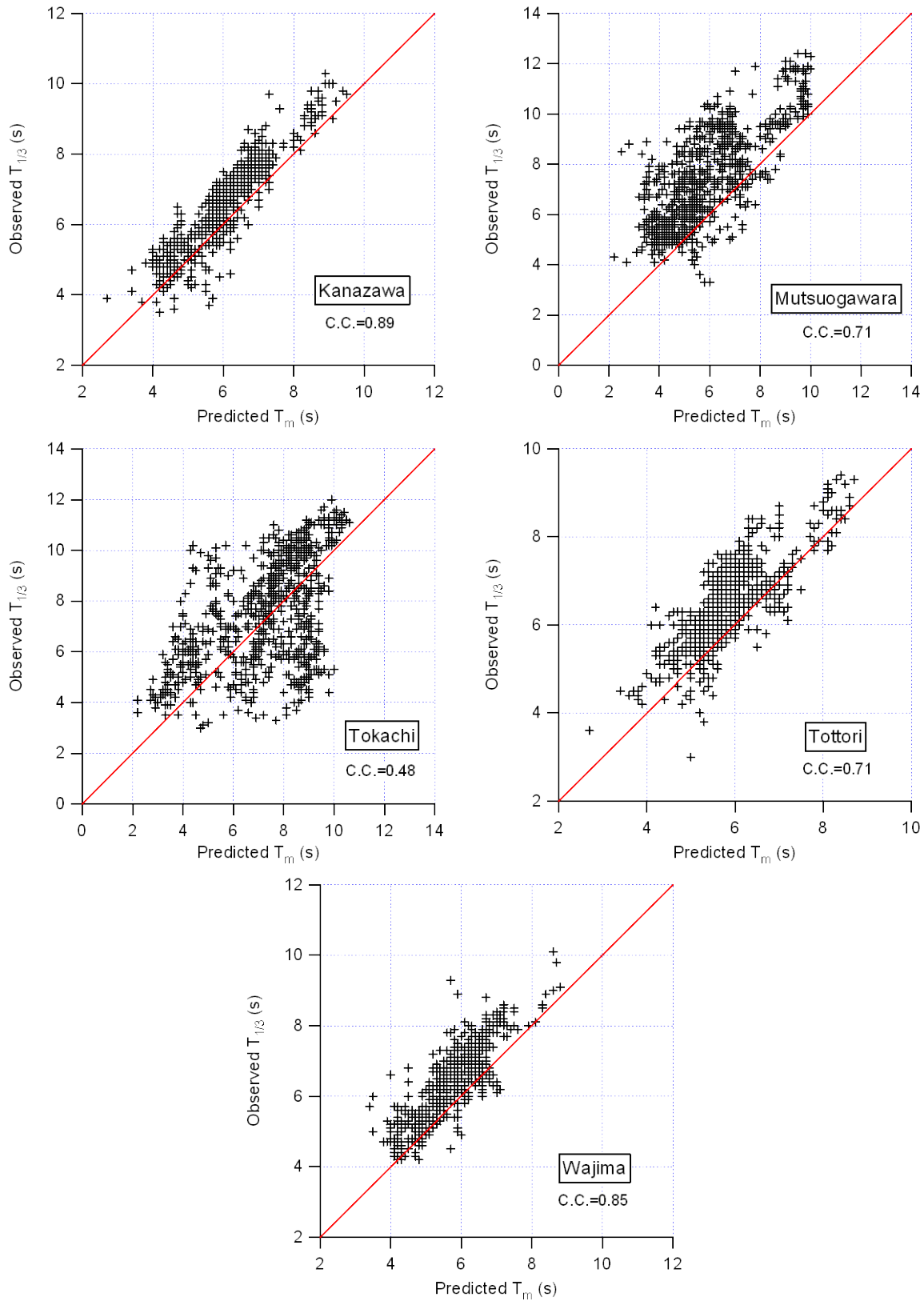

Fig. 5.7 Comparison of predicted vs. observed wave periods

5.3.2 Development of a virtual buoy system using real-time wave Prediction

Threat from high waves and storm surge has always existed and continues to pose a threat to life and property. The coastal areas are threatened especially during the typhoon season from May through October, with the higher occurrences in August and September. High wind and rough seas are common along the coastal areas along the Sea of Japan, during the winter season. A network of wave gauges exist throughout Japan but coverage is limited to areas of high traffic such as ports and harbors, leaving other areas uncovered.

Building on the results obtained in testing the real-time wave prediction system, this section presents the development of a virtual buoy system. The system utilizes the latest advances in technology to enable hourly calculation and data distribution of wave prediction: (1) hourly available GPV atmospheric analysis, (2) spectral wave modeling, (3) Beowulf high performance cluster (HPC) computing, (4) internet connectivity, and (5) web and mobile access.

Hourly available GPV atmospheric analysis provides the SWAN wave model with 10 meter wind data that has shown to improve wave prediction, refer to Section 5.3.1. Data availability is a key factor that enables the concept of calculating wave prediction every hour. Advances in wave modeling have enabled quicker calculation of wave prediction through the use of parallel processing and improved prediction accuracy through research and study shown in Section 3.3.2.

Predicted wave estimation information is delivered through to a wide audience, two methods of accessing the calculated results of the real-time virtual buoy system is available: (1) mobile internet access, and (2) personal computer access. Internet connectivity has allowed data to be exchanged worldwide, quickly, and freely. Web and mobile access of data allows end users to conveniently view data.

This virtual buoy system allows access to wave prediction data through a web mashup, refer to Section 5.3.2.7. The main goal of this system is to: (1) provide wave information estimations at locations where wave observation is unavailable, and (2) provide historical wave analysis data for immediate hindcast evaluation of the seas surrounding Japan.

5.3.2.1 Real-time wave information from instruments

Many types of oceanographic observational data are available, such as remote satellite sensing and ship report measurements, but the most accessible and utilized is observational data from NOWPHAS wave gauges. NOWPHAS (The Nationwide Ocean Wave information network for Ports and HArbourS) is a network of 55 wave stations (as of 2003) distributed throughout Japan, that provide wave information every ten minutes. The main type of meter

used is the Doppler-type Wave Directional Meter (DWDM, Hashimoto et al. 1996). The DWDM obtains directional spectra from the tri-dimensional water particle motion, by applying the Doppler Principle of the acoustic signal. Wave gauges are limited to areas of high importance or usage such as ports and harbors. Wave information of areas where gauges do not exist, are left to be interpolated or hindcasted by a wind-wave model.

5.3.2.2 Real-time wave prediction using hourly available atmospheric GPV analysis

Real-time wave prediction is accomplished by calculating wave characteristics using SWAN, a third-generation wave model developed by Delft University of Technology with wind input from the hourly available atmospheric GPV analysis from the Japan Meteorological Agency (JMA). This section briefly describes the SWAN domain setup, wind input, and process flow used to produce the real-time wave prediction hourly, refer to section 5.3.1, Real-time wave prediction using hourly analyzed atmospheric GPV.

5.3.2.3 Domain setup

The real-time wave prediction is produced using SWAN setup two domains. The outer domain covers most of the Northern Pacific Ocean (latitude 5° N to 55° N, and a longitude 120°E to 175°E) with a spatial resolution of 0.25°. The nested inner domain covers the seas surrounding Japan (latitude 24°N to 47°N, and a longitude 126°E to 149°E) with a spatial resolution of 0.02°. The outer and inner domain uses bathymetry with spatial resolutions of 10 minutes and 2 minutes respectively. Figure 1 shows the outer and inner domains.

5.3.2.4 Wind input

The Per Hour GPV Atmospheric Analysis, produced by JMA, is a numerical analysis of the horizontal wind and temperature fields of Japan and surrounding areas. The dataset contains wind and temperature fields for 17 atmospheric levels, including 10 m wind and 1.5 m temperature data at the surface. The data grid covers an area between 22.4 to 47.6 degrees latitude and 120 to 150 longitude with a spatial resolution of 0.05 degrees by 0.0625 degrees (481 x 505 grid points). Assimilated wind observations are from WINDAS, ACARS, Satellite AMV, and AMeDAS. Temperature observations are obtained from ACARS and AMeDAS. Data is collected from all sources up until 20 minutes past the hour at which time the data set is assimilated into the JMA GPV-MSM, then distributed by 30 minutes past the hour.

5.3.2.5 Process flow

The entire process cycle from start to finish executed once every hour as new GPV-QMA analysis data is received (half past the hour). There are four steps in the entire process cycle:

1) Process outer domain forecast for step (2) boundary condition input;
2) Process inner domain hindcast;
3) Process outer domain forecast for step (4) boundary condition input; and
4) Process inner domain for forecast.

Each step has two types of output: Initial condition for next processing cycle (next hour), and statistical ocean parameters. Wind input for the inner domain hindcast consists of the previous and current hour GPV-QMA 10m wind data whereas the wind input for the inner domain only consist of the current hour GPV-QMA 10m wind data set to constant. Figure 3 shows the real-time wave prediction processing and data flow cycles.

5.3.2.6 Data Flow

A processing cycle of the real-time virtual buoy system consists of four steps as shown in Figure 5.8. Each cycle is performed hourly upon arrival of the GPV atmospheric analysis data. The first step involves downloading the GFS 0.5 degree data from the NCEP server. This download is performed four times a day at 0000, 0600, 1200, and 1800 UTC. The hourly available GPV atmospheric analysis data is sent to the HPC half past each hour. Upon reception, the analysis data is formatted for input into the SWAN model. The second step is the heart of the system and involves calculating the wave incest and forecast as described in Section 3 (Real-time wave prediction using hourly available atmospheric GPV analysis). The third step involves converting the SWAN data into a GrADS formatted binary file and drawing graphical maps of the inner domain as shown in Figure 4. The final step involves sending the wave prediction data to the distribution/web server and archive server.

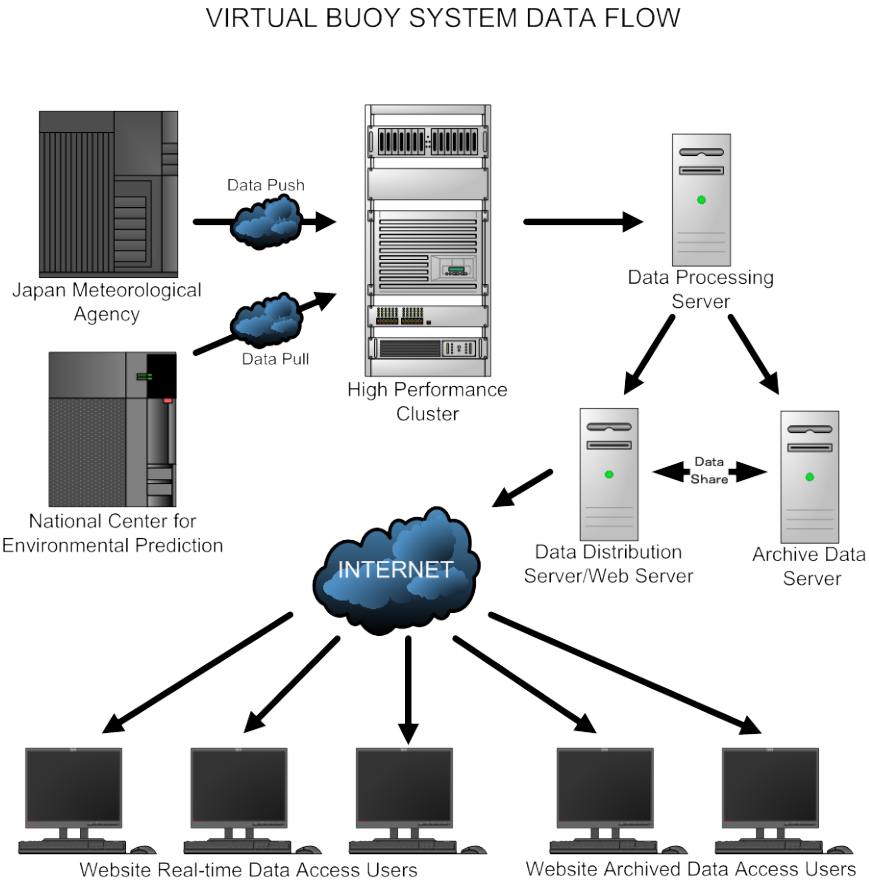

Fig. 5.8 Data flow of the real-time and archive wave prediction application

5.3.2.7 Real-time virtual buoy mashup

The real-time virtual buoy mashup allows graphical access to grid point data through a web browser interface. A mashup is a web application that combines data from many sources into a unified tool. This mashup employs the Google Maps API to provide the user with a visual method to select latitude and longitude coordinates. A map of Japan is graphically displayed upon starting the mashup as shown in Figure 5.9. The user is allowed to either use the Google Maps control functions (① through ④) or manually enter the latitude and longitude of the desired data point (⑤). The following is a brief discussion of the overall map control:

① Navigation controls allowing up, down, left, and right map movement
② Scale controls allowing zooming in and out
③ View controls allowing the map to be displayed in map mode (street map), Satellite mode (satellite imagery), or Hybrid mode (combination of map and satellite).
④ Slider tool allowing quick movement. Clicking down on the inner box and dragging will move the display map similarly
⑤ Manual latitude and longitude input

In addition to the control functions the user is allowed to click anywhere on the map and drag in the opposite direction of the desired map motion.

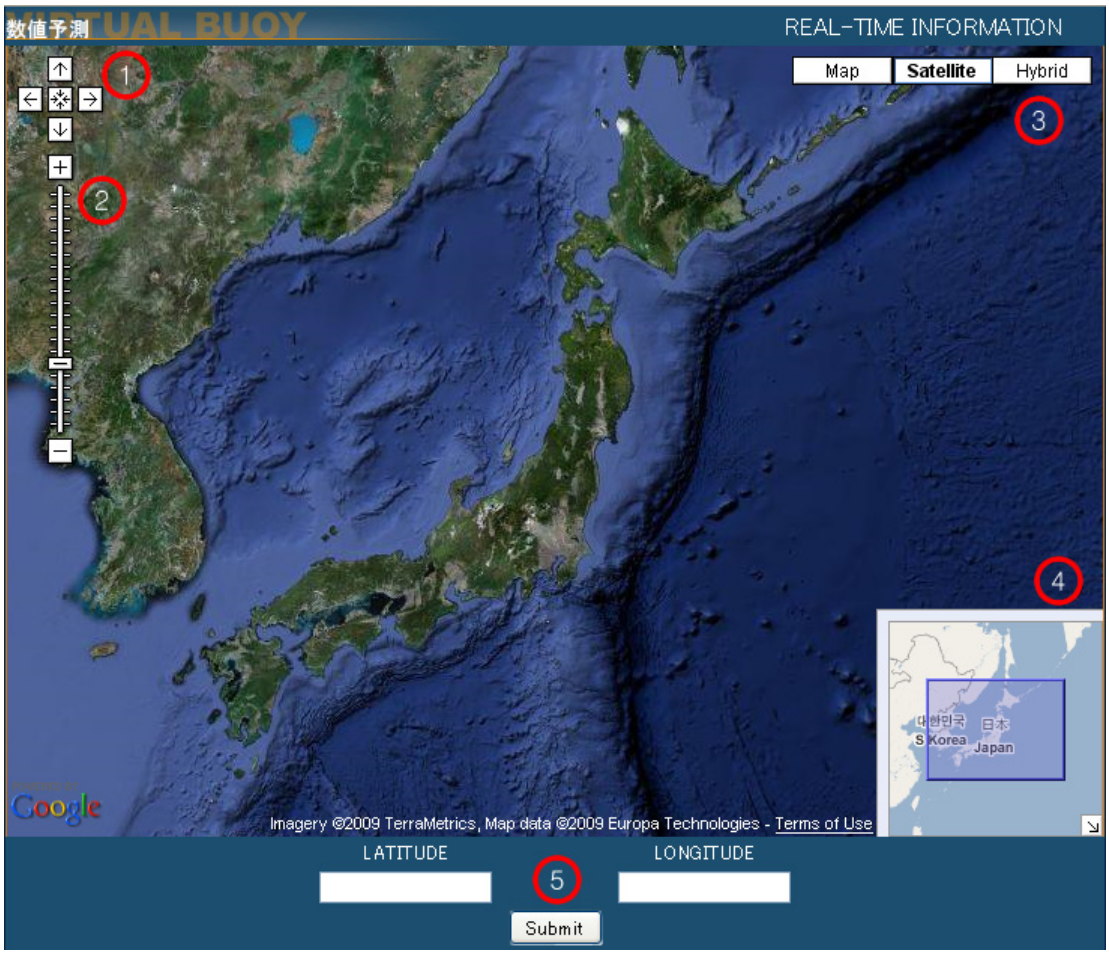

Fig. 5.9 Real-time virtual buoy mashup

Sliding control function number ② in the upward direction zooms the map into an area showing finer detail. Figure 5.10 shows the mashup zoomed into the Kiisuido area. The locations of four NOWPHAS wave gauges are shown in yellow dots, and clicking on the area indicated by the red arrow will return the graphical graph and text data output as shown on the right of Figure 5.11. The four graphs in Figure 5.11 show data extracted at the selected point. Respectively the data fields are: (1) wind and wave direction, where red denotes wave data and blue denotes wind data, (2) wind speed, (3) significant wave height, (4) mean wave period hindcast and forecast, where red denotes hindcast and green denotes forecast.

Google map serves as the general GIS to return the latitude and longitude of the desired point. A system process that retrieves the requested data is called once the user selects a point by clicking on a location or clicking select. Data returned is dependent on the data stored in the immediate file history folder. The data shown in Figure 5.11 was requested on 2/26/2009 at 1955 JST and includes data from 2/24/2009, 2000 JST through 2/26/2009, 2100 JST where the most current hindcast and forecast are shown on the right side of the graphs. The most recent hindcast is 2/26/2009, 1900 JST with forecasts for 2000 and 2100 JST.

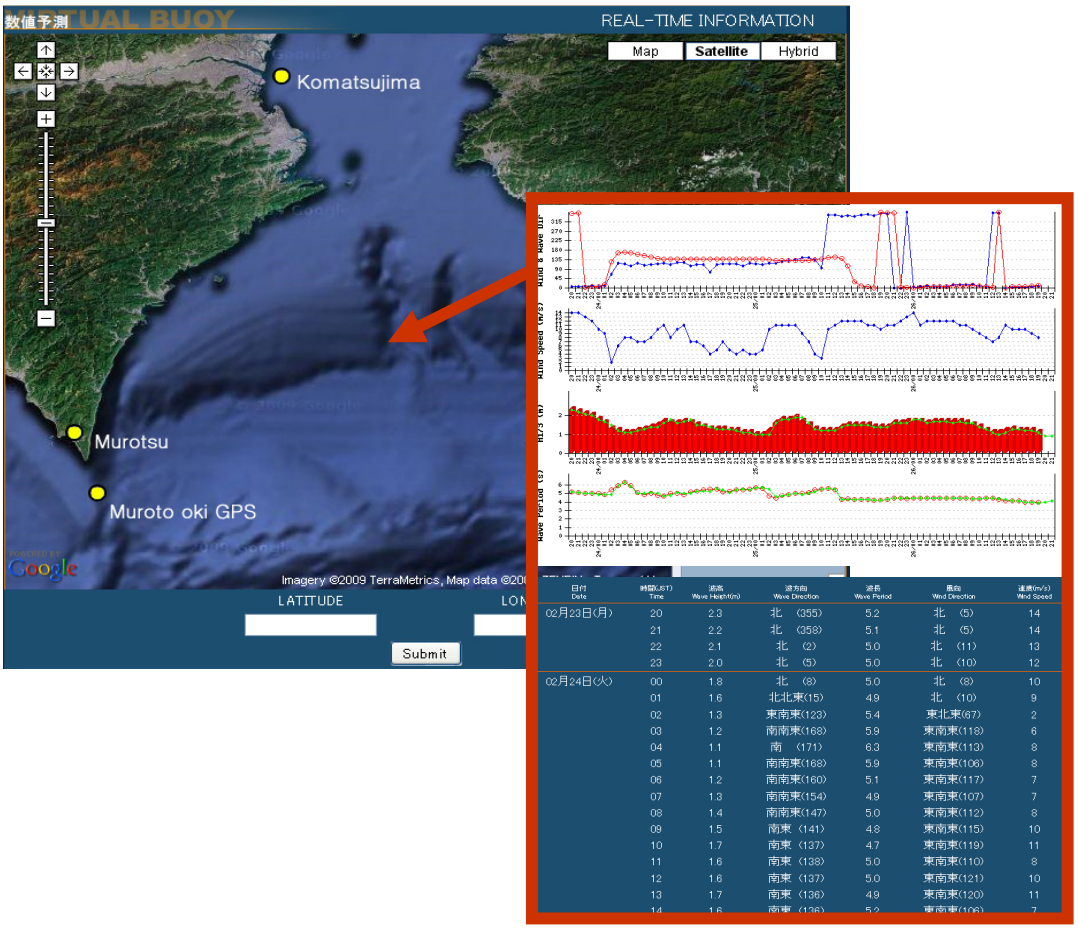

Figure 5.10 Real-time virtual buoy mashup, zoomed to Kiisuido

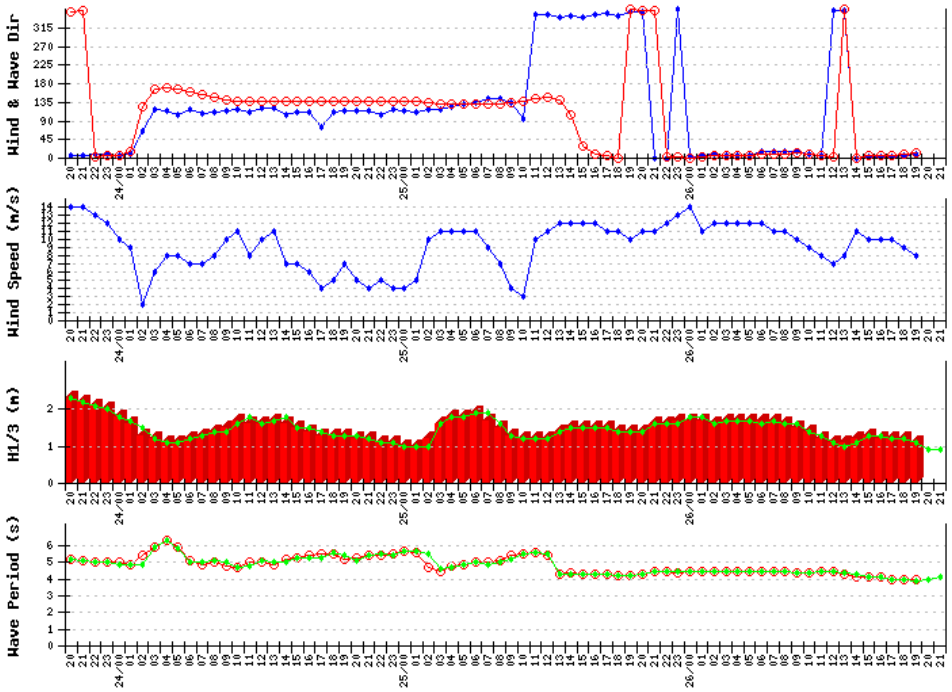

Fig. 5.11 Real-time wave prediction application display detail

5.3.2.8 Archive virtual buoy mashup

Both hindcast and forecast is archived for future use as requested. The same mashup as used in the real-time virtual buoy is used for viewing point data of archived data. The virtual buoy mashup and all underlying programs are copied to a new location and archived data of the requested time is then copied from the archive server into the data folder of the new mashup location. Point data is then available using the same functionality as the real-time virtual-buoy mashup.

This archive system allows quicker data extraction, leading to quicker analysis of prior events at areas of concern. In theory, if analysis of a prior event is immediately needed the real-time virtual buoy mashup allows evaluation of any event in the seas surrounding Japan up to three days prior. Any request prior to three days requires a new location to be created with archived data.

5.3.2.9 Conclusions

This study presented a virtual buoy system that allows access to real-time wave analysis and prediction for any point within the computational domain. Wave gauge instruments are commonly installed at high traffic areas and areas of concern, leaving other areas uncovered. Real-time analysis and short-term forecast can work in conjunction with existing observational data systems to offer a better real-time picture of the oceans state. Potentially any point in the computational domain can serve as a virtual buoy where wave gauge data is unavailable. Archives of hourly wave analysis can be extracted at any location within the computational domain, allowing immediate evaluation of hindcasts. Reducing the time and resources needed to reconstruct and analyze previous events, such as disasters or accidents caused by high wind, wave, and surge.

Chapter 6 Conclusions

6.1 Summary of this study

This study has been performed for the purpose of developing an accurate cost-effective wind-wave analysis system. Historically, proprietary wind-wave modeling systems were only accessible for commercial and disaster prevention applications due to the high operation and development cost. As the complexity of modern wind-wave models increase, moving from parameterized to explicitly solved formulation, more processing power and data storage is needed. Modern numerical weather prediction and wind-wave modeling require high performance computing (HPC) systems to accurately process weather and wave process formulation in a timely manner. Large decreases in cost of powerful commodity off the-shelf (COTS) personal computer hardware, coupled with shared open source licensing has led to the rapid development of operating system, parallel computing, and numerical modeling software. Advances in data distribution and internet communication have allowed real-time data to be shared throughout the world at little or no cost. These factors have led to the ability to develop cost effective wind-wave prediction and virtual buoy systems.

The four areas of development that form the wind-wave system were:

1) System architecture – included the development a Beowulf Class I cluster computer, to allow parallel-processing using COTS equipment along with open source licensed operating system and processing software;
2) Meteorological wind input – included study and development of atmospheric analysis and forecast data on both synoptic and meso-scale resolutions;
3) Wind wave model – included development to improve predictive accuracy of the SWAN wind-wave model.
4) System processes – included development of shell scripts and other programs necessary to automatically execute processes that convert, calculate, and distribute data.

Main results of the findings during this study are as follows:

Chapter 2 Wave prediction and analysis system

The developed wind-wave system consists of four core components: (1) System architecture, (2) Meteorological wind input, (3) Wind-wave model, and (4) System processes.

The first core component is the system architecture. The system architecture includes computing hardware that provides the system with a platform for data acquisition, processing, storage, and dissemination. The system architecture is to a Beowulf Class I cluster computer specification. System hardware utilizes commodity off the-shelf (COTS) personal computer hardware interconnected on a private local area network with an open source software infrastructure.

The second core component is the numerical weather models that describe the current and future atmospheric conditions. The key input data required by modern wind-wave models is the 10m wind grid provided by NWP models. Each NWP model wind grid affects the wind-wave model differently and accurate wind grid analysis and forecast are required to accurately calculate the ocean's state now and in the future. The two main groups of spatial scales used are synoptic and meso-scale. Synoptic-scale atmospheric models, such as the GFS, FNL, and NARR, show weather systems on a large scale, typically showing the development of large pressure system that generate hazardous high sea and surge. Meso-scale atmospheric models, such as the WRF and HAGPV, show smaller weather systems that typically generate localized wind waves.

The third component is the wind-wave model. The developed wind-wave analysis system uses the SWAN wind-wave model, Booij et al. (1999). SWAN is based on the action balance equation. Although SWAN specifically designed for coastal application, the developed wind-wave system employs it for both ocean and coastal applications. The basic calculation philosophy of SWAN is identical to WAM (WAMDI group 1988) for oceanic scales.

The default version of SWAN allows the use of two different energy transfer models for calculations. The first from WAM cycle 3 based on formulations of Komen et al. (1984) and the second from WAM cycle 4 (Komen et al. 1994) based on formulations of Janssen (1991). SWAN was modified to add the changes as specified by Lalbeharry et al. (2004) to the wind growth formulation of Janssen (1991).

Lalbeharry et al. (2004) notes two specific differences in the implementation of SWAN and WAM 4.5. First, swan omits the shift growth parameter $z\alpha = 0.011$ in the wave growth source term. Second, the wave growth limiter in the exponential wind growth source term differs between SWAN and WAM 4.5. Janssen formulation in SWAN is implemented using a limiter as described by Ris (1997) and WAM 4.5 uses an implementation specified by Hersbach and Janssen (1999).

The fourth component is systems operation and data dissemination. The developed system is designed to operate automatically without manual intervention. Data is automatically downloaded, prepared, processed, and distributed. High bandwidth internet connectivity allows timely data acquisition of atmospheric datasets from worldwide weather data centers as well as data distribution through mobile and pc internet connections.

Chapter 3 Wave forecasting and verification

Testing of wind-wave analysis system employed for wave forecasting was performed. Two studies were performed: (1) Wave forecasting system for the seas surrounding Japan, and (2) Three season study of GFS-WRF-SWAN.

The first study was performed to test wave prediction for the general seas surrounding Japan for a two month period, November and December 2004. Comparing the prediction results to observations at seven NOWPHAS wave gauge location revealed that wave height correlation was good, even at the 59th hour forecast. During this study forecasted wave height was under predicted and mean wave period was extremely under predicted.

Under prediction was attributed to: (1) differences of forecasted point and wave gauge locations, (2) synoptic scale wind data, bathymetry, wave model computational domain resolution not able to resolve small wind systems, (3) inherent computational errors in both the GFS wind and SWAN wave models.

The second study was performed to test wave prediction during three climatic seasons. Focus was aimed at better understand factors causing errors in wave prediction by the system in specific the following were performed: (1) testing the predictive accuracy of the synoptic-scale GFS and JMA GPV wind data, (2) testing the accuracy of WRF meso-scale wind forecast, (3) testing wave forecasting using GFS and WRF wind input into the SWAN wave model, and (4) testing the Komen et al. (1984), Janssen (1991) and the Lalbeharry (2004) wind growth formulation sin SWAN. It was found that:

1) GFS shows an ability to accurately predict typhoon routes given accurate initial typhoon location and conditions.
2) For results of WRF wind forecast comparisons at Aomori and Mutsu with the Automated Meteorological Data Acquisition System showed good agreement
3) Forecast by the GFS-SWAN model shows good correlation coefficient of wave forecast in the Winter and Spring. Forecast during Fall shows decreasing correlation coefficient as the forecast time series progresses into the future. The rate of decrease is dependent on the ability of GFS to reproduce pressure systems. The greatest limitation of GFS during times of typhoon strength winds is the spatial resolution of three hours, where actual typhoon movement and strength is not tracked accurately.
4) It is shown that the meso-scale wind mesh of WRF does a better job of resolving small scale weather systems than the synoptic-scale wind mesh of GFS. The GFS-WRF-SWAN model showed better performance of the GFS-SWAN model a computational domain with complex topological features that influence wind patterns.
5) Energy transfer model modifications in SWAN by Lalbeharry et al. (2004) has shown to improve wave height and period forecast correspondence with NOWPHAS buoy test points. In addition, using a large frequency range of 0.05 to 1.0 Hz decreases the forecast performance of the Lalbeharry et al. (2004) formulations. Showing its dependency on higher frequencies on the energy spectrum.

Chapter 4 Wave hindcasting and analysis

Testing of wind-wave analysis system employed for wave hindcasting was performed to show the ability of SWAN to recreate sea conditions during two previous events that generated high seas and storm surge: (1) Analysis of the damaging effects caused by Typhoon Tokage, and (2) Analysis of high waves generated by Hurricane Katrina.

The first study calculated hindcasts of a typhoon event that produced high waves and surge along the coastal areas of Shikoku and Wakayama in Japan. Typhoon Tokage caused extensive flooding to approximately 25,000 homes, damaged 500 non-residential properties, and breached barriers at 9 locations. Prediction accuracy was verified by comparing calculated results with the NOWPHAS buoy at Murotsu. Although slightly under reported, calculated hindcast showed good wave peak height prediction. The tendency of change for wave period is similar to the tendency of change for wave heights but overall wave period is generally under predicted. Overall hindcasting ability of the wind-wave system by the SWAN wave model to predict wave heights was shown to be reliable.

The second study calculated hindcast of a typhoon event that produced high waves and surge along the coastal areas of Louisiana and Mississippi in the United States of America. This study aimed to: (1) recreate conditions created by Hurricane Katrina in the Gulf of Mexico, and (2) evaluate wave prediction accuracy of three energy transfer models, with three different meteorological 10 meter wind data and two different frequency range settings.

Evaluation and comparison of each type of wind data were summarized as follows:

- NARR data contains more observational data at a higher resolution than GFS and FNL but prediction results were generally under-predicted in all test cases.
- GFS and FNL wind data produced overall similar results in test cases.
- GFS and FNL wind speed during peak wind speed was generally over-predicted. GFS data is slightly larger than FNL data, and NARR data is under-reported during this period.

Evaluation and comparison of each energy transfer model were summarized as follows:

- Komen et al.'s model (1984) provided overall good significant wave heights and mean wave periods for both frequency ranges and each wind data input. Validation statistics showed good correlation coefficient for both wave height and period. Significant wave height bias was generally low however significant wave heights during the peak of the Hurricane were under-predicted. Mean wave periods were generally under-predicted.
- Janssen's model (1991) tended to under-predict significant wave heights and periods. Using the frequency range of 0.04 to 0.5 Hz slightly increased period predictions. Significant wave height during the peak of the hurricane was greatly under-predicted. Mean wave period was under-predicted however showed better results than the Komen et al.'s model (1984).

- Modified Janssen model by Lalbeharry et al. (2004) produced very good significant wave heights and mean wave periods for frequency range of 0.04 to 0.5 Hz. Good correlation coefficient and low error bias were shown in test cases when using the smaller frequency range. During peak wind speeds at NDBC station 42040, the model well estimated the hurricane's peak significant wave height, using the smaller frequency range.

Chapter 5 Real-time wave hindcast and forecast

This study combined the research advances of both wave hindcasting and forecasting to develop a real-time wave prediction system using hourly available atmospheric GPV analysis. A hindcast and forecast of the seas surrounding Japan was calculated every hour using the hourly availability of atmospheric GPV analysis. JMA provides a, "Per Hour GPV Atmospheric Analysis," grid data which is made available as soon as 20 min after observations have been collected. This hourly GPV analysis grid is calculated using the GPV-MSM model with observational data provided by the WINDAS network of Doppler and the AMEDAS network of weather stations. Hourly wave analysis has been developed to aid in estimating wave parameters at locations where observational equipment are not available.

The first study employed the wind-wave prediction system for both hindcasting and forecasting where the hourly available GPV atmospheric analysis is used to calculate a highly accurate forecast system that predicts ocean statistical parameters in real time. Hindcast of the previous hour and a forecast of the fore-coming hour were calculated each hour as GPV atmospheric data arrived. Calculated results were compared with data from six NOWPHAS buoy points located at positions open to the sea and evaluated for accuracy. It was shown that both calculated hindcast and forecast showed a high degree of accuracy. The improvement of wave prediction shown through this test is attributed to three factors: (1) increase in temporal resolution of wind input to one hour, (2) increase in spatial resolution to two kilometers and, (3) increase in observational data assimilated into the wind analysis.

The second study develops a real-time virtual-buoy system by applying the fore-mentioned concepts of real-time wave prediction using hourly available atmospheric GPV. This system simulates a virtual buoy (wave gauge) by providing real-time wave analysis and prediction for any point within the computational domain. Wave estimations can be accessed through a web browser using a personal computer or mobile device with access to the internet. Web browser access is made possible through a "Google Map mashup" that provides a graphical interface to the data. This virtual buoy system compliments wave instruments by providing current and near future ocean condition estimations at locations where wave observations are unavailable. Archives of hourly wave analysis can be extracted at any location within the computational domain, allowing immediate evaluation of hindcasts to estimate ocean conditions. Reducing the time and resources needed to reconstruct and analyze previous events, such as disasters or accidents caused by high wind, wave, and surge.

6.2 Future development and testing

This study has shown promising hindcast and forecast ability of the developed wind-wave prediction system. To date, the real-time wave prediction using hourly atmospheric GPV data has produced the best results and additional development is being planned. This section briefly describes future development and testing.

6.2.1 Improving forecast using initial conditions of real-time hindcast

Currently the wind-wave prediction system when employed for forecasting processes a forecast four times a day. Initial condition input is required to maintain the current sea state during the start of each processing run. Spin-up is required if initial condition input is not available. The 6^{th} hour forecast snap-shot (hotfile) of the previous processing run is used as initial condition input of the current processing run. Using the real-time hindcast produced hourly as initial condition input for each processing run is expected to increase results of the wind-wave prediction system forecast.

6.2.2 Adding wave surge forecast using SuWAT

Surge Wave Tide coupled model (SuWAT) is a storm surge model developed by Kim (2007). SuWAT is a framework that couples a Hurricane surge model, wave model, and tide model to predict surge values generated by typhoon strength systems. The current wind-wave prediction system calculates forecast out to 72 hours, 4 times a day. Integrating the SuWAT model into the forecast will provide a surge forecast three days into the future, exposing areas around Japan that have a high probability of inundation by storm surge.

Appendix A References

Alves, J.H.G.M. and M.L. Banner (2003): Performance of a saturation-based dissipation-rate source term in modeling the fetch-limited evolution of wind waves, J. Phys. Oceanogr., 33, 1274-1298.

Battjes, J.A. and J.P.F.M. Janssen (1978): Energy loss and set-up due to breaking of random waves, Proc. 16th Int. Conf. Coastal Engineering, ASCE, pp. 569-587.

Booji, N., L. H. Holthuijsen and R. C. Ris (1999): A third-generation wave model for coastal regions. 1. model description and validation, J. Geophys. Res. Vol.104, 7649-7666. Press, New York, pp. 387.

Booji, N., Haagsma, I.J.G., Holthuijesen, L.H., Kieftenburg, A.T.M.M. Ris, R.C., van der Westhuysen, A.J. and Zijlema, M. (2004): SWAN Cycle III Version 40.41 Users Manual, Delft Univ of Tech, The Netherlands, p 118, http://fluidmechanics.tudelft.nl/swan/index.htm.

Bouws, E. and G.J. Komen (1983): On the balance between growth and dissipation in an extreme, depth-limited wind-sea in the southern North Sea, J. Phys. Oceanogr., Vol.13, pp. 1653−1658.

Brown, R.G. (2004): Engineering a Beowulf-style Compute Cluster, Dept of Phy, Duke Univ, http://www.phy.duke.edu/~rgb /Beowulf/beowulf_book/beowulf_book/index.html.

Bretschneider, C. L. (1952): Revised wave forecasting relationships, Proc. 2nd International Conf. on Coastal Engr., American Society of Civil Engineers, Berkeley, CA, 1-5.

Calvaleri, L. and Malanotte-Rizzoli, P. (1981): Wind wave prediction in shallow water: Theory and applications, J. Geophys. Res., Vol. 86(C11), pp 10, 961-10, 973.

Chalikov, D.V. and M. Yu. Belevich (1993): One-dimensional theory of the wave boundary layer, Bound. Layer Meteorol. 63, pp. 65-96.

Charnock, H. (1955): Wind stress on the water surface, Q. J. Royal Meteorol. Soc. 81, pp. 639-640.

Doty, B. and J.L. Kinter III (1992): The Grid Analysis and Display System (GrADS): A practical tool for earch science visualization. Eighth International Conference on Interactive Information and Procession Systems, Atlanta, Georgia, 5-10 January, 1992.

Eldeberky, Y. and J.A. Battjes (1995): Parameterization of triad interactions in wave energy models, Proc. Coastal Dynamics Conf. '95, Gdansk, Poland, pp. 140-148.

Eldeberky, Y. (1996): Nonlinear transformation of wave spectra in the nearshore zone, Ph.D. thesis, Delft Univ of Tech, Department of Civil Engineering, The Netherlands.

FNL: Final Global Data Assimilation System, National Center for Environmental Prediction, http://dss.ucar.edu/datasets/ds083.2/.

GEBCO: General Bathymetric Chart of the Oceans, Intl Hydrographic Org and the Intergovernmental Oceanographic Comm of UNESCO, http://www.ngdc.noaa.gov/mgg/gebco/.

Georga Tech. (2005): Risk increasing statement from Georga Tech. http://www.washingtonpost.com/wp-dyn/content/article/2005/09/15/AR2005091502234.html.

GFS: Global Forecasting System, National Center for Environmental Prediction, http://www.emc.ncep.noaa.gov/modelinfo.

Groop, W., Lusk, E., Ashton, D., Buntinas, D., Butler, R., Chan, A., Ross, R., Thakur, R. and Toonen, B. (2006): MPICH2 User's Guide, Mathematics and Computer Science Div, Argonne National Lab, p 35, http://www-unix.mcs.anl.gov/mpi/mpich2/downloads/mpich2-doc-user.pdf.

GPV-GSM: Grid Point Value – Global Spectral Model, Japan Meteorological Agency, http://www.jmbsc.or.jp/hp/online/f-online0a.html

GPV-RSM: Grid Point Value – Regional Spectral Model, Japan Meteorological Agency, http://www.jmbsc.or.jp/hp/online/f-online0b.html

GPV-MSM: Grid Point Value – Meso Scale Model, Japan Meteorological Agency, http://www.jmbsc.or.jp/hp/online/f-online0c.html

HAGPV: Hourly Atmospheric Analysis Grid Point Value, Japan Meteorological Agency, http://www.jmbsc.or.jp/hp/online/f-online3x.html

Hashimoto, N., Mitsui, M., Goda, Y., Nagai, T., and Takahashi, T. (1996), "Improvement of Submerged Doppler-Type Directional Wave Meter and its Application to Field Observation", Proceedings of 25th International Conference on Coastal Engineering (ICCE'96) pp.629-642.

Hasselmann K. (1962): On the non-linear energy transfer in a gravity-wave spectrum Part 1. General theory. Journal of Fluid Mechanics 12 (4): pp. 481–500.

Hasselmann, K., Barnett, T.P., Bouws, E., Carlson, H., Cartwright, H., Cartwright, D.E., Enke, K., Ewing, J.A., Gienapp, H., Hasselmann, D.E., Kruseman, P., Meerburg, A., Müller, P., Olbers, D.J., Richter, K., Sell, W. and Walden, H. (1973), Measurements of wind-wave growth and swell decay during the Joint North Sea Wave Project(JONSWAP), Dtsch. Hydrogr. Z. Suppl., 12, A8.

Hasselmann, K. (1974): On the spectral dissipation of ocean waves due to white-capping, Bound. Layer Meteor. 6, pp. 107-127.

Hasselmann, S. and K. Hasselmann (1981): A symmetrical method of computing the nonlinear transfer in a gravity-wave spectrum, Hamb. Geophys. Einzelschr. 52, pp. 1-138.

Hasselmann, S., K. Hasselmann, J.H. Allender and T.P. Barnett (1985): Computations and parameterizations of the nonlinear energy transfer in a gravity wave spectrum. Part II: Parameterizations of the nonlinear transfer for application in wave models, J. Phys. Oceanogr., 15, 11, pp. 1378-1391.

Hersbach, H. and P. A .E. M. Janssen (1999): Improvement of the short-term behavior in the wave ocean model (WAM). J. Atmos. Oceanic Techn., 16, pp. 884-892.

Holthuijsen, L.H., N. Booij (2000): Oceanic and near-shore whitecapping effects in SWAN. In Proc., Sixth Int. Workshop on Wave Hindcasting and Forecasting, pp. 362-368.

Holthuijsen, L.H. (2007): Waves in Oceanic and Coastal Waters, Cambridge University

Janssen, P.A.E.M. (1989): Wave induced stress and the drag of air flow over sea waves, J. Phys. Oceanogr., 19, pp. 745-754.

Janssen, P.A.E.M. (1991): Quasi-linear theory of wind-wave generation applied to wave forecasting, J. Phys. Oceanogr., Vol. 21, pp. 1631-1642.

Japan Marine Recreation Association (2006). Report on Marine Leisure Accidents Resulting in Injury or Death 2006, Japan Marine Recreation Association, Japan Marine Recreation Association Annual Report, Japan.

Jelesnianski, C.P. (1993): The Habitation Layer - Chapter 4, Global Guide to Tropical Cyclone Forecasting, WMO/TC-No. 560, Report No. TCP-31, World Meteorological Organization; Geneva, Switzerland.

Kalnay, Eugenia (2003): Atmospheric Modeling, Data Assimilation and Predictability. Cambridge University Press.

Kim, S.Y. (2007): Effect of large tidal variation on storm surge in the western coastal sea of Korea, PhD dissertation, Disaster Prev. Res. Inst., Kyoto Univ, pp. 121.

Knabb, R.D., Rhome J.R. and D.P. Brown (2005): Tropical Cyclone Report on Hurricane Katrina, 23-30 August 2005, US Dept of Commerce, National Oceanic and Atmospheric Admin, National Weather Service, National Hurricane Center, http://www.nhc.noaa.gov/pdf/TCR-AL122005_Katrina.pdf.

Komen, G.J., Hasselmann, K. and Hasselmann, S. (1984): On the existence of a fully developed wind-sea spectrum, J. Phys. Oceanogr., Vol. 14, pp. 1271-1285.

Komen, G. J., L. Cavaleri, M. Donelan, K. Hasselmann, S. Hasselmann and P.A.E.M. Janssen (1994), Dynamics and modeling of ocean waves, Cambridge University Press, New York. pp. 532.

Knutson, T.R. (2004): Impact of CO2-Induced Warming on Simulated Hurricane Intensity and Precipitation: Sensitivity to the Choice of Climate Model and Convective Parameterization, Journal of Climate, Vol. 17, No. 18.

Lalbeharry, R., Behrens, A., Guenther, H. and Wilson, L. (2004): An evaluation of wave model performances with linear and nonlinear dissipation source terms in Lake Erie, Proc 8th Intl Workshop on Wave Hindcasting and Forecasting, Hawaii, USA.

LSU Hurricane Center (2005): Hurricane Katrina Hindcast, Luisiana State Univ, http://hurricane.lsu.edu/floodprediction/katrina32/images/ katrina32.JPG.

McGranahan, G., D. Balk and B. Anderson (2007). The rising tide: assessing the risks of climate change and human settlements in low elevation coastal zones. Environment & Urbanization 19(1): 17-37 (2007). International Institute for Environment and Development (IIED), http://eau.sagepub.com/cgi/content/abstract/19/1/17.

Madsen, P.A. and O.R. Sørensen (1993): Bound waves and triad interactions in shallow water, Ocean Engineering, 20, 4, pp. 359-388.

Marine Accident Inquiry Agency (2003). Report on Marinie Accidents 2003, Marine Accident Inquiry Agency, Marine Accident Inquiry Agency Annual Report, Japan, http://www.mlit.go.jp/maia/12english/report2003/Contents.htm.

Mase, H., S. Katsui, T. Yasuda, and T. H. Tom (2005). Verification of GFS-WRF-SWAN Wave Prediction System By Three Seasons' Comparison. Annual Journal of Coastal Engineering, 52(1): 181-185.

Miles, J.W. (1957): On the generation of surface waves by shear flows, J. Fluid Mech., Vol. 3, pp. 185-204.

Mitsuyasu, H. (1968): On the growth of the spectrum of wind-generated waves, Rep. Res. Inst. Appl. Mech. Kyushu University 16, pp. 251-264.

Moskowitz L. (1964): Estimates of the power spectrums for fully developed seas for wind speeds of 20 to 40 knots. Journal of Geophysical Research 69 (24): pp. 5161–5179.

NARR: North American Regional Reanalysis, National Center for Environmental Prediction, http://www.emc.ncep.noaa.gov/mmb/rreanl/.

National Weather Service (2005): Service Assessment, Hurricane Katrina August 21-31, 2005, U.S. Dept. of Commerce, National Oceanic and Atmospheric Administration, http://www.weather.gov/os/assessments/pdfs/Katrina.pdf.

NDBC: National Data Buoy Center, National Oceanic and Atmospheric Administration, http://www.ncbc.noaa.gov/

NOMADS: The NOAA Operational Model Archive Distributed System, A network of environmental data sets from NOAA and other organizations where data is served through a common framework and protocol, http://www.ncdc.noaa.gov/oa/climate/nomads/nomads.html.

Orlanski, I., (1975): A rational subdivision of scales for atmospheric processes. Bull. Amer. Meteor. Soc., 56, pp. 527-530.

Phillips, O.M. (1957): On the generation of waves by turbulent wind, J. Fluid Mech., Vol. 2, pp. 417-445.

Phillips, O.M (1958): The equilibrium range in the spectrum of wind-generated ocean waves, J. Fluid Mech. 107, pp. 465-485.

Phillips O.M. (1960): On the dynamics of unsteady gravity waves of finite amplitude. Part I. The elementary interactions. Journal of Fluid Mechanics 9 (2): pp. 193–217.

Pierson, W.J., G. Neuman, and R.W. James (1955): Observing and forecasting ocean waves by means of wave spectra statistics, H. O. Pub. No 603, U.S. Navy Hydrographical Office, Washington, D.C.

Ris, R.C. (1997): Spectral Modeling of Wind Waves in Coastal Areas, Dept of Civil Eng, Delft Univ of Tech, Rpt No 97-4, pp. 160.

Severdrup, H.U., W.H. Munk (1947): Wind, sea and swell: theory of relations for forecasting. U.S. Navy Hydrographic Office Pub. No. 601. pp. 44 .

Sugahara, K., Sato, K., Nagai, T. and Kawaguchi, K (1999). Summary of the NOWPHAS wave, tide, and wind observation facilities, Tech. Note of Port and Harbour Research Institute, Ministry of Transport, Japan, No.941.

SWAMP (1985): Sea wave modeling project (SWAMP). An intercomparison study of wind wave prediction models, Part 1: Principal results and conclusions, Ocean wave modeling, Plenum Press, New York.

SWAN: Simulating Waves Nearshore, A numerical wave model for obtaining realistic estimates of wave parameters in coastal areas, lakes and estuaries from given wind-, bottom-, and current conditions developed by Delft University of Technology,

http://fluidmechanics.tudelft.nl/swan/default.htm.

Takayama, T., Hashimoto, N., Nagai, T., Takahashi, T., Sasaki, H., and Ito, Y. (1994), "Development of Submerged Doppler-type Directional Wave Meter", Proceedings of the 24th International Conference on Coastal Engineering (ICCE'94), Vol.1. pp.624-634.

Takayama, T. (2006): Disasters in Japan Due to Storm Surges and Waves, Japan Seminar on Hurricane Katrina Disaster Reports, Tokyo, Japan.

Tolman, H.L. (1992): Effects of numeric's on the physics in a third-generation wind-wave model, J. Phys. Oceanogr., Vol. 22(10), pp. 1095-1111.

Tolman, H.L. and D, Chalikov (1996):, Source terms in a third-generation wind wave model, J. Phys. Oceanogr. 26(11), pp. 2497-2518.

Tom, T. H., H. Mase, S. Katsui, T. Yasuda, and K. Ogawa (2006). Analysis of High Seas Generated by Hurricane Katrina. Annual Journal of Coastal Engineering, 53(1): 421-425.

Tom, T. H., H. Mase, and T. Yasuda (2008). Real-time Wave Prediction Using Hourly Analyzed Atmospheric GPV. Annual Journal of Coastal Engineering, 55(1): 186-190.

US Army Corps of Engineers (2006): Performance Evaluation of the New Orleans and Southeast Louisiana Hurricane Protection System, Volume I Executive Summary and Overview, Draft Final Report, Interagency Performance Evaluation Task Force, pp. 50, https://IPET.wes.army.mil.

WAMDI group (1988): The WAM model – a third generation ocean wave prediction model, J. Phys. Oceanogr., Vol. 18, pp. 1775-1810.

Whitham, G.B. (1974): Linear and nonlinear waves, Wiley, New York, pp. 636

WRF: Weather Research and Forecasting, A meso-scale numerical weather prediction model originally developed at NCAR (the National Center for Atmospheric Research), http://wrf-model.org

Wu, J. (1982): Wind-stress coefficients over sea surface from breeze to hurricane, J.Geophys., Res., 87, C12, pp. 9704-9706